Frictional behaviour of pigs in motion

Report number: 2732

A. den Heijer

Technische Universiteit Delft

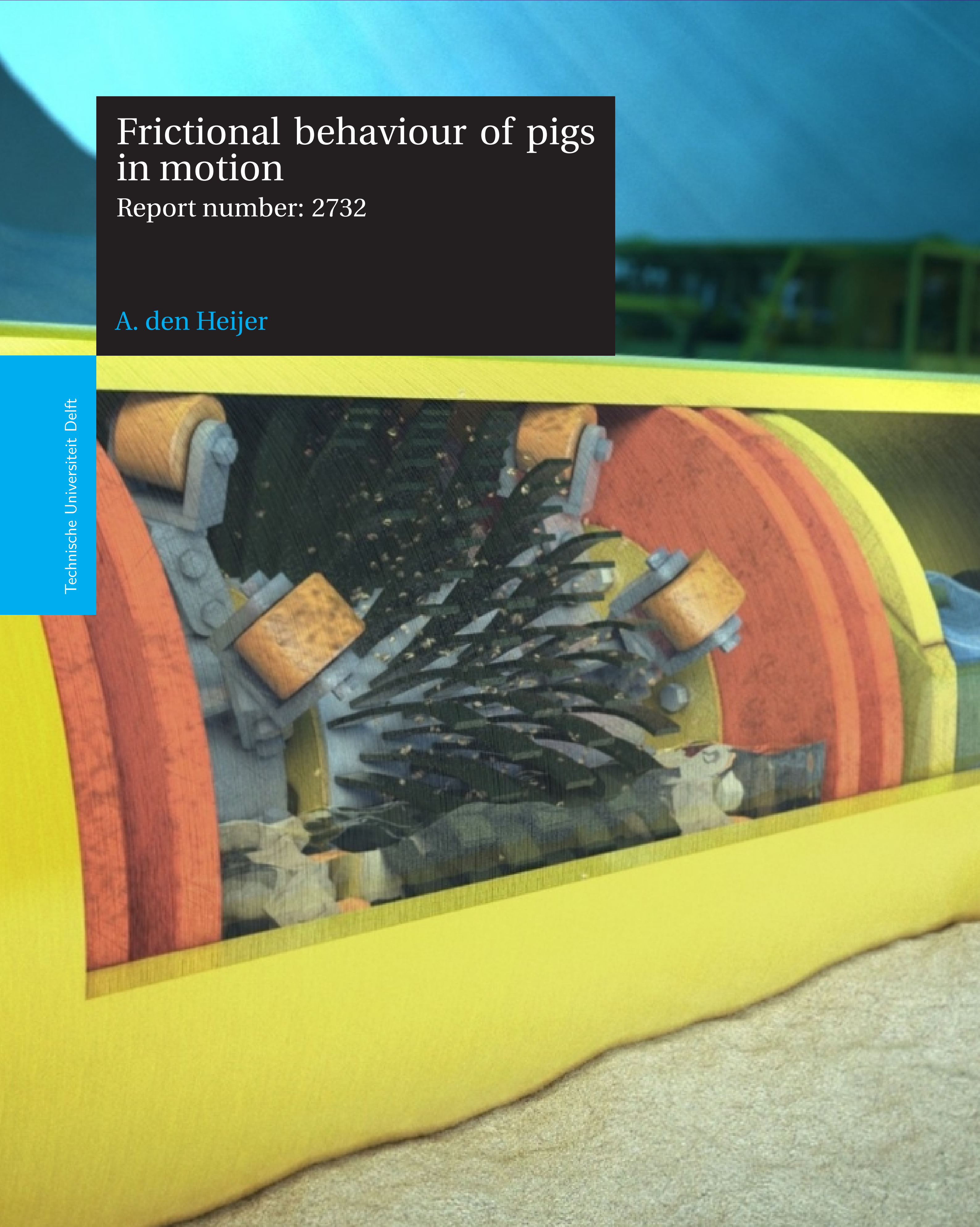

Delft University of Technology

Challenge the future

Frictional behaviour of pigs in motion

Report number: 2732

by

A. den Heijer

in partial fulfillment of the requirements for the degree of

Master of Science
in Mechanical Engineering

at the Delft University of Technology,
to be defended publicly on Monday April 25, 2016 at 10:00 AM.

Student number:	1382667	
Supervisors:	Prof. dr. ir. R. A. W. M. Henkes,	TU Delft
	Dr. ir. W.-P. Breugem,	TU Delft
	Dr. ir. R. A. J. van Ostayen,	TU Delft
	Ir. M. H. W. Hendrix	TU Delft
External Reviewer:	Dr. ir. B. W. van Oudheusden,	TU Delft

An electronic version of this thesis is available at http://repository.tudelft.nl/.

TU Delft — Delft University of Technology

Preface

I would like to express my appreciation to everyone who provided me the possibility to complete this thesis. Without their help it would not have been possible. Notably, I would like to thank Prof. dr. ir. Ruud Henkes. He introduced me to the subject and gave me the opportunity to perform the research at Shell Amsterdam. I have been supported greatly and Shell never limited me in achieving my own full potential. A great, but confrontational time, in which I learned my own limits and have achieved a lot.

I especially would like to thank dr. ir. Ron van Ostayen and dr. ir. Wim-Paul Breugem. Their input has been valued very much. I have always left our meetings with additional energy and curiosity.

No words can express the appreciation to ir. Maurice Hendrix, who not only was a great supervisor, but also became a personal friend.

At Shell I would like to thank ir. Peter Veenstra. Our mentor meetings helped me in managing all the stakes in the project, and gave me confidence in the path I had set out. Also the support by ir. Gijs Groote, who helped in determining the practical relevance of each step, and by dr. ir. Maurice Fransen, who still looks into the further implementation of the work done in this thesis, should not stay unnoticed.

The experimental part of this thesis could not have been performed without the help of ir. Arend van Wolfswinkel, who helped in the design and the operation of the experiments. Thanks are also due to Harry Gusselkoo, who performed the construction work and who even during Christmas was willing to make some adjustments.

Furthermore, I would like to thank all the people supporting me personally during the final part of my studies. First of all my girlfriend, Els Brouwer, who not only was always there for me, but also helped me with improving the writing of this thesis. My parents for their support. My friends from "intern island" with whom I could change ideas so easily. And finally my fellow students at the university who made me laugh so much during the final hours of writing this report.

A. den Heijer
Delft, April 2016

Abstract

Pigs (pipeline inspection gauges) are free moving piston-like devices, that are used for inspecting or cleaning pipelines in for example the oil and gas industry. Here they are for used for onshore and offshore pipelines, where they are propelled by the production fluids. A better control of the velocity of the pig in the pipeline can be achieved by using so-called bypass pigs, which have an opening (bypass) that allows that some fluid passes by which reduces the pig velocity. A new development is a by-pass pig with speed control, in which the bypass area is adjusted when the pig moves through the pipeline to obtain a constant preset pig velocity. The goal of this research was to accurately describe the forces on a pig, with special emphasis on the friction between the pig and the pipe wall. Such a wall friction model can be used in pipeline simulation tools, that are used to prepare a pigging operation.

The friction force is divided into two parts: (1) the normal force that the pig imposes on the pipeline wall (F_{wall}) and (2) the coefficient of friction (μ) which converts F_{wall} to a friction force.

F_{wall} is calculated by a non-linear finite element model for a 12" sealing disk for a range of oversizes. A uniaxial tensile lab test was performed to fit the material coefficients used in the non-linear Mooney-Rivlin material model. It was shown that the results could be matched by a linear elastic analytical model with a correction factor Cor = 1.45.

An experiment was designed to measure both μ and F_{wall} for a range of pig disk oversizes. These values were measured for sealing disks with different thicknesses and made of different materials. The models were able to accurately describe the experiment results.

Due to lubrication the coefficient of friction can drop by orders of magnitude. Lubrication can be described by the Reynolds equation for the fluid pressure of thin fluid films. The material of a pig that makes contact with the pipeline wall is deformed by this fluid pressure which can be described by soft elastohydrodynamic lubrication theory.

To couple the linear elastic material of the sealing disk to the non-linear Reynolds equation, two numerical approaches were followed. Firstly, the linear elastic contact was described by a row of closely spaced linear springs. Secondly a lubrication model was made in which the linear elastic contact was described by the boundary element method. This method allows the description of a whole domain by only the boundary (for example a surface by a 1D boundary line).

It was shown that these models give a good qualitative description of the lubrication behaviour. The model validation is left for future work.

In addition, pressure drop measurements were performed in a flow loop for a model of the bypass pig. These measurements were compared with correlations from the literature.

Contents

List of Figures

List of Tables

Nomenclature

English notations:

Symbol	Units	Description
A	m^2	Area
A_0	m^2	Pipe area
A_1	m^2	Bypass area
a	m	Foot length
a^-	m	Negative foot length
a^+	m	Positive foot length
C	–	Correction factor
C_d	[–]	Drag coefficient
c	m	Chamfer length
D	m	Pipe diameter
d	m	Bypass diameter
d_{plate}	m	Plate diameter
E	Pa	E-modulus
E^*	Pa	Plain strain E-modulus
E_{fit}	Pa	Fitted E-modulus
F	N	Force
F_f	N	Friction force
F_n	N	Normal force
F_a	N/m	Asperity force
F_{axial}	N	Force in axial direction, measurement result
F_{circ}	N	F_{wall} per radian, measurement result
F_{friction}	N/m	Friction force per meter
F_{pressure}	N/m	Driving pressure force per meter
F_{wall}	N/m	Wall force per meter
h	m	Fluid film height
f	N/m	Traction
h_o	m	Original film height
K	–	Winkler constant
K_s	–	Friction number
L	m	Beam length
l	m	Sealing disc length (r-r_p)
l'	m	Sealing disc length (r_s-r_p)
$M_{\delta P}$	$N.m$	Pressure moment
M_θ	$N.m$	Hoop stress induced moment
M_c	$N.m$	Compressive stress induced moment
M_f	$N.m$	Friction induced moment
M_t	$N.m$	Tensile stress induced moment
M_w	$N.m$	Wall force induced moment
m	–	Inclination chamfer
N_a	$\#/m^2$	Average number of asperities per meter
P	N	Load
P_a	Pa	Asperity pressure
P_f	Pa	Fluid pressure
P_t	Pa	Contact pressure
P_{to}	Pa	Original contact pressure
R	m	Radius in analytical kinematic model
R_a	m	Average asperity radius

Re_{bp}	–	Bypass Reynolds number
$RELAX$	–	Relaxation factor
r	m	Pipe radius
r_i	m	Inner radius
r_p	m	Spacer disk radius
r_s	m	Sealing disk radius
S_a	–	Shore hardness
T		Fundamental solution
t	m	Thickness
t_p	m	Spacer disk thickness
t_w	m	Chamfer length
U		Fundamental solution
u	$m/s/m$	Velocity / Displacement
u_{pig}	m/s	Pig speed
u_{mix}	m/s	Fluid mixture velocity
w_{plate}	m	Distance between bypass pig and bypass disk

Greek notations

Symbol	**Units**	**Description**
α	rad	Dummy variable in integration, Chamfer angle in BEM lubrication model
β	rad	Angle in radian in the analytical kinematic model
Γ	–	Error function
γ_{rz}	–	$2\epsilon_{\mathrm{rz}}$
δ	–	Oversize
δ_{ij}		Kronecker delta
δ_o	m	Original indentation
ϵ	–	Strain
ζ	–	Thickness ratio
η	$Pa.s$	Dynamic viscosity
θ	rad	Circumferential direction sealing disk
κ	m^{-1}	Curvature
λ	Pa	Lamé constant
μ	–	Coefficient of friction, Lamé constant
μ_{dry}	–	Dry coefficient of friction
μ_{static}	–	Static coefficient of friction
μ_{dynamic}	–	Dynamic coefficient of friction
ν	–	Poisson's ratio
ρ	kg/m^3	Fluid density
σ	Pa	Stress
ω	m	Compliance

1

Introduction to pigging

Pigging is the act of running a pig through a pipeline. A pig (pipeline inspection gauge) can be employed in single and multiphase pipeline systems. The pig interacts with the flow behaviour of the surrounding fluids and or solids. These solids and fluids need to be managed to secure the integrity of the system. This is done by control of the fluid flow and by building facilities such as slugcatchers which act like a buffer. To model the pipeline system response to control and to engineer the facilities it is important to accurately model the friction of a pig. In this chapter a global introduction to pigging will be given. First some background on pigging is given in Section 1.1 to place the research in the proper perspective. In Section 1.2 the different types of pigs are described. In Section 1.3 bypass pigs and its application is discussed. In Section 1.4 the research goal of this thesis is given. Finally, the conclusions of this chapter are summarized in Section 1.5.

1.1. Background to pigging

Pipelines often prove to be the most economical, the safest and the most reliable way of transporting oil and gas [15]. A standard industrial procedure to improve the efficiency and the safety of oil and gas pipelines is the use of a pig, which is commonly referred to as pigging. A pig (pipeline inspection gauge) is a freely moving piston in a pipeline. Typically a pig is propelled by the gas and/or liquid flow in the pipeline. Exceptions are pull-through or self-propelled pigs. Pull-through pigs are pulled through a pipeline by a rope or a chain. Self-propelled pigs move through pipelines by a driving mechanism. Examples of self-propelled pigs are the ones used by James Bond to dismantle a nuclear bomb transported through a pipeline [16], or in the Hyperloop proposed by Musk [17] as a new transport method. Pigs have multiple purposes in the process industry such as: removing liquid in the pipeline, removing deposits from the pipeline wall and inspection of the pipeline wall. Tiratsoo [14] further specifies the purposes of pigs in six different phases of the lifetime of a pipeline. The six phases of the lifetime of a pipeline are in order of time: construction, operation, inspection, general maintenance and repair, renovation and rehabilitation, and decommissioning. In Table 1.1 the purposes for each phase are stated.

Table 1.1: A summary of reasons to pig during different phases of the lifetime of a pipeline [14].

Construction	**General maintenance**
Removing construction debris	Corrosion inhibition
Acceptance testing	Pre-inspection cleaning
Operation	Isolation
Pipeline wall cleaning	Recommissioning
Condensate removal	**During renovation/rehabilitation**
Product separation (batching)	Gel pigging
Applying corrosion inhibitors	Chemical cleaning
Inspection	Scale removal
Check for physical damage (dents)	**Decommissioning**
Detect corrosion, lamination's or cracking	Product removal
Leak detection	Pipe wall cleaning
Sampling	Inspection/testing

1.2. TYPES OF PIGS

(a) Foam pigs

(b) Cup pig

(c) Bi-directional pig

(d) Intelligent pig

Figure 1.1: Different pig types used for multiple purposes [1].

In the previous section the purpose of pigging was given. Different types of pigs have been designed to optimally serve each purpose. In this section pigs are differentiated in four categories: inflatable and foam pigs, cone pigs, bidi pigs, and intelligent pigs [14]. In Figure 1.1 an example of each different type of pig is shown.

An inflatable pig is often a sphere with a polyurethane skin, filled with water or glycol. A foam pig is made of a very flexible piece of foam, typically spherical, cylindrical or more cone like shaped. Often one side of the foam pig is sealed, so that the pig is propelled by the fluid behind it. Inflatable pigs and foam pigs are often used in a first pigging attempt, because they can undergo large deformations, such as ovalities, tight bends, valves and T-bends. Their ability to deform makes the risk for the pig to get stuck very low.

Cup pigs are steel tubes with large polyurethane cups attached. By the driving pressure the cups are pressed onto the pipe wall securing a tight seal. The tight seal allows little leakage across the pig which makes them useful for batching liquid between two cup pigs. However, when cup pigs get stuck they are very hard to remove.

Bi-directional pigs are similar to cup pigs in the sense that they consist of a tube with polyurethane disks attached. However, the polyurethane disks are straight, and the pig thus has no preference for the direction of movement.

Intelligent pigs often consist of a train of bi-directional pigs and cup pigs with electronics, wheels, scrapers and sensors in between. The train with equipment serves to inspect or clean pipelines. For inspection purposes the intelligent pig often needs to control its speed which is done by adjusting a bypass of flow through the pig. The rather large length of an intelligent pig and the multiple polyurethane disks attached to it increase the pressure drop required to drive it.

The main focus of this thesis will be on bi-directional pigs. The bi-drectional pig is most commonly used for heavy duty pigging jobs such as dewatering, dewaxing and cleaning. The flat oversized sealing disk of the bi-directional pig secures a good seal which makes it superior in cleaning and maintenance tasks [6]. Note that in the case of intelligent pigs also often the same flat sealing disks are used. The flat disks makes a relatively simple starting point of this research. After this is done more complex shapes can be investigated. A special feature which is not exclusive, but often seen on bidirectional pigs is the use of a bypass. In the following section bypass pigs and bypass pigging is discussed.

1.3. BYPASS PIGGING

A bypass pig the production fluid to flow through the pig during the pigging operation. To operate pigs sometimes the flow velocity of the fluid through the pipeline has to be reduced (for example because the pressure or velocity is too high). A reduction in flow velocity means a reduction in production and thus production deferment. By allowing fluid to flow through the pig, the pressure drop over the pig and therefore the speed of the pig in the pipeline can be reduced without reducing the production. Any pipeline that will face production deferment as a result of pigging is a potential candidate for bypass pigging. Since the costs of bypass pigging over normal pigging are very small, and the reward by the reduction of product deferment is very high, the employment of bypass can be very lucrative. However, when the bypass becomes too large the pig will get stuck and the costs will also be very high.The trick to bypass pigging therefore is to balance the bypass area with the friction of the pig. That a bypass can be used to reduce the speed of a pig is of course evident. However bypassing pigging also has some large advantages in the case of dewaxing and dewatering.

Figure 1.2: A wax plug received after a cleaning operation with a pig [2].

Dewaxing is necessary because the cooling of hot, high pressure oil can cause deposition of wax. The wax deposits on the pipeline wall will decrease the radius of the pipeline. A smaller pipeline radius will cause a higher pressure drop over the pipeline. This reduces the amount of fluid that the pipeline can transport. During dewaxing, a plug of the deposited wax is formed in front of the pig. An example of such a wax plug is shown in Figure 1.2. The pigging frequency needs to be high enough so that the pressure drop caused by the wax plug does not stall the pig. Models to predict the build up of wax and the build up of pressure drop over a wax plug do exist [18] [19] [20]. When the wax plug becomes too large, the pig gets stuck and the pipeline is clogged. Unclogging a pipeline or laying a new piece of pipeline, combined with the deferment caused during that time, makes a stuck pig a very expensive undertaking [21]. Because the costs of pigging are relatively low and the costs of a stuck pig are very high, oil pipelines are typically pigged sufficiently often to minimize the wax deposit and related wax plug length [22].

A bypass pig causes a highly turbulent jet in front of the pig which helps in breaking the wax plug into particles. This is shown in Figure 1.3. The formation of a wax plug in front of a pig is a risk since it can cause

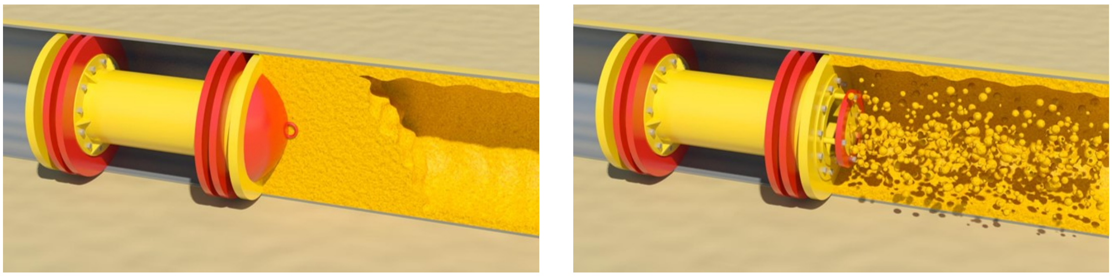

(a) Fluid forces working on the standard pig push the wax plug out.

(b) The by-pass pig smooths out the liquid surge and transports the solid particles as a slurry.

Figure 1.3: Wax removal without and with by-pass pigging [3].

the pig to get stuck. A bypass will however reduce the driving pressure on the pig. Therefore the risk of the pig getting stuck also increases. The trick to bypass pigging is to find a balance between the wax plug reduction (by creating a bypass) and the driving pressure (dependent on the bypass).

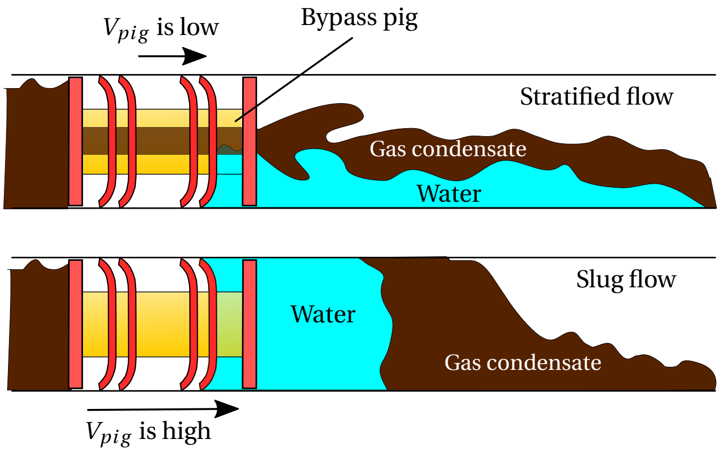

Figure 1.4: Different flow regimes in front of the pig. Schematic adapted from Groote [4].

A second application of bypass pigging is in the dewatering of pipelines. Pigs can be used for liquid removal from for example gas condensate pipelines. Liquids will accumulate in the lower points of the pipeline. This liquid can be removed by running a pig through the pipeline. The liquid can have various flow patterns, depending on the specific local conditions. For example as a stratified liquid layer on the bottom of the pipe or as a slug in front of the pig. This is illustrated in Figure 1.4. When a slug forms in front of a pig, the slug needs to be stored by a slug catcher. A slug catcher serves to separate gas and liquid. Slug catchers are large devices with high capital expenditure. To illustrate the size, Figure 1.5 shows a slug catcher.

By increasing the bypass, the speed of the pig will decrease. When the pig moves with the velocity of the fluid liquid layer in front of the pig no slug will form and the flow will remain stratified. To model the fluid flow in front of a pig in large pipeline systems 1D models are typically used. One of the purposes of these 1D flow models is to find the required size of a slug catcher. This size is determined by the surge volume, which is equal to the amount of liquid that has to be stored temporarily. The maximum surge volume is determined by the size of the liquid slug arriving minus the capacity of the plant to process the liquid over the slug arrival time interval.

To determine the speed of a pig models need to balance the driving pressure on a pig by a friction force. In Figure 1.6(a) the surge volume as a function of the bypass area is shown for one situation described by Groote [4]. The goal in this figure is to reduce the slug catcher size from 700 m^3 to 150 m^3. Spronsen [23] reports that with bypass pigging the slugcatcher size can be reduced by up to a factor 4 with related cost savings of tens to hundreds of milions USD. In Figure 1.6(a) the friction force is varied by plus and minus 50%. In the following chapter an investigation into the accuracy of friction models is done. Note however, that a wrong prediction of the friction of a pig can under or over predict the necessary dimensions of a slug catcher by hundreds of cubic meters. In Figure 1.6(b) measurements from an operation by Shell are shown. It can be seen that bypass

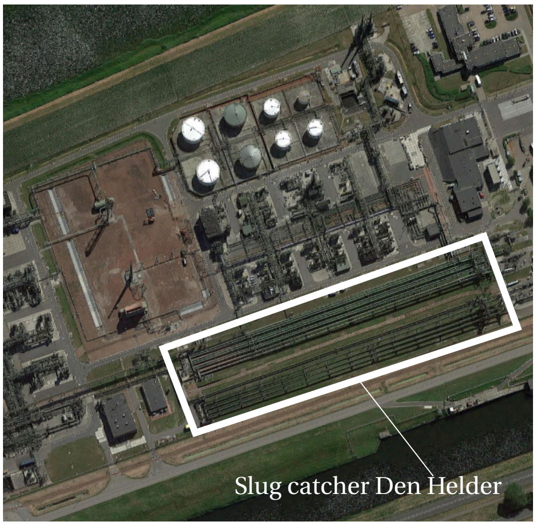

(a) The slug catcher in Den Helder as can be seen on Google maps.

(b) A slug catcher from nearby with a person in front of it [3].

Figure 1.5: Two pictures of slug catchers to illustrate the size of slug catchers.

pigging works properly and that a peak of liquid flow can be reduced significantly by using bypass pigging.

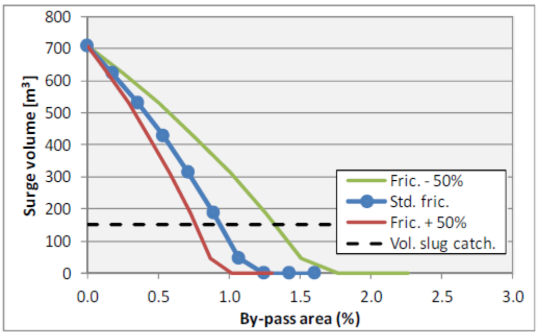

(a) Results from a mechanistic model used to predict the surge volume [4].

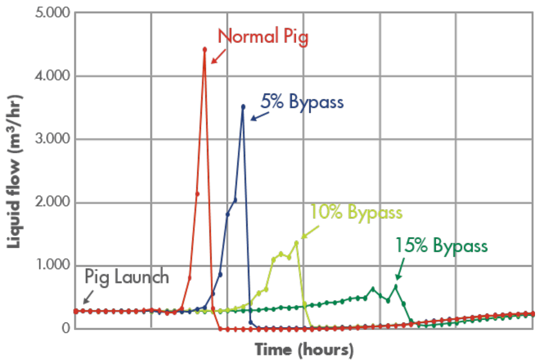

(b) Results measured at the outlet of a two-phase Pipeline: 120 km, 36 inch [3].

Figure 1.6: (a) The results from a simplified model with varying friction values. A 50% change in friction force can have tremendous influence on the fluid mechanics [4]. (b) Different results from an actual pipeline. The surge volume and deferment are reduced considerably by the employment of bypass pigging [3].

1.4. RESEARCH GOAL

By accurate modelling of pigs and the interaction of pigs with the surrounding fluids the production, dewaxing frequency and slugcatcher size is determined. Bidirectional pigs are the most common type of pigs for these jobs, and therefore the research in this thesis will focus on those first. Bypass pigging has the potential to improve current pigging operations with potential cost savings following. In the recent literature the values for the friction force are varied by 50% [4]. The used models to predict this friction force are discussed in the following chapter. However, it can already be stated that the currently used accuracy of 50% is very optimistic. An accurate description of the friction is essential to promote the employment of bypass pigging. The goal of this thesis is to model the frictional behaviour of bidirectional bypass pigs as accurate as possible with the input parameters typically available.

1.5. SUMMARY

The purpose of pigging in the oil and gas industry was discussed in this chapter. Bypass pigging adds value by increasing the production over normal pigging, reducing the risk of clogging by a wax plug and decreasing the necessary dimensions of a slug catcher. When employing bypass pigging a balance has to be found between the bypass area and the friction of the pig. In this chapter the goal of this thesis project was defined. In the following chapter the physical phenomena, the available models and the experiment are described.

2

MODELLING OF PIGGING

In this chapter a framework is given to investigate and compare different pig friction models. Firstly, each part of the framework is discussed to show the required input and output parameters and the underlying physical phenomena. This is done in Section 2.1. Secondly, pigging models from the literature are discussed and compared in section 2.2. Thirdly, the available experimental validations found in the literature are discussed in Section 2.3. With knowledge about the relevant phenomena, available models and available experimental validation of these models an outline can be made for this thesis. This is done in Section 2.4. Finally, the conclusions of this chapter are summarized in Section 2.5.

2.1. FRAMEWORK

In Figure 2.1 an overview of the forces on a pig is given. The three forces are described by three different branches of mechanical engineering. The force on the wall is described by solid mechanics theory, the phenomena between two moving surfaces such as friction and wear are described by tribology and the pressure force on the pig is described by fluid mechanics.

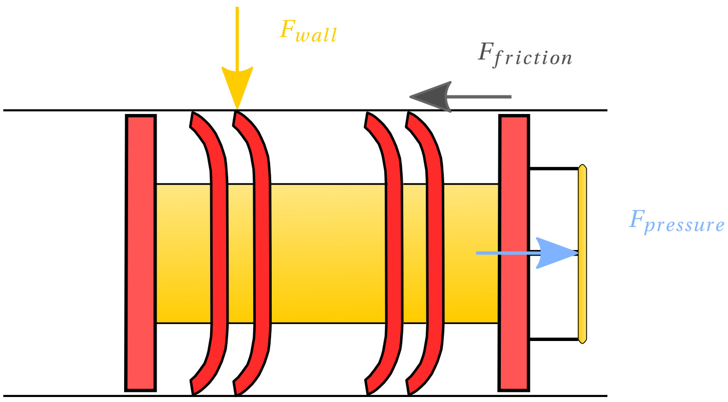

Figure 2.1: Three forces are involved in the friction of a pig during motion. The force normal on the pipeline wall F_{wall}, the friction force F_{friction} tangential to the pipeline wall and the driving pressure force F_{pressure}.

A model of the relevant phenomena that describes each force is given in Figure 2.2. With arrows the causality of change of the input and the output parameters are given. The design dimensions and material properties of the pig are assumed to be given and to be constant during pigging. The operating conditions are given by the pipeline system and can influence each relevant phenomenon. The pig velocity is an output parameter which has a large influence on each phenomenon. The wall force is determined by geometric considerations together with the differential pressure over the pig. The coefficient of friction is a function of the load and can be reduced by lubrication, which will occur when the speed of the pig is high enough. This implies that an increase of the pig velocity can lead to a decrease of the differential pressure over the pig.

In the following seven subsections each part of Figure 2.2 is discussed.

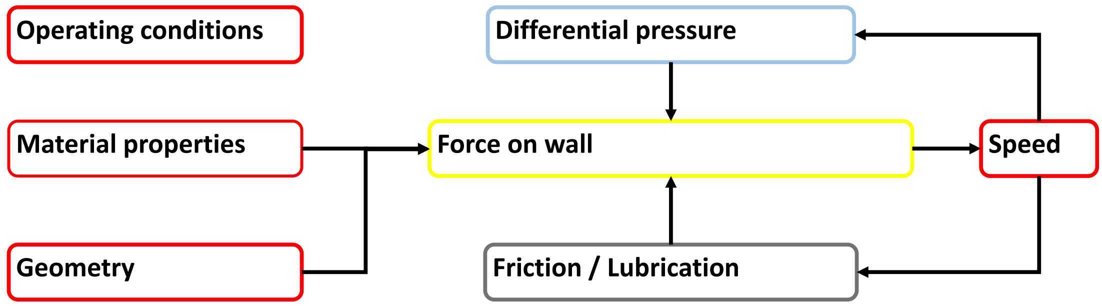

Figure 2.2: A schematic overview of the physical phenomena which occur during pigging.

2.1.1. OPERATING CONDITIONS

In this section the physics of a pig in an offshore gas condensate trunk line will be discussed. Topics which will be addressed are:

- Fluid properties
- Pipeline properties
- Material properties
- Operating conditions
- Chemical environment

Condensate is an oil that is co-produced with natural gas from reservoirs. Each condensate has a unique composition, but some typical 'standardized' compositions exist. It should be noted that often in addition to the condensate also some free water is co-produced with the gas in the trunkline in the field. To simplify lab experiments often water instead of condensate is used. In the calculations done in this report only water will be assumed as the propelling fluid.

Trunklines vary in size and material. Typical sizes vary from 8" to 60". Pipelines are made of multiple types of steel which can be assumed undeformable compared to the polyurethane rubber of a pig. The wall roughness of pipelines varies over time and the wall can be covered with waxy deposits.

Numerous models have been made to model the temperature and the pressure along a pipeline. The initial pressures and temperatures of fluid leaving a well are high. However, because of heat losses to the surrounding the fluids quickly cool to the ambient conditions. For the sea often about 5 °C is used and for land 25 °C [18]. For practical reasons, and to enable the comparison of the model simulation with experiments done at room temperature, an ambient temperature of 20 °C will be assumed in this report.

2.1.2. MATERIAL PROPERTIES

Pigging disks are made of polyurethane. Polyurethane can have a wide range of properties, such as those used for bed mattresses and golf balls. Polyurethane can be mixed with multiple additives to obtain specific material properties. Often the mixture of adhesives is proprietary to the manufacturer. However, some standardized tests to check the material properties of polyurethane exist. The three most important tests for this application are hardness tests, tensile strength tests and wear tests.

The shore hardness is an indicator of the E-modulus of the disk. To measure the shore hardness ASTM D2240 or DIN 53505 is used. Typically pig disks are made of Shore A65 to A85 material. The tensile strength is an indication of the force that the rubber can resist before tearing. The tensile strength also gives values for the E-modulus of the material along a range of elongations. The tensile strength is measured according to ASTM D402. The results of these two experiments will be given in Chapter B.

The wear of a pig sealing disk can be measured by an abrasion loss test. This is typically done according to ASTM D5963. In this thesis this tests is not done.

2.1.3. GEOMETRY

A bidi pig is built up as shown in Figure 2.3. The sealing disks are fitted into the pipeline to form a seal. The spacer disks are used to clamp the sealing disks and larger clamping disks can increase the resistance against deformation of the sealing disks. Guiding disks are the first and last rubber disks and they guide the pig through bends.

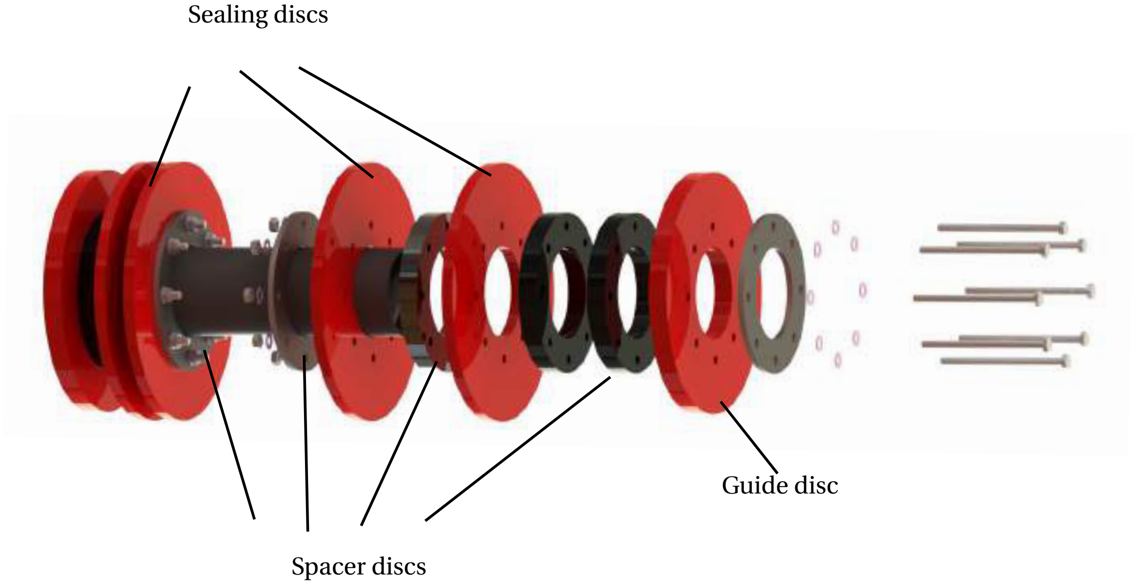

Figure 2.3: The typical build up of a bidi bypass pig [1].

The design dimensions of one sealing disk are shown in Figure 2.4. Other dimensions such as pig length, guiding disk dimensions, and other scraping or sensing structures will not be taken into account. The different pig dimensions are given in Table 2.1.

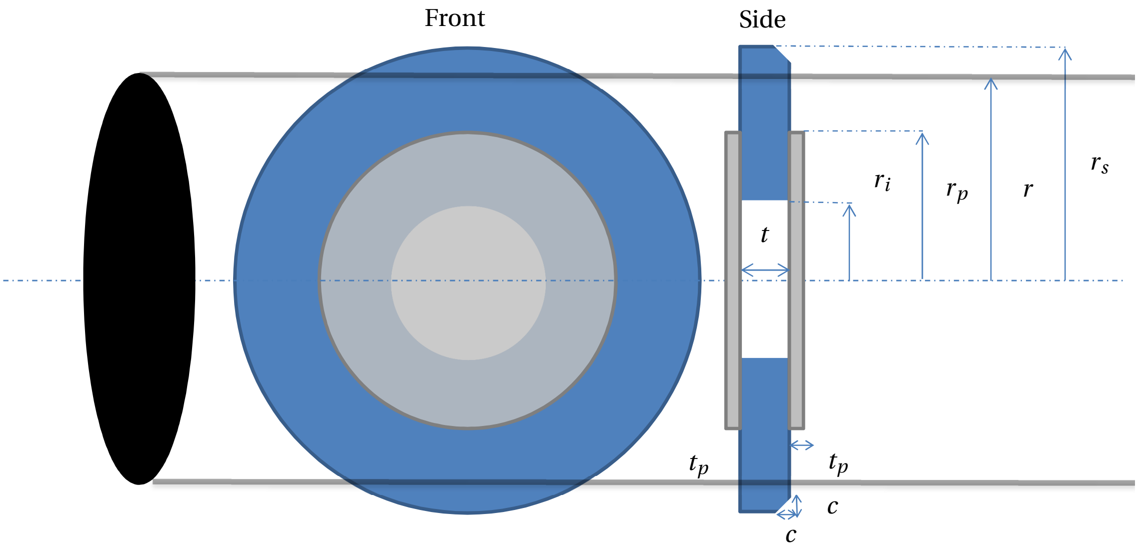

Figure 2.4: A sealing disk clamped between spacer disks with all design dimensions.

In pigging sometimes ratios of the above dimensions are used. Zhu studied the dimensionless groups of the geometry [9]. The four dimensionless numbers are: oversize, clamping rate, thickness, and chamfer.

The oversize is defined as:

$$\delta = \frac{r_s - r}{r} * 100\% \tag{2.1}$$

The clamping rate is defined as:

$$\zeta = \frac{r_p}{r_s} \tag{2.2}$$

Table 2.1: Dimensions of the pig sealing disk drawn in Figure 2.4.

Symbol	Name	unit
r_i	inner radius	m
r_p	spacing disk radius	m
r	inner pipe radius	m
r_s	sealing disk radius	m
t	thickness sealing disk	m
t_p	thickness plate	m
c	chamfer disk	m

The thickness ratio is defined as:

$$\xi = \frac{t}{r_s} \tag{2.3}$$

The chamfer ratio is defined as:

$$\bar{x}' = \frac{c}{r_s} \tag{2.4}$$

Commercial pigs are available from 4” to 60” even though larger pigs (such as the 98” which can be seen in Figure 2.5) exist [5].

Figure 2.5: A very large pig with a weight of over 500 kg used to pig a 2.5 m pipeline. The pipeline, which transports seawater, is made of glass fiber reinforced epoxy and reinforced concrete sections with no internal lining. The pipeline can be subject to natural fouling from marine growth, such as barnacles and mussels [5].

2.1.4. FORCE ON WALL

The pig sealing disk has to be deformed to fit the pipeline. The resistance of a pig sealing disk against deformation creates a normal force on the pipeline wall. Note that when the pig sealing disk is shown in an axisymmetric perspective, the force has the unit Newton per meter circumference.

Linear elasticity is described by Hooke’s law. Hooke’s law describes a linear relation between the stress and the strain in a material. Hooke’s law is often given as an empirical observation, and does not necessarily hold for large deformations. Rubber is an example of a material which behaves highly non-linearly. The material behaviour of rubber can be defined as isotropic, non-linear elastic, incompressible and strain rate independent. Hyperelastic material models (such as the Mooney-Rivlin model) provide ways to model the stress-strain behaviour of such a material [24].

For more information on solid mechanics the reader is referred to "Mechanics of Material" [25] or "Applied Mechanics of Solids" [26].

2.1.5. FRICTION COEFFICIENT

Friction occurs when the surface of an object is in contact with another surface. The most simple form of friction is Coulomb friction which states that the frictional force is less than or equal to the product of a friction coefficient and the normal force. Coulomb friction means that a certain threshold of force needs to be overcome to move an object. If the force acting on the object is equal to or smaller than the friction force, the object will not move. This is formally stated in Equation 2.5 in which F_f is the friction force, μ is the friction coefficient and F_n is the force normal to the surface.

$$F_f \leq \mu F_n \tag{2.5}$$

Coulomb's law is a simple empirical formula, which incorporates many factors that influence the friction force. Friction coefficients for the interaction of two different materials are typically less than one. In the literature the coefficient of friction used for pigs made of polyurethane rubber varies between 0.23 and 0.9 [27] [28] [9] [6] [29]. This wide range shows that little consensus exists on the coefficient of friction for pigs.

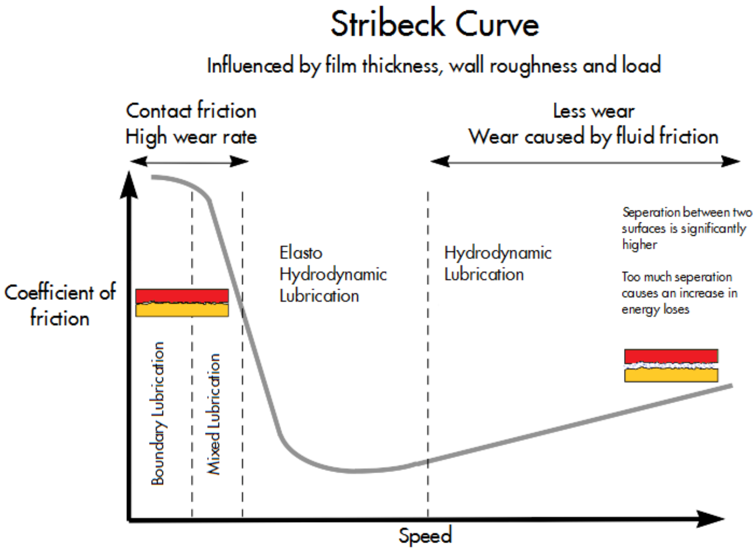

Figure 2.6: The Stribeck curve gives the coefficient of friction between two surfaces as a function of speed. Both values are typically on a log-log scale. In this figure four friction regimes are differentiated.

When two surfaces move over each other with a certain slip velocity the coefficient of friction can be significantly reduced because of lubrication. The typical friction behaviour against the slip velocity is given by the Stribeck curve shown in Figure 2.6. There are four lubrication domains: boundary lubrication, mixed lubrication, elastohydrodynamic lubrication and hydrodynamic lubrication. A clear overview of lubrication theory is given by Hamrock [30].

When a surface is forced against another surface, the surfaces are supported by each others wall asperities. Wall asperities can be envisioned as small cones describing a random height profile. During movement of one of the surfaces the wall asperities will undergo either an elastic or a plastic deformation. When fluid is present between the two surfaces, this fluid can create an upward pressure which reduces the contact between the two surface.

Friction can be divided into four regimes based on whether the surface is supported by either plastically or elastically deformed wall asperities and/or a fluid pressure. Boundary lubrication is defined as the regime in which the load is carried by the surface asperities rather than by the lubricant. During mixed lubrication the surfaces are supported by a mixture of elastically and plastically deformed wall asperities. During elastohydrodynamic lubrication the surface is supported by the lubricant film, but the surface and the wall asperities are still elastically deformed. Hydrodynamic lubrication is defined as the lubrication regime where the load is completely supported by a fluid film.

To describe the friction within these four regimes three physical phenomena need to be taken into account: contact mechanics, surface asperities and fluid film mechanics. During dry friction only contact mechanics and surface asperities are considered.

CONTACT MECHANICS

Contact mechanics describe the deformation of solids at a very localised position. To describe forces on a body often it is valid to rewrite the boundary conditions to simpler concentrated boundary conditions. This is the so-called Saint-Venant's principle. In the case of contact mechanics the concentrated boundary conditions are no longer useful because the interest is in the local deformation. Analytical solutions for contact mechanics problems can for example be obtained from the Hertzian contact equations. Typical Hertzian solutions are available for the contact between a sphere and a half-space and for the contact between a rigid cylinder and a half-space.

For more complex geometries than cylinders and spheres other methods need to be used. An initial approach is the use of the elastic foundation theory, in which the contact is modelled as a row of independent linear elastic springs [31]. For non-Hertzian contact problems (thus involving large strains or friction at contact) the elastic foundation theory gives a large error. Therefore, there are various numerical models to solve the fully linear elasticity equations.

For more information on contact mechanics the reader is referred to 'Contact Mechanics' [31], or 'Computational Contact Mechanics' [32].

ASPERITY MODELS

Asperity models describe the effect of wall roughness on the contact surface(s). Many different asperity mechanics models exist and the reader is directed to papers such as [33] or [34].

One widely used model is the one of Greenwood and Williamson [35]. In that model a rough surface is modelled through a large number of spherical asperities with the same radius of curvature. The asperity heights are described by a Gaussian or an exponential distribution. Furthermore, the asperities are assumed to behave like Hertzian linear elastic spheres. However, also many extensions of this theory to for example plastic deformation or non-spherical asperities exist.

FLUID FILM LUBRICATION

Lubrication is the phenomenon in which the friction (and wear) between two surfaces is greatly reduced by a third medium (gas, liquid or solid) in between them. This can be intentional (as is for example the case in many mechanical applications) or unintentional (as in the case of an aquaplaning car). Lubrication creates a large drop in the amount of friction a surface undergoes as can be seen in Figure 2.6. In this figure the speed is varied, however a more general approach is to vary the lubrication parameter. The lubrication parameter is a dimensionless number defined by:

$$\text{Lubrication parameter} = \frac{\eta u}{F} \tag{2.6}$$

in which η is the viscosity of the lubricant, u is the relative speed between the two surfaces and F is the distributed force in Newton per meter. Note that the coefficient of friction can thus be described as a function of the lubrication parameter .

To describe the fluid film between two surfaces, one can use the Reynolds equations which can be derived from Navier-Stokes. To take the fluid flow phenomena occurring around wall asperities into account Patir and Cheng [36] introduced a modified Reynolds equation.

2.1.6. SPEED

The speed of a pig is determined by the balance between the driving pressure force and the friction force. By creating a bypass the driving pressure force is reduced and therefore the pig will move slower. Pigs typically move with speeds between 1 m/s to 5 m/s [3]. It is trivial that pigs can cause damage to their surroundings when the speed is too high.

2.1.7. DIFFERENTIAL PRESSURE

In this section the differential pressure over the pig is discussed in two parts: firstly the variation of the pressure over the sealing disks is discussed and secondly the description of the driving pressure on the pig is discussed.

SEALING DISK

The differential pressure is defined as the pressure at a certain location at the outer side of a pig minus the pressure just in front of the pig. This differential pressure varies along the pig. O'Donoghue has measured the differential pressure along a pig while the pig moves over a pressure transducer that is mounted at a fixed location in the pipe wall [6]. The result is shown in Figure 2.7.

From these results no conclusions were drawn on the pressure difference between the pig sealing disks. These measurements have been done at different pig velocities. The measured differential pressure ratio between the sealing disks was found to be dependent on the pig velocity. However for multiple runs with the same velocity no reliable relation was found.

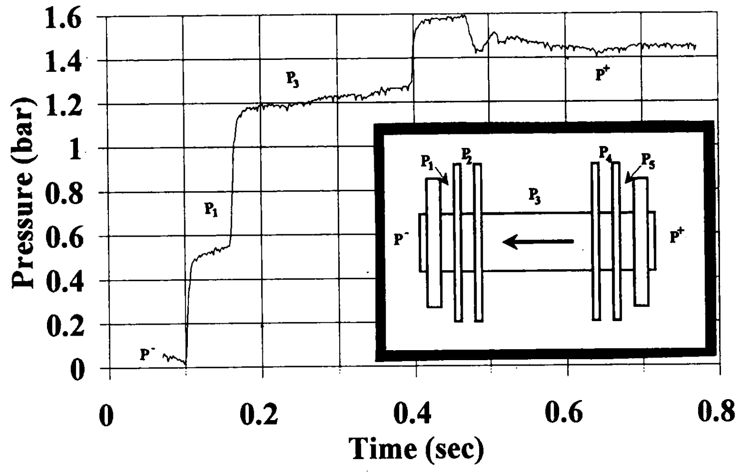

Figure 2.7: The differential pressure over a pig while passing along a pressure transducer in the pipe wall. It can be seen that the guiding disks also give a considerable pressure loss. Secondly it can be seen that the largest pressure drop occurs over the front of the sealing disks [6].

DRIVING PRESSURE PIG

The schematic model shown in Figure 2.2 shows a causal relation from the speed in the direction of the differential pressure. This is explained by the fact that the pressure difference is a function of the mixture velocity of the working fluid and the pig velocity. In the case of a normal pig, the speed equals the velocity of the working fluid (when compressibility effects are neglected). However for a bypass pig the working fluid can pass the pig. In that case the driving pressure is determined by the following equation:

$$\Delta P = 0.5 C_d \rho (u_{\text{mix}} - u_{\text{pig}})^2 \tag{2.7}$$

in which ΔP is the differential pressure over the pig, C_d is the drag coefficient, ρ is the density of the fluid, u_{mix} is the fluid mixture velocity and u_{pig} is the pig velocity. Note that when the pig moves with the velocity of the mixture the driving pressure will be zero and if the pig velocity is zero the driving pressure will be maximal. Therefore, the causality is stated from the speed of the pig to the differential pressure. Note that a higher u_{mix} (velocity of the driving fluid) will of course increase the speed of the pig. However, in this model it is assumed that u_{mix} is an operating condition given as an input parameter.

2.2. PIG FRICTION MODELS

In the following section four pig friction models are briefly discussed and the respective physical phenomena taken into account are given. One of the first and most widely known models is by Cordell and is shown in Figure 2.8 [7]. Cordell's model is very simple, however it is the most used in the industry and considered an industry best practice. Figure 2.8 shows the pressure drop necessary to drive a pig as a function of the diameter and a factor K depending on the type and shape of a pig. This factor K captures all physical phenomena relevant in the friction of a pig. Cordell suggests that the pressure drop scales inversely to the diameter. By making a short derivation this suggests that Cordell uses a constant friction force per meter circumference.

$$\begin{aligned} \text{Driving force on pig} &= \text{Friction of pig} \\ \Delta P \pi D^2/4 &= F_{\text{friction}}[N/m]\pi D \\ \Delta P &= K/D \end{aligned} \tag{2.8}$$

Since this model is widely used in the industry it suggests that the model in this report should be able to give results in a similar way. If a new model gives a new K value it will improve the adoption in the industry. However, the fact that his model is an industry best practice shows that little is known about the pig friction behaviour.

O'Donoghue proposes an approach with a linear elastic large deformation analytic wall force model coupled with an inverse hydrodynamic lubrication (IHL) model [6]. This model is validated with results from a 10" pigging run. This model from 1996 is by far the most complex pig friction model found in the literature.

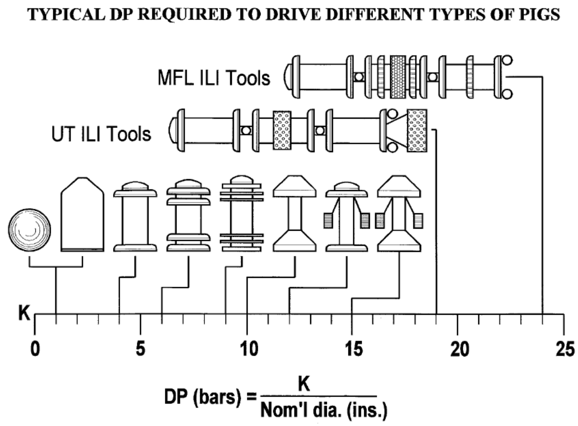

Figure 2.8: A model used to predict the necessary differential pressure over a pig to drive it through a pipeline [7].

In a project of Statoil a 40" high friction pig is used to prevent buckling by filling the pipeline during the laying on the sea floor [8]. To secure that the friction was high enough two independent finite element studies were performed. The finite element analyses gave a radial displacement as a function of the radial force for a coefficient of friction (η) of 0.4 and 0.2. In Figure 2.9 the results of these studies are shown. In the following chapters, graphs like these in which the radial force is plotted as a function of the radial displacement (which directly relates to the oversize) are used to describe the necessary friction force.

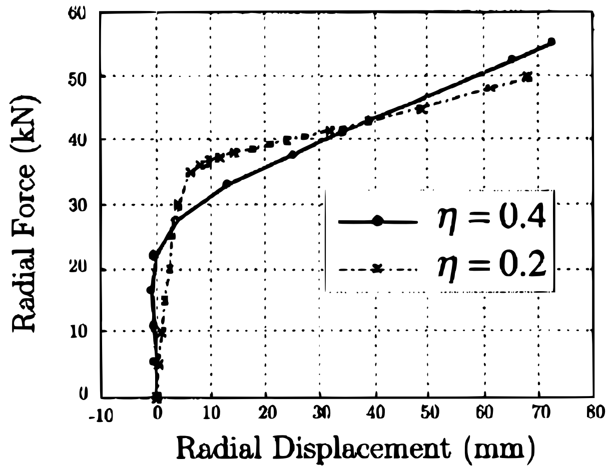

Figure 2.9: Postbuckling responses for a sealing disk considering two different values for the friction coefficient [8].

In 2015 an extensive finite element study was published by Zhu [9]. In this study Zhu uses a Mooney-Rivlin hyper elastic material model in combination with planar elements. The impact of four parameters (oversize, thickness, chamber dimension and clamping rate of the sealing disks) on the contact force and the deflection angle of the sealing disk are studied at different differential pressures over the pig. Zhu does not specify the used coefficient of friction or any consideration of lubrication. The finite element model is validated with pull tests of a pig through a pipe segment and the modelled results are fitted to the experimental results with a coefficient of friction. Multiple references to this modelling approach are given [9] [37].

In Table 2.2 an overview of the modelling approaches used in the four previous models is given. Six different sub models or approaches are differentiated. Firstly, whether a linear or non linear constitutive relation is assumed. Secondly, what kind of kinetics are taken into account. Thirdly, which approach is used to model contact. Fourthly, the kind of asperity model that is used. Fifthly, the lubrication model that is used. And finally how the pressure drop over the disk is taken into account.

The expected error that each approach will bring is indicated with red, yellow or green. Meaning a red approach will bring a significant error and a green approach will be in agreement with the actual physics. Combining all green approaches will already create a better model. However, a model is only as good as its

Table 2.2: An overview of the physical phenomena taken into account in each pigging friction model.

Models	Cordell '92	O'Donoghue '93	Nieckele '01	Zhu '15
Constitutive	Non	Linear	Linear	Non-linear
Kinetics	Type of pig	Fixed	Numerical	Numerical
Contact	Non	Winkler	Non	Slide line
Asperity	Non	G.W.	Non	Non
Lubrication	Non	I.H.L.	Non	Non
Pressure drop	Non	Constant	Constant	Constant

validation. Therefore, in the following section some pig friction experiments will be discussed.

2.3. PIG FRICTION EXPERIMENTS

Often in experiments only the friction force necessary to move a pig through a pipeline is measured. The wall force the sealing disk applies on the pipeline wall in those cases remains an unknown. The speed which will initiate the lubrication between the sealing disk and the pipeline wall can cause a large decrease in the coefficient of friction. Therefore the experiments found in the literature are discussed in two parts. First, wall force experiments are discussed for dry friction. Second, experiments to investigate the lubrication behaviour are discussed.

The pressure drop over this pig only forms a small part of this thesis. Many decisions made were based upon earlier work. For a broad review of done work on this subject the reader is referred to the thesis done by Azpiroz [38] or the thesis done by Liang [39].

2.3.1. WALL FORCE + FRICTION EXPERIMENTS

Pigging friction experiments described in the literature can be divided into three categories: pig pull tests, open scrape tests and pipeline pigging tests. Examples of pig pull tests and open scrape tests are shown in Figure 2.10. A pig is propelled with pressurized air or water in a pipeline. In addition to these three experiments also pressure drop measurements over a pig during field runs exist. The main result from these experiments is the force or the pressure drop necessary to move the pig.

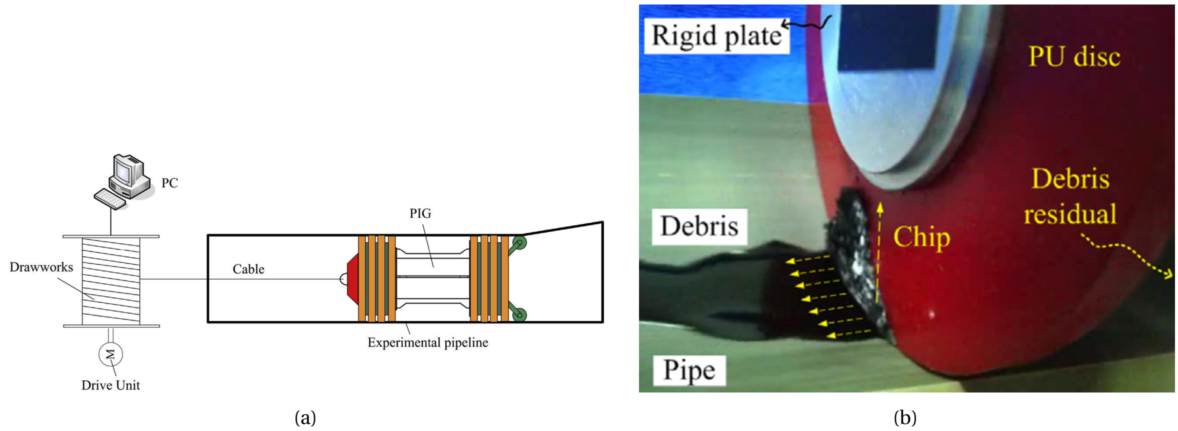

Figure 2.10: (a) An overview of a typical pig pull test given by Zhu [9] (b) A scraping test on the influence of wax deposits on the frictional behaviour of pig sealing disks. [10]

In the framework it is shown that the coefficient of friction is an important parameter in predicting the friction force of a pig. This coefficient of friction is not a material property, but a ratio between the force normal to the surface and parallel to the surface. Also the coefficient of friction can vary depending on at least: material properties, the load (F_{wall}), and wall roughness. We are not aware of any experiments in the literature in which both F_{wall} and F_{friction} are measured for an actual pig.

Some sources report measurements of μ. How these values are found however is not always clear. Sometimes the coefficient of friction is found by simple desktop experiments in which the angle of inclineation is measured before the disk starts slipping [6]. The coefficient of friction can also be found by standardized tests. These tests measure the coefficients of friction for the used material in combination with a different material, with or without lubricants and/or for various speeds [40]. An example of how the coefficient of friction is used to compare a model with an experiment is given next.

Zhu measures F_{friction} by a pig pull test to validate the results from his finite element model [9]. To do this the coefficient of friction is needed which is obtained by a "friction and wear test" in dry and oily circumstances. In the friction and wear test a value of μ is obtained which is between 0.5 and 0.6. With these values the model has a minimum relative error of 6.13% and a maximum relative error of 27.35 %.

2.3.2. LUBRICATION EXPERIMENTS

Furthermore litle is known about the effect of lubrication on pigging. Little effort has been done to relate the experiment results to the lubrication phenomena. The one exception on this is the work done by O'Donoghue [6]. O'Donoghue tries to research lubrication with pig runs in a 15 km long 10 inch diameter test facility, with the ability to loop the pig to achieve pig runs up to 200 km.

Because of the computational power available at that time O'Donghue uses a simplified model. O'Donoghue reports that the model is in quantitative agreement, however it is not able to predict certain phenomena such as forward leaking.

The lubrication obtained in this test facility was limited. No visual inspection of the pig was done and the use of air and water limits the lubrication. By using oil as a working fluid the lubrication can be orders of magnitude higher.

2.4. RESEARCH OUTLINE

First the relevant phenomena were discussed and the most important parameters defined. The complex relation between the input parameters and the output parameters are described by models. Examples are CFD models to find a drag coefficient for different Reynolds numbers or lubrication models to match the coefficient of friction to the lubrication parameter.

Zhu has published a sophisticated finite element study into the wall force. However, the validation done in this study uses a coefficient of friction found in external tests. Therefore, the interpretation of the validation results is not unambiguous. In this thesis an analytical model and a finite element model are made, respectively, similar to the ones given by O'Donoghue [6] and Zhu [9]. These models are discussed in Chapter 3. The design, measurement results and model validation with a new experiment which measures both the coefficient of friction and the wall force are given in Chapter 4. Even though the coefficient of friction is measured in Chapter 4, these measurements did not result in a constant coefficient of friction applicable in practice. The results should rather be interpreted as the other way around. For a fixed coefficient of friction the wall force was measured.

O'Donoghue proposed a more sophisticated soft elastohydrodynamic lubrication model, but was not able to perform the actual calculations. In Chapter 5 a soft elastohydrodynamic model is built. The model uses the Winkler springs as proposed by O'Donoghue. This limits the accuracy since it assumes that linear elastic behaviour can be described with a row of closely spaced springs which do not interact. In the case of actual linear elastic contact the difficulty of course is that the displacement at any point interacts with the pressure at any point. The Winkler spring approach therefore is very approximate.

Johnson [31] (the reference in respect to the used Winkler spring model) suggests multiple numerical techniques to extend this model to actual linear elasticity. One of these methods is the boundary element method. Although it is not necessarily better than the other options (such as the finite element method or a multigrid method), the boundary element method is a very elegant method which can solve a contact problem by linear elasticity or a fluid film problem by Stokes flow.

In this thesis the boundary element method is used to build a more accurate lubrication model. The boundary element method is so elegant because it allows the user to describe a problem by just the boundary. This is unlike the finite element model in which the boundary and the interior of a domain needs to be discretized. The boundary description allows a reduction of dimension while describing the problem. This means that it can describe a 2D domain by a 1D boundary line. Therefore, the boundary element method is numerically very efficient. When the solution for the boundary is known the exact solution can be found at any point inside the domain. Therefore, the boundary element method is also very accurate.

Although this sounds very pleasant, these advantages are met by the fact that according to Becker [41] [42] the numerical implementation of the boundary element method is plagued by: *'a mathematical monster that leaps out of every page'*. In this thesis the reader is referred to other sources for mathematical monsters, since the given derivation is very concise.

Firstly a general purpose boundary element code is written in Matlab and compared to the analytical results for a Bernoulli beam in Chapter 6. This Matlab code is coupled to the model that describes the mechanics of lubrication in Chapter 7.

The opportunity arose to do pressure drop measurements over a model pig in a flow loop. The purpose of these experiments was to validate the already performed CFD studies. In Chapter 8 these flow loop experiments are discussed.

2.5. CONCLUSIONS

A framework was made in which multiple pigging models can be compared. With this framework four models from the literature are analysed. The used models were compared and a quick assessment of the accuracy has been made. The comparison of current models indicates possible improvements of current pigging models.

Also available experimental validations are analysed. It was shown that most experiments measure the friction. The wall force (or radial force) typically given by models is lost. Since this gap is identified, this thesis focusses on closing this gap. Only a limited amount of work on pig lubrication is found. The found work is relatively old (1996) en was limited by the available computational power. In this thesis a more accurate lubrication model is made with the help of the elegant boundary element method. Finally, the outline of this thesis was given.

3

WALL FORCE MODEL

In this chapter models are discussed to describe the force of the rubber sealing disk on the wall. First, the parameters and definitions are introduced. The model discussed here is based on an analytical model for large deformation disks found in the literature [6]. In subsequent order the kinematics and the momentum balance of the model will be discussed. Next to the analytical model a finite element model is built with the commercial software package Femap. The results from the finite element model are used to validate the analytical model. Finally conclusion on the comparison between the finite element model and analytical model are drawn.

3.1. ANALYTICAL MODEL

To reduce complexity a single sealing disk is analysed in a 2D axisymmetric perspective. After the analysis has been made, it is easy to repeat it for multiple disks. The mass is not taken into account in this analysis. This is allowed since Zhu showed that for an oversized sealing disk the total force contribution by the mass on a disk is zero [9].

The spacer disks and pipeline walls are assumed to be rigid. This assumption is acceptable since the stiffness of steel is typically 30000 times higher than the stiffness of the used sealing disk rubber. The spacer disk has no other purpose than restricting the movement of the sealing disks and therefore little engineering rules are known.

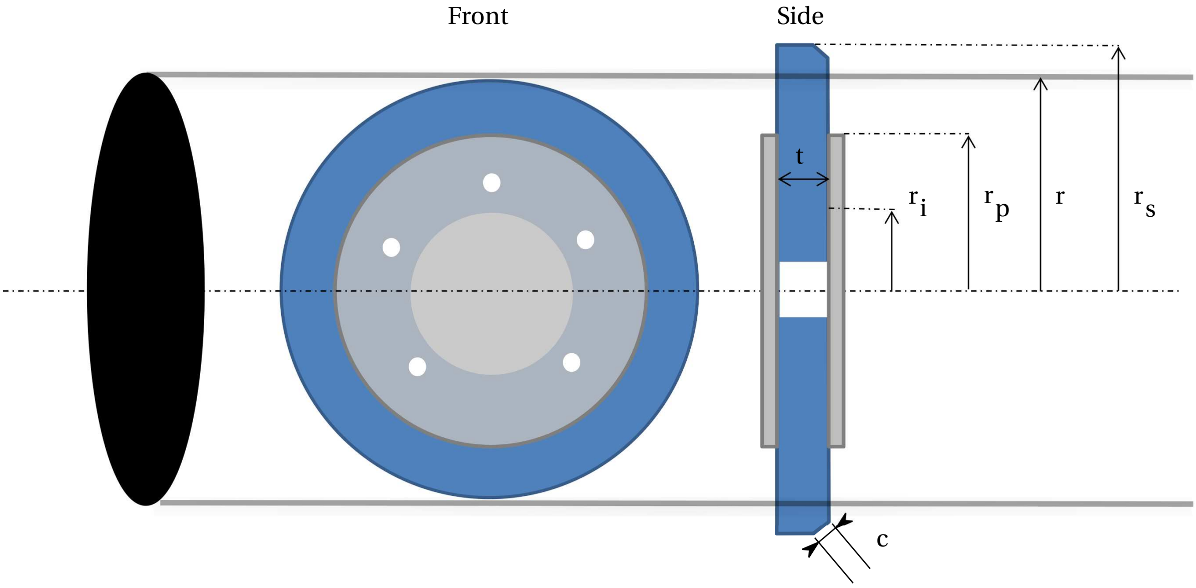

Figure 3.1: Definition sketch of the parameters describing the geometry of a pig sealing disk. These parameters are: the sealing disk radius (r_s), the pipe radius (r), the spacer disk radius (r_p), the sealing disk inner radius (r_i), the thickness (t), and the chamfer length(c).

In Figure 3.1 the relevant parameters of a sealing disk are shown. In the industry often not the specific parameters, but dimensionless ratios such as the oversize and clamping rate are used. The oversize and clamping rate are defined as:

$$\text{Oversize} = \frac{r_s - r}{r} \tag{3.1}$$

$$\text{Clamping rate} = \frac{r_p}{r_s} \tag{3.2}$$

First the kinematic model is discussed. In this section the deformation of the sealing disk is described by an arc with a constant curvature. This choice will help to describe the large deformation effects.

> Assumption: The deformation of the pig sealing disk can be described by an arc with constant curvature and constant length. Therefore, the sealing disk radius r_s, and sealing disk thickness t are assumed to be constant.

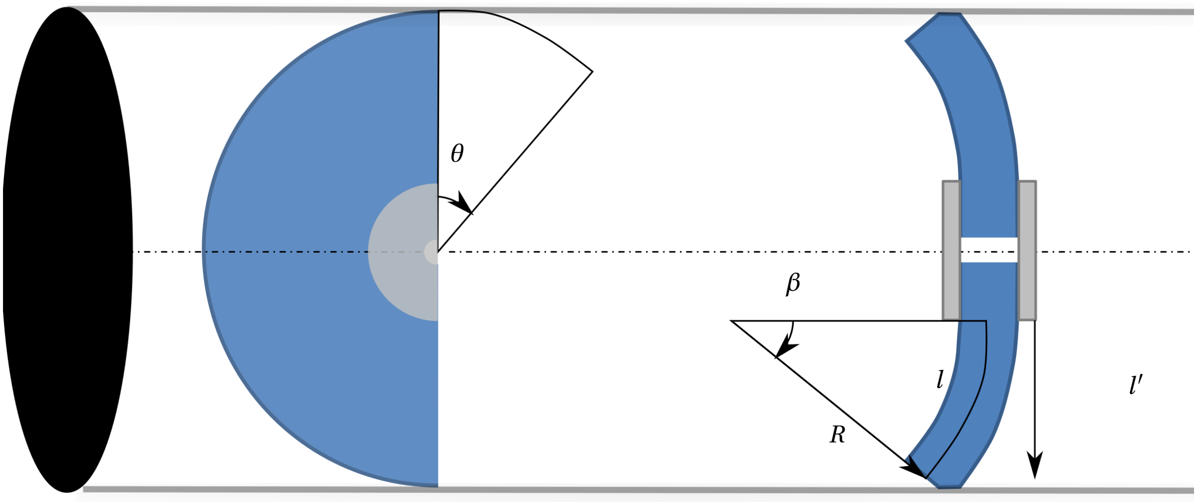

Figure 3.2: The kinematic model of the deformed sealing disk described by: centre length l, projected height l', angle β, radius R and circumferential dimension θ.

In Figure 3.2 the deformed pig sealing disk is shown. The centre line of the sealing disk is described by an arc with radius R and angle β. It is assumed that the centre line has a constant length l and a projected height l'. The length and projected height can be calculated with Equation 3.3 and 3.4, respectively:

$$l = R * \beta \tag{3.3}$$

$$l' = R * \sin(\beta) \tag{3.4}$$

By assuming no radial compression, i.e. there is only bending and circumferential compression, l is assumed to be constant. By this assumption l can be related to the sealing disk radius minus the spacer disk radius. Note that l therefore is assumed constant. The projected height is related to the disk geometry by using: the spacer disk radius, the pipe radius, the thickness, and the chamfer. Chamfer is the worn edge along the sealing disk and in this analysis it is defined parallel to the pipe wall. Note that some sealing disks have a machined chamfer and in these cases the geometry should be described accordingly. In this analysis chamfer is denoted by c and defined by its length. This is shown in Figure 3.3. The equation describing the centre line arc can be related to the sealing disk geometry by Equation 3.5 and 3.6:

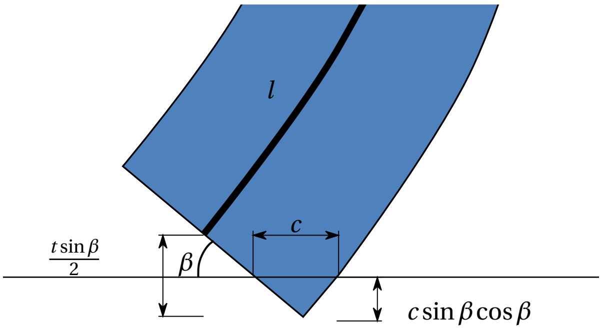

Figure 3.3: Close up of the contact area of the sealing disk. The worn edge runs parallel to the pipe wall and is described by a contact length c.

$$l' = r - r_p - \frac{t * \sin(\beta)}{2} + c\sin(\beta)\cos(\beta) \quad (3.5) \qquad\qquad l = r_s - r_p \quad (3.6)$$

By combining Equation 3.3 - 3.6 four independent equations are obtained. The input values are: r, r_s, r_p, t, and c. The four output values are: R, β, l, and l'. The Newton-Raphson method is used to solve these equations as is shown in Appendix A.

In Figure 3.4 all forces, stresses and pressures are shown for the deformed geometry. A distinction is made between external moment and internal moment. By using the deformation of the sealing disk a moment balance can be made. Because the described model is static, the sum of the internal moments and external moments should be equal to 0. For simplicity the moment balance is considered around point A. Five different force and moment contributions are distinguished:

- M_w caused by the force normal to the pipeline F_{wall}
- M_f is related to the friction force F_{friction} which is parallel to the pipeline wall
- $M_{\Delta P}$ from the pressure drop ΔP normal to the sealing disk surface
- Internal momentum $M_{c/t}$ from the compressive and tensile bending stresses σ_t and σ_c
- Internal momentum M_θ from the hoop stress σ_{hoop} caused by circumferential compression

In the following section an expression for each moment is given. A full derivation is given in Appendix A. To derive the following equations, it is assumed that the material follows Hooke's law.

> Assumption: The material of the pig sealing disk can be described by linear elasticity as given by Hooke's law. This law describes the relationship between stress and strain with an E-modulus (E) and a Poisson's ratio (ν).

The moment in point A caused by the wall force can be expressed as:

$$M_w = F_{\text{wall}}\left(R(1-\cos(\beta)) - \frac{t\cos\beta}{2}\right) r\,d\theta \tag{3.7}$$

The moment in point A caused by the friction force can be expressed as:

$$M_f = F_{\text{friction}}(r - r_p)\,r\,d\theta \tag{3.8}$$

Both F_{wall} and F_{friction} have the unit N/m and are defined as N per meter circumference. By assuming a constant coulomb friction coefficient (μ), F_{wall} can be related to F_{friction} by:

$$\mu F_{\text{wall}} = F_{\text{friction}} \tag{3.9}$$

The moment in point A caused by the pressure difference over the pig sealing disk is expressed as:

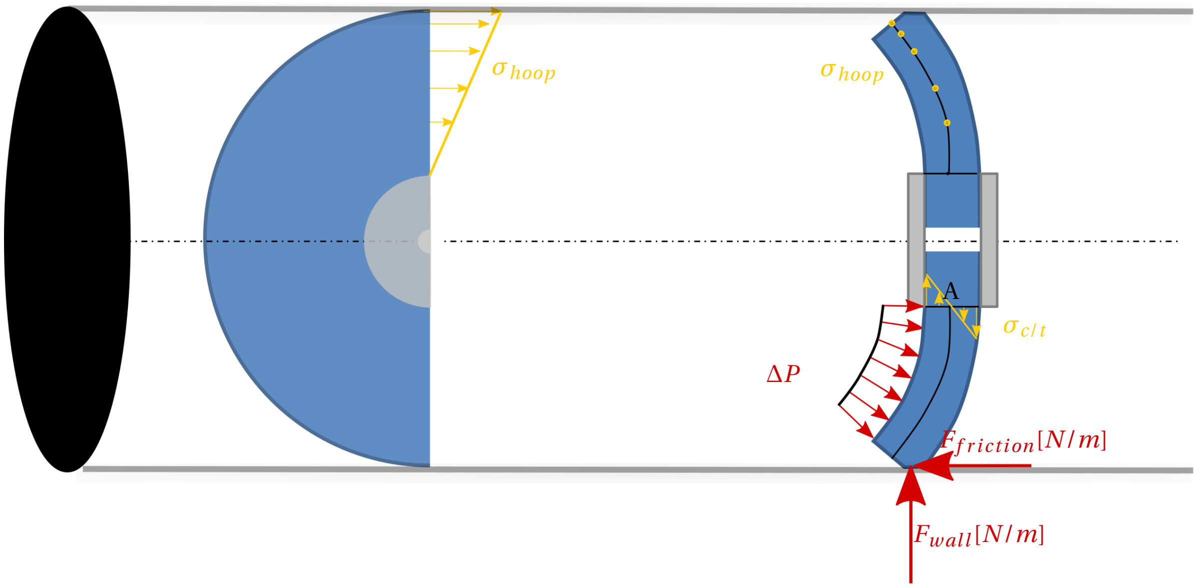

Figure 3.4: Relevant forces and stresses applied on a deformed sealing disk. The wall force and friction force are denoted, respectively by F_{wall} and F_{friction}. Note that both are defined per meter circumference. The external pressure is denoted by ΔP. The external forces and pressure are balanced by: compression stress σ_c, tensile stress σ_t, and hoop stress σ_{hoop}.

$$M_{\Delta P} = \Delta P * R_{\Delta P}^2 d\theta * \left(\frac{R_{\Delta P}\beta}{2} - \frac{R_{\Delta P} * \sin(2\beta)}{4} + r_p * (1 - \cos(\beta)) \right) \tag{3.10}$$

in which ΔP denotes the pressure drop in Pascal and $R_{\Delta P} = (R - t/2)$.

To describe the stress-strain relationship the E-modulus (E) and Poisson's ratio (ν) are used. Note that in Equation 3.12 and 3.13 the moment is recognized as the moment-curvature relation which is typically used for pure bending. In the moment-curvature relation the moment of inertia is given by:

$$I = \frac{t^3 r_p d\theta}{24} \tag{3.11}$$

The moment in point A induced by the compression and tension bending stress can be expressed as:

$$M_c = \frac{t^3 E r_p d\theta}{24R} \tag{3.12}$$

$$M_t = \frac{t^3 E r_p d\theta}{24R} \tag{3.13}$$

The moment in point A caused by the hoop stress can be expressed by Equation 3.14. This integral does not have an analytical solution and therefore has to be evaluated numerically. Since the contribution of the stress is integrated over the angle β, a dummy variable α is used which runs from 0 to β:

$$M_\theta = \frac{ER^2 t d\theta}{(1-\nu^2)} \int_0^\beta \frac{\alpha - \sin(\alpha)}{\alpha + \frac{r_p}{R}} (1 - \cos(\alpha)) d\alpha \tag{3.14}$$

Finally, the following moment balance is made:

$$M_f + M_w - (M_{\Delta P} + M_t + M_c + M_\theta) = 0 \tag{3.15}$$

The value $d\theta$ appears in every momentum contribution and therefore can be divided out. When the deformation and pressure are known, F_{wall} can be expressed explicitly as:

$$\frac{M_{\Delta P} + M_t + M_c + M_\theta}{\left(R(1-\cos(\beta)) - \frac{t\cos\beta}{2}\right) r d\theta + \mu(r - r_p) r d\theta} = F_{\text{wall}} \tag{3.16}$$

By combining Equation 3.7 - 3.15 eight independent equations are obtained. The input values are: R, β, r, r_p, t, μ, ΔP, E, and ν. The output values are: M_w, M_f, F_{wall},$M_{\Delta P}$, M_{rt}, M_{rc}, M_θ, and F_{friction}.

In the case that ΔP is also unknown one additional equation can be used. When the pig is in motion the driving pressure is equal to the friction force and therefore:

$$\Delta P \pi r^2 = F_{\text{friction}} 2\pi r \rightarrow \Delta P = \frac{2F_{\text{friction}}}{r} \tag{3.17}$$

By using this equation F_{wall} can be expressed explicitly as:

$$\frac{M_{rt} + M_{rc} + M_\theta}{\left(R(1-\cos(\beta)) - \frac{t\cos\beta}{2}\right) r d\theta + \mu(r - r_p) r d\theta - (2\mu/r) * R_{\Delta P}^2 d\theta * \left(\frac{R_{\Delta P}\beta}{2} - \frac{R_{\Delta P} * \sin(2\beta)}{4} + r_p * (1-\cos(\beta))\right)} = F_{\text{wall}} \tag{3.18}$$

The Matlab function of these equations is presented in Appendix C.

3.2. FINITE ELEMENT MODEL

By using finite element software, the two main assumptions of the previous section are tested. First the assumption of linear elasticity is checked by comparing a linear material model to a non-linear Rivlin material model. Secondly the assumption of the constant curvature is checked by comparing the analytical model to the finite element model. Here a deviation of 1.45 is seen. After this is done the deformed geometry of the analytical model is compared with the deformed geometry of the finite element model.

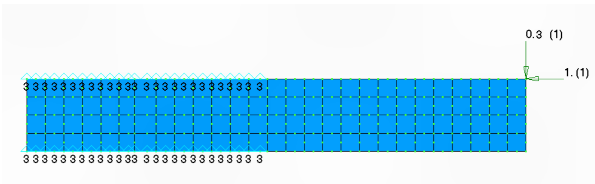

Figure 3.5: Finite element mesh of a sealing disk in axisymmetric perspective. Two forces respectively in the axial and radial direction are applied by function 1. The radial direction is multiplied by 1 and the axial direction by 0.3. Thereby a coefficient of friction of $\mu = 0.3$ is used. The mesh is constrained in direction '3', meaning that the disk cannot move in the axial direction.

The finite element model is shown in Figure 3.5. The dimensions are based on a commercial Baker Hughes disk with: thickness $t = 15$ mm, a sealing disk radius $r_s = 0.1615$ m and an inner radius of $r_i = 0.0585$. In this and the following chapter no wear is taken into account and so $c = 0$.

The fixation is modelled by fixating the nodes at the location of the spacer disk in the axial direction. The wall force and friction force are applied by a function (1) and coupled with a coefficient of friction μ of 0.3 . Solving the model will result in a range of translations at the point where the force is applied. The translation Δr in the radial direction is related to the oversize by oversize $= \Delta r/(r_s - \Delta r)$.

The geometry is built in Femap 11.0.0 64-bit and solved with the advanced non-linear solver Adina 601. Axisymmetric 2nd order quadrature elements are used. The model has been checked for grid convergence by refining the mesh by a factor 4 from 108 to 432 elements. The smaller elements showed some difficulty at locations where the force was applied which was solved by using rigid elements. The forces for F_{circ} changed by less than 1% when the iteration process was stopped.

3.2.1. COMPARISON NON-LINEAR FEM MODEL WITH LINEAR FEM MODEL

The disk material is specified as 75 Shore hardness (S_A) with which an initial estimate of the E-modulus can be obtained by the Gent equation [43]. However, because of the large deviation between the Gent equation and the non-linear material model a new E-modulus was fitted by choosing a value which was in agreement with the non-linear material model at 3% oversize and 53.25 % clamping rate. Due to the derivation of the strain it is not possible to use a Poisson's ratio of 0.5. This is explained in more detail in Appendix B.4. For a Poisson's ratio of $\nu = 0.45$ an E-modulus of 12.25 MPa is found. The non-linear material is defined by a Rivlin material model which is fitted with the least squares algorithm in Adina to axial strain experiments [44]. For more information about the Gent relation, the axial strain experiments and the material model the reader is referred to Appendix B.

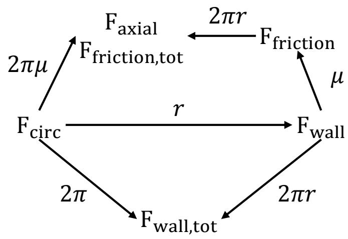

Figure 3.6: Conversion model.

The results from the finite element model for different clamping ratios are shown in Figure 3.7 given in force per radian. This unit directly relates to the outcome of the experiments done in Chapter 4. In this report values for the necessary force to pull a disk through (F_{axial}), the wall force per radian (F_{circ}), the actual wall force ($F_{wall,tot}$), the wall force per meter circumference (F_{wall}), and the friction force per meter circumference ($F_{friction}$) are used. This can lead to confusion and therefore the necessary conversion is given in Figure 3.6.

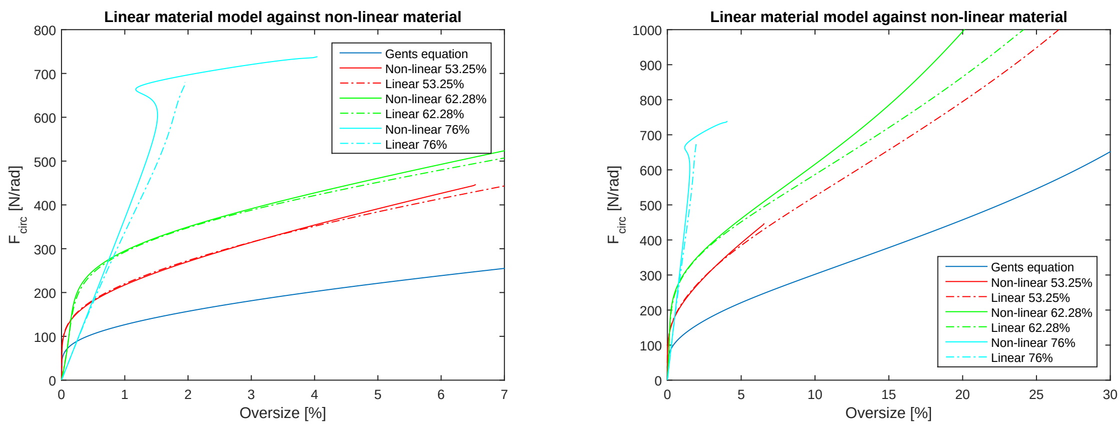

(a) (b)

Figure 3.7: Difference between the linear and non-linear material model for a range of clamping rates. The used mesh is shown in Figure 3.5 in which the constraints are varied. The linear material is described by an E-modulus of $E = 12.25$ MPa and $\nu = 0.45$. The non-linear material is defined by axial strain tests as described in Appendix B.

Firstly it must be noted that the Gent relation, which is widely used in the industry, underpredicts the actual E-modulus. In the relevant oversize range a linear E-modulus describes the non-linear material behaviour reasonably accurate. The high clamping rate model shows numerical difficulties. Because of the high clamping rate, the deformed position where the load is applied only moves beyond the centre of the fixation after some time. The deformation therefore closer resembles a plane strain compression than a bending deformation. This bending deformation suddenly occurs when the axial deformation passes the applied load past the disk centre.

From Figure 3.7(b) it can be concluded that even beyond the relevant oversize range the linear material model shows good agreement with the non-linear material. The higher clamping rate causes higher strains at a similar oversize. Therefore, the influence of non-linear material is expected to be larger for higher clamping rate geometries.

In Figure 3.8 the influence of the thickness on the non-linear material behaviour is tested. Overall the behaviour of the non-linear material can be approximated by a linear material with an E-modulus of 12.25 MPa.

3.2.2. Comparison analytical model with linear FEM model

In the following part the assumption of the kinematic model is validated. Therefore, the results of the analytical model will be compared to the results from the FEM model. Again the clamping rate and thickness are varied

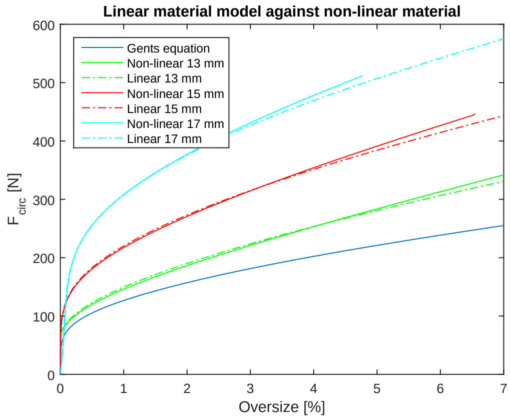

Figure 3.8: Difference between the linear and non-linear material model for a range of thicknesses. The used mesh is shown in Figure 3.5. For thicknesses other than 15 mm the mesh is displaced evenly. The constraints are kept constant to resemble a 53.25% clamping rate. The linear material is described by an E-modulus of $E = 12.25$ MPa and $\nu = 0.45$. The non-linear material is defined by axial strain tests as described in Appendix B.

along a range of oversize's. The results are shown in Figure 3.9.

A deviation of 45% was noted between the analytical model and the FEM model. O'Donoghue, who uses a similar analytical model, reports that his analytical model gives wall force values that are between 30 - 50 percent less than his FEM model [6]. The kinematic model does not have the ability to compress in the radial direction. Therefore, the analytical model overpredicts the arm from where the forces are applied which is compensated by underpredicting the forces. The length of the arm can be seen in Figure 3.4, or with the defined length in Figure A.1. The analytical model is also validated by applying a moment (therefore not applying radial compression). The deviation between the moment loaded FEM model and the analytical model was less than 3%. This 3% deviation could be traced back to local deformation of the model.

To correct for the limitations of the kinematic model a linear correction factor C is introduced. When corrected with $C = 1.45$ both models are in agreement for both the different thicknesses and clamping rates. The results of the corrected analytical model are shown in Figure 3.10. A comparison with the non-linear material against the 76% clamping rate case was shown in Figure 3.10(c). The initial compression is not in agreement with the analytical model. However, when the geometry is in the bending mode the analytical model is in agreement.

3.2.3. Comparison deformed shape analytical model and FEM model

In Figure 3.11 the geometry of the analytical model is compared with the geometry of the finite element model. The used disk is described by a sealing disk radius of 0.1615. The linear material for both models is defined by an E-modulus of $E = 12.25$ MPa and a Poisson's ratio of 0.45. The geometry is 15 mm thick with a spacer disk with a radius of 0.086 m. The deformed geometry is shown for 1% to 6% oversize.

The deformation assumed in the analytical model is in agreement with the deformed geometry from the finite element model. It must be noted that probably more accurate kinematic model can be found (higher order polynomials). In this thesis no further research into this has been done.

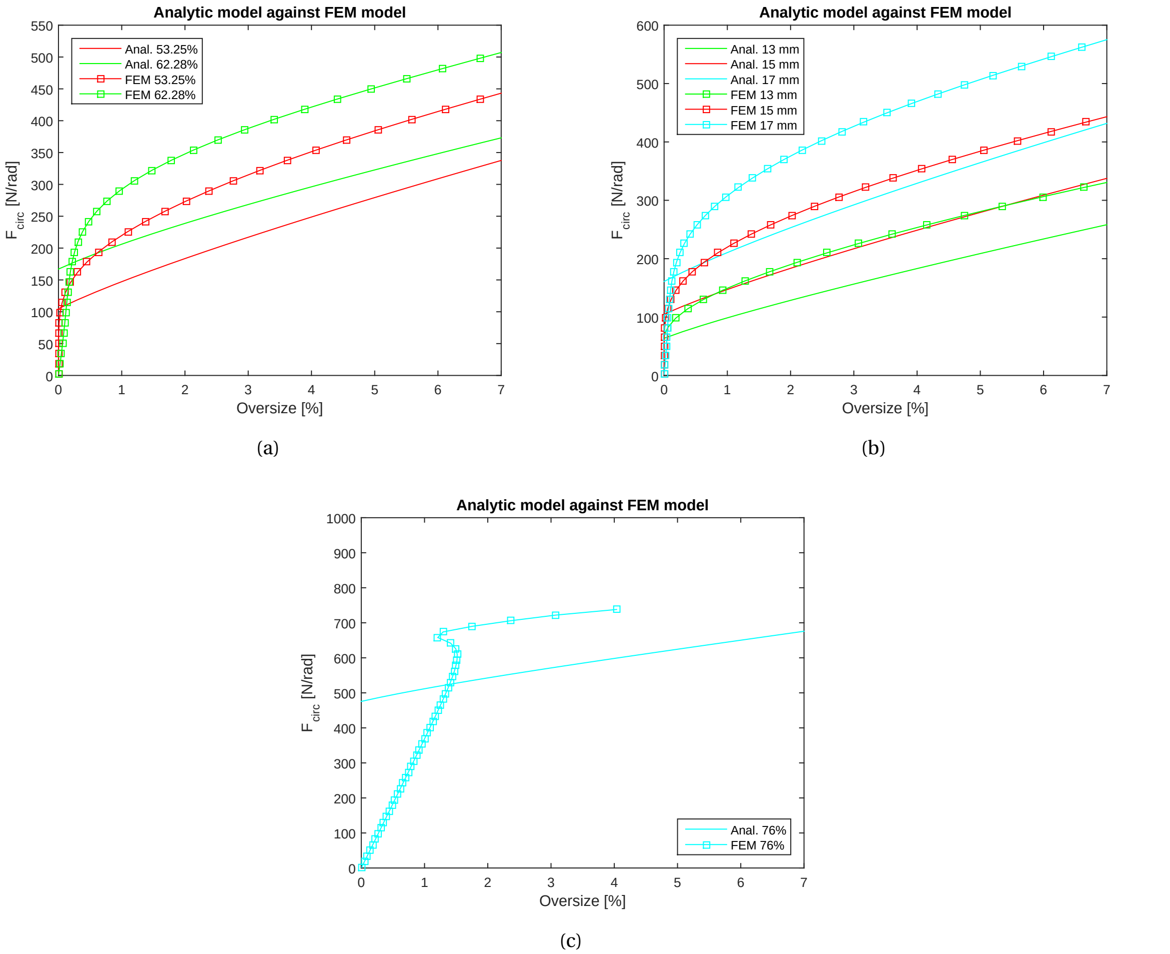

Figure 3.9: Comparison of the linear finite element model results with the linear analytical model results. The used disk is a 75 Shore Baker Hughes disk of $r_s = 0.1615$. The linear material for both models is defined by an E-modulus of 12.25 MPa and a Poisson's ratio of 0.45. Unless otherwise stated the geometry is 15 mm thick with a clamping rate of 53.25%.

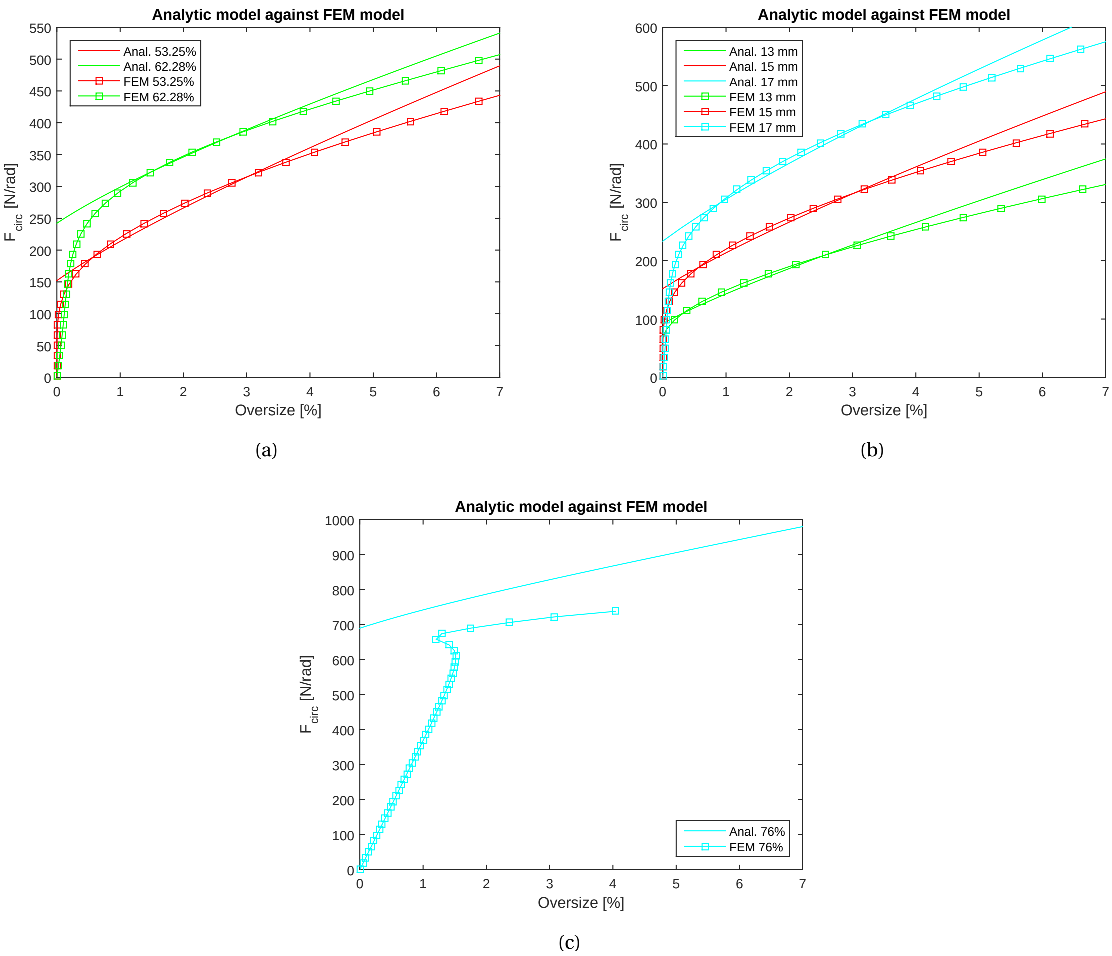

Figure 3.10: Comparison of the linear finite element model with the linear analytical model to test the influence of the used kinematic model. The influence of the limitations of the kinematic model are large and therefore the results are multiplied with a linear correction factor of 1.45. The used disk is a 75 Shore Baker Hughes disk of $r_s = 0.1615$. The linear material for both models is defined by an E-modulus of $E = 12.25$ MPa and a Poisson's ratio of 0.45. Unless otherwise stated the geometry is 15 mm thick with a clamping rate of 53.25%.

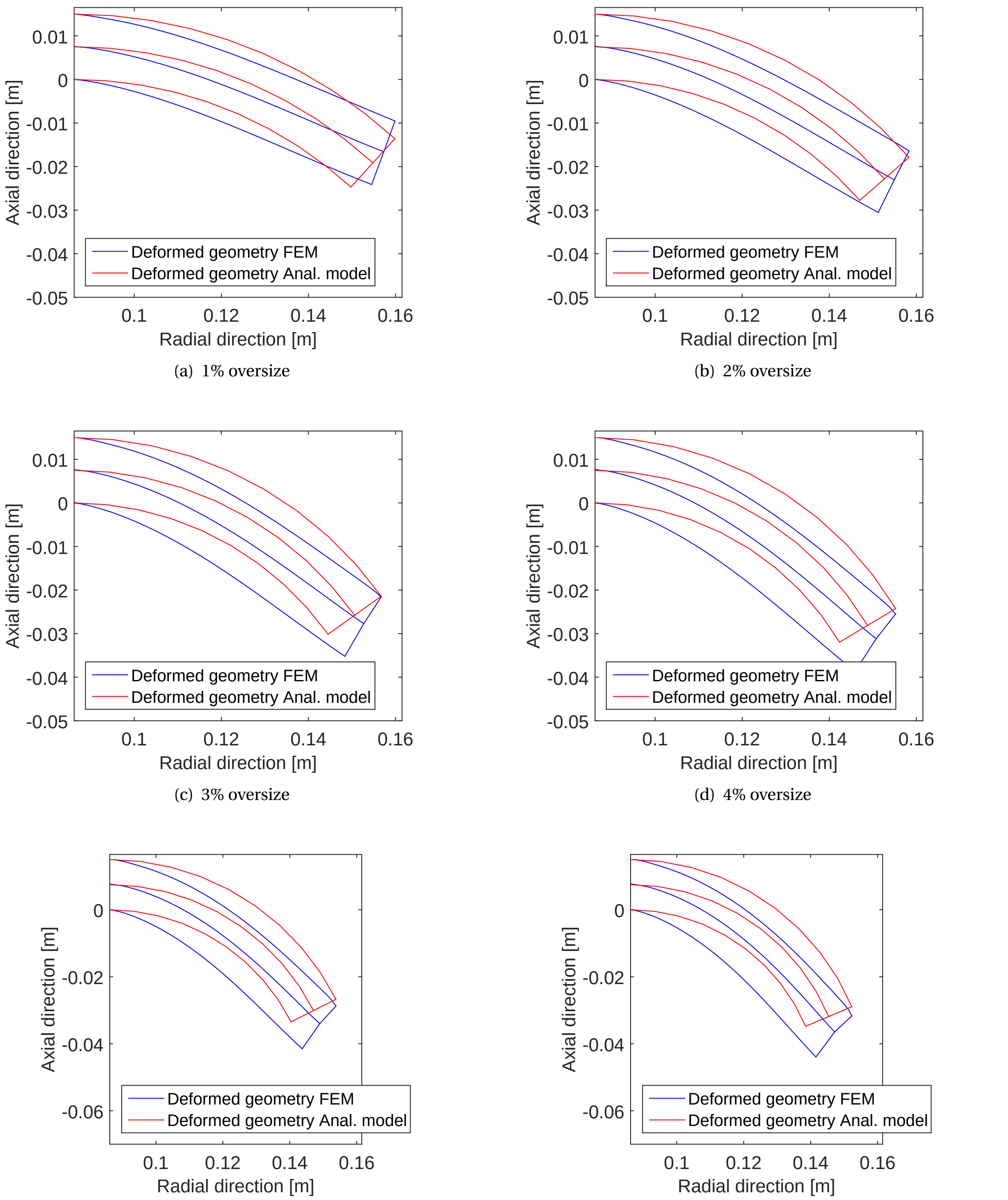

(a) 1% oversize

(b) 2% oversize

(c) 3% oversize

(d) 4% oversize

(e) 5% oversize

(f) 6% oversize

Figure 3.11: Deformed geometry for 1% to 6% oversize for both the analytical model and the finite element model with a linear E-modulus.

3.3. CONCLUSIONS

In this chapter the definitions to describe the sealing disk geometry were given. With these parameters an analytical model has been made to predict the necessary force to deform a sealing disk. To validate the analytical model a FEM model has been made. The FEM model with non-linear material from the axial strain test showed that the currently used Gent relation was inaccurate. A new linear E-modulus was obtained to fit linear material with the non-linear model. After this was done, the analytic model was compared with the FEM model. A constant deviation of 45% was found. The analytical model with a constant correction factor of 1.45 was shown to be in agreement with the FEM model. This analytical model and FEM model will be checked with an experiment in the following chapter.

4

SEALING DISK EXPERIMENTS

To measure the necessary force to move a pig sealing disk through a pipe various experiments have been done in the literature. In Section 4.1 a new experimental design is discussed for which the measurement procedure is described in Section 4.2. In Section 4.3 the measurements results are presented. The results from the experiment are compared to the analytical model from the previous chapter. To compare multiple disks additional experiments with disks from a different vendor were performed. This is discussed in Section 4.4. Finally, a conclusion is drawn to how the analytical model compares to the performed experiments.

4.1. DESCRIPTION OF THE EXPERIMENT DESIGN

In this thesis an experiment is presented in which both F_{wall} and F_{friction} are measured. Therefore, μ is no longer an unknown and a clear comparison between the experimental and numerical results can be made.

To measure the steady state friction force and normal force, between the disk and the wall, a dedicated experiment was designed and built. This facility, as shown in Figure 4.1, allows to carry out pull tests.

To measure the normal force on the wall (F_{wall}) a metal ring is fabricated which can be tensioned to reduce the radius of the ring. The force necessary to tension the ring is measured by a load cell. The measurement value for the load cell is called F_{circ} and can directly be related to the distributed force F_{wall}. To impose the distributed force F_{friction} a second force is applied in the axial direction.

It is chosen to directly apply the force on the disk. To make the system as stiff as possible a metal threaded rod is used. A tensioning bolt on the threaded rod can be turned to pull the disk. The force on the threaded rod is measured by a second load cell and is called F_{axial}. To prevent the disk from moving skew a sleeve is welded on the spacer disk. This sleeve is supported in a guiding beam to prevent rotation or translation in any other direction than the axial direction.

The experiment is shown in Figure 4.1.

The method of conservation of work is used to relate F_{circ} to F_{wall}. A definition sketch is given in Figure 4.2. Note that since the distributed wall force is defined per meter circumference the total force on the pipeline wall equals $F_{\text{wall}}2\pi r$. For conversion to other values the reader is referred to Figure 3.6. The energy necessary to move the rubber disk inward must be equal to the work done at the end of the ring by the tensioning mechanism. Therefore, we write:

$$\begin{aligned}\text{internal energy} &= \text{external energy}\\ F_{\text{wall}}2\pi r\Delta r &= F_{\text{circ}}2\pi\Delta r\\ F_{\text{wall}}r &= F_{\text{circ}}\end{aligned} \tag{4.1}$$

Since F_{wall} and F_{friction} are both defined per meter circumference, $F_{\text{friction}} = F_{\text{axial}}/(2\pi r)$.

Finally, by using the definition for the Coulomb friction coefficient, as given in Equation 3.9, the coefficient of friction can be obtained through:

$$\mu = \frac{F_{\text{friction}}}{F_{\text{wall}}} = \frac{F_{\text{axial}}}{2\pi F_{\text{circ}}} \tag{4.2}$$

By adjusting the ratio between F_{axial} and F_{circ} the force ratio on the sealing disk can be varied. The ratio of these two forces equals μ. By increasing F_{axial} a range of μ from 0 to the value where the disk starts sliding can

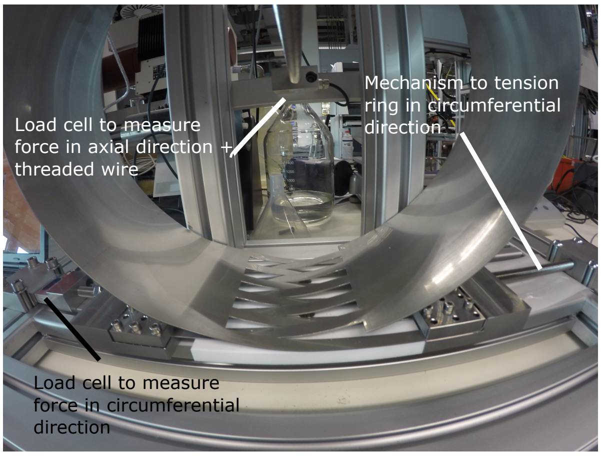

(a)

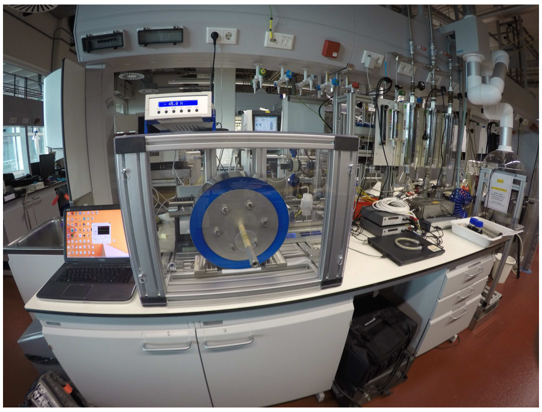

(b)

Figure 4.1: (a) A close-up of the experiment which shows: the metal ring, the axial load cell, and the circumferential load cell. (b) Overview of the experiments. The bolt which is turned to pull the disk through the metal ring is also shown. Poly-carbonate plates are placed for safety.

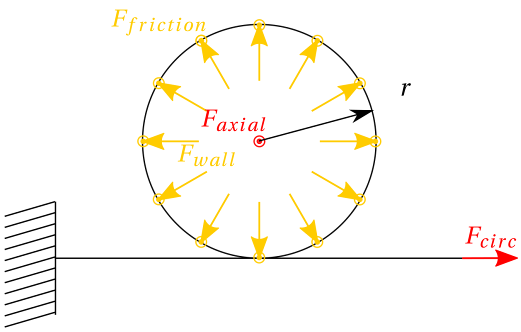

Figure 4.2: A schematic overview of the forces in the experiment.

be measured. Hypothetically the maximum μ equals the static coefficient of friction. By increasing the axial force a range of values for the coefficient of frictions can be obtained. How this range is measured is discussed in the following section.

4.2. MEASUREMENT PROCEDURE

All measurements were performed with two 24 bit GSV-2TSD-DI data acquisition devices connected to a 1 kN and 2 kN load cell (KD40S ME-systeme), for the circumferential and axial direction, respectively. The measurements were performed with 10 Hz and the settings of the device were recorded. The software used to record the data was GSV multi-channel. The sealing disk described in this chapter is a Baker Hughes 12" disk. Since the disk is new no wear was apparent and the dimension of the worn edge c is thus equal to zero. The disk has an outer radius of $r_s = 0.1615$ m , a clamping rate of 53.25% and a thickness (t) of 15 mm.

The disk is deformed to the specified oversize at the start of each measurement. At this point no axial force is applied, so $\mu = 0$. During the measurement the force in the axial direction is increased. When F_{axial} increases the circumferential force F_{circ} decreases. The increase in F_{axial} and decrease in F_{circ} is shown in Figure 4.3, where a typical time series is shown. During the entire measurement the disk is pulled through in steps. At each step three zones are distinguished: a rapid increase force (rise), a steady constant force (slip) and finally a slow decrease (rest).

In the rise zone the disk is still in static equilibrium. When the disk starts to move the slip zone is entered. During slipping a nearly constant noisy axial force is measured. It is assumed that during slipping the disk slips at some parts along the circumference and stays static at other parts. When the increase of F_{axial} is stopped the disk enters the rest mode which means that both forces are restored. It is thought that this is caused by micro slip and stress relaxation of the material. During microslip the rubber slips over the wall asperities of the metal ring. Stress relaxation occurs because the polymer chains of the rubber sealing disk find a lower energy state over time in the deformed position. When the polymer chains are in this new lower energy state the E-modulus of the material becomes lower.

The data points of the rise, slip and rest modes are selected by hand. This selection is shown in Figure 4.4.

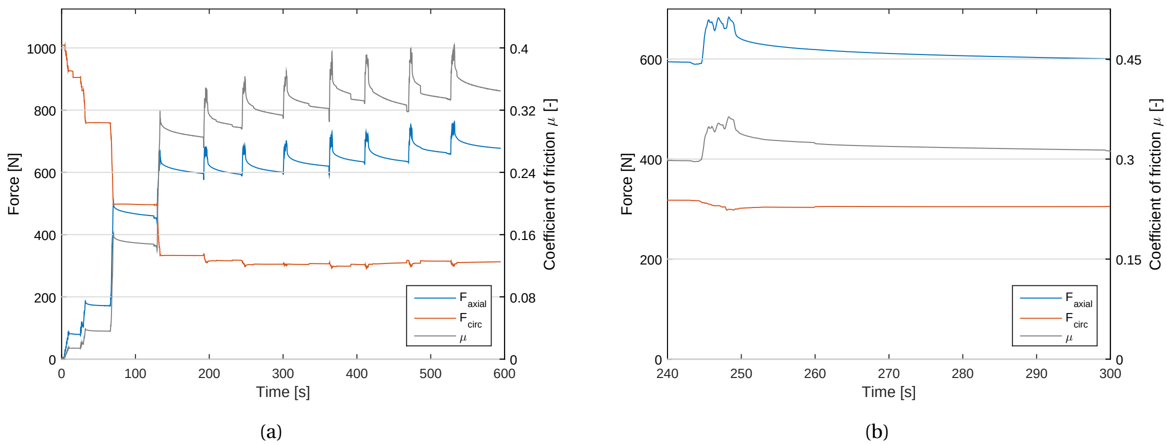

Figure 4.3: (a) Signal during a measurement with a 12" 75 Shore Baker Hughes sealing disk with spacer disks resulting in a clamping rate of 53.25% are used. The oversize is fixed at 2.8%. Afterwards μ is derived and plotted on a second y-axis. Note that the simulated coefficient of friction rises over the entire measurement period. (b) A close-up of one tensioning. See how 3 rotations of the bolt pulling the disk creates 3 oscillations in F_{axial}.

Each sealing disk is measured twice at each displacement. The radial displacement was kept constant per measurement set. Therefore, the experiments were performed for a radial displacement of, respectively 1.5, 3.0, 4.4, 5.9, 7.3, or 8.6 mm. For the described Baker Hughes disk these values correspond to an actual oversize of: 0.9%, 1.9%, 2.8%, 3.8%, 4.7%, 5.6%. The radial displacements are derived from the hypothetical radial displacement for 1 to 6 % oversize for 12 actual inches (0.3048 m).

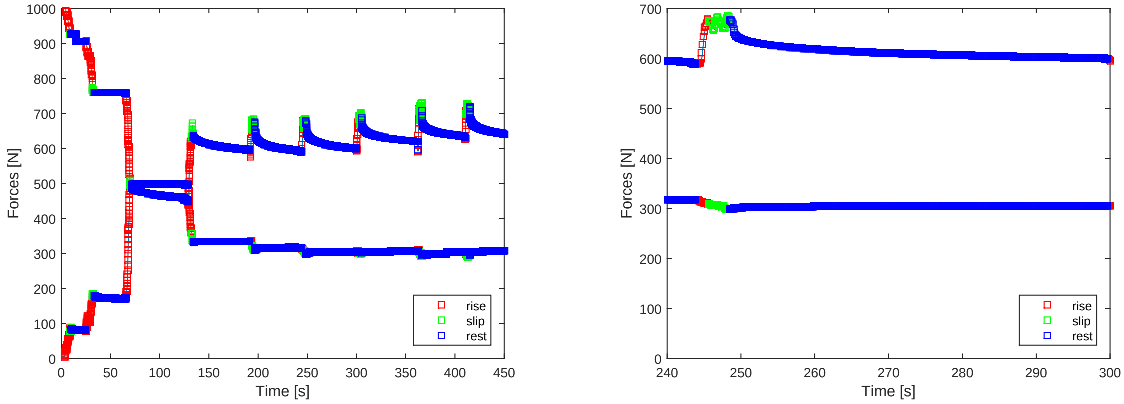

(a) (b)

Figure 4.4: Mask applied on the rise, slip and rest zone of the time series from Figure 4.3.

4.3. RESULTS

The coefficient of friction is calculated by Equation 4.2 and is plotted on a second y axis for a typical time series in Figure 4.3. How should these results be interpreted in relation to classic Coulomb friction which describes a static and dynamic coefficient of friction?

The static and dynamic coefficient of friction are denoted by μ_{static} and μ_{dynamic}. Typically, $\mu_{\text{static}} > \mu_{\text{dynamic}}$ and therefore μ_{static} is a threshold value for the ratio between the normal force and the tangential force after which motion is initiated.

In the rise zone the sealing disk is still in static equilibrium, and therefore $\mu < \mu_{\text{static}}$. During these measurements the signal is clear and repeatable. At some point during the increase of F_{axial} the disk starts slipping. This means $\mu > \mu_{\text{static}}$ at the points where the disk starts slipping. During the experiment it is seen that the μ at which slipping starts increases. After tensioning of the axial bolt the disk can rest. At this point it is thought that the rubber creeps around the wall asperities to relief a certain amount of force on the sides of the wall asperities.

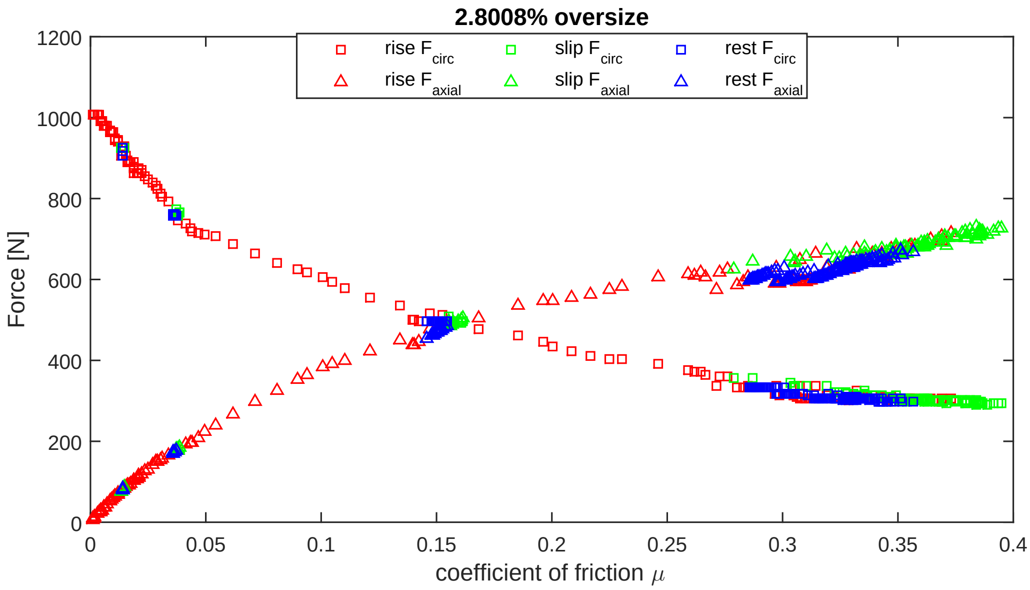

Figure 4.5: Measurement data for F_{circ} and F_{axial} plotted against the coefficient of friction μ. For clarity one in every 2 rise and slip data points are plotted and one in every 25 rest data points is plotted. Note that F_{circ} decreases when F_{axial} increases. The maximum μ is encountered in the slip region. This figure shows the necessary force to pull a pig sealing disk depending on the coefficient of friction.

For comparison all data points are plotted in Figure 4.5. In this figure one in every two data points is plotted for the rise and slip zone. For the rest zone one in every 25 data points is plotted. To remove the noise from oscillations only the rise data points are used. All rise data points are plotted in Figure 4.6.

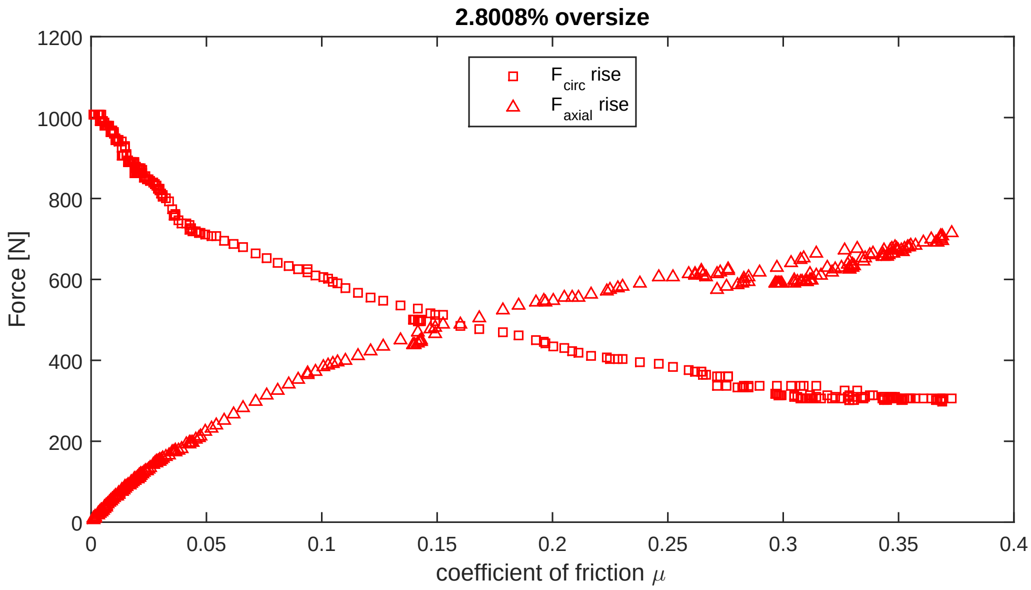

Figure 4.6: Rise measurement data for F_{circ} and F_{axial} plotted against the coefficient of friction μ. All datapoints are plotted. Some noise still occurs at the higher coefficient of friction.

In Appendix F the measurements for a range of oversizes are shown. To demonstrate repeatability each measurement session is performed in duplex. The overlap in measured values shows that the measurements are repeatable. For higher oversizes no significant different μ's were encountered.

In Figure 4.7 the experiment is compared to the finite element and analytical results. To compare the experiment results with the model results the forces for a constant μ need to be obtained. To obtain data points for $\mu = 0.3$ the average of all values between $\mu = 0.29..0.31$ is taken. All other geometric dimensions are according to the dimensions of the experiment. The finite element model uses the non-linear material model in combination with data from axial strain tests. The analytical model described in Chapter 3 assumes: a linear E-modulus of 12.25 MPa, a Poisson's ratio of 0.45, and a correction factor of 1.45. The differences between the model and experiment are probably explained by internal friction of the experiment. At the point where both ends of the metal ring meet a certain friction force is needed to fix the disk in the correct oversize. When the oversize increases the internal friction will increase as well.

Other sources of errors which are not taken into account are: temperature influences, and skewness of the sealing disk during a measurement. These nuisances are seen in the noise of the two different measurements.

The boundary conditions of the finite element model cause some error. The disk is currently free to move in the radial direction, which is partly true in the experiment. Secondly F_{wall} and F_{friction} are applied as a concentrated force. The local deformation therefore will show some error. In the following chapter this local deformation will be further discussed.

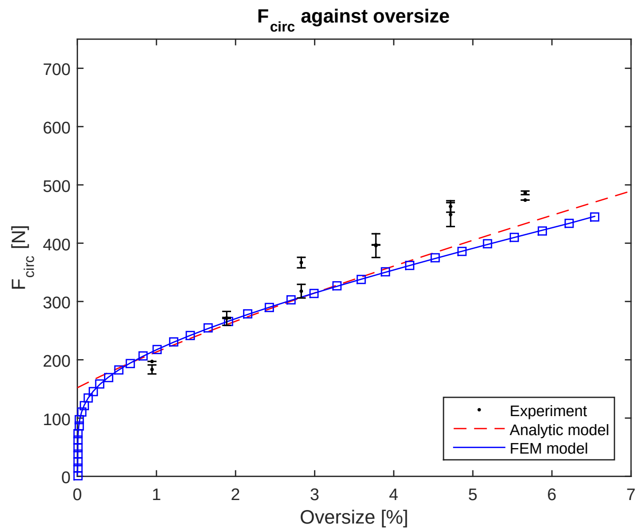

Figure 4.7: The measured force F_{circ} is compared to results from a non-linear finite element model and the analytical model. The analytical model results are for the geometry as described. Used material properties are: E = 12.25 MPa, ν = 0.45 and a correction factor C = 1.45.

4.4. ADDITIONAL EXPERIMENTS

To further validate the analytical model multiple different sealing disks are compared. First the notable differences between both vendors are discussed and a disk similar to the Baker Hughes disk is tested. To see if the analytical model is correct, a thinner disk (13 mm) of the same material and a softer 65 Shore disk are also tested. Finally, a conclusion is drawn on the applicability of the analytical model for general sealing disks.

4.4.1. SEALING DISKS FROM DIFFERENT VENDORS

In Figure 4.8 a typical sealing disk from Rosen is shown. The relevant dimensions are given in Table 4.1. First it must be noted that a 12 inch disk from this vendor has a diameter of 0.308 m. This is significantly less than the Baker Hughes disk (0.323 m diameter), but larger than 12 inch (0.3048 m). The measurement procedure for the experiments described in this chapter is equal to the one explained in Chapter 4. However, the comparison is done for a lower coefficient of friction (μ = 0.25). The spacer disk is the same as the one used in the previous chapter (0.172 m diameter). This gives a higher clamping rate of 55.8% for the Rosen disk. As can be seen in Figure 4.8, additional holes needed to be drilled to mount the spacer disk. Since these holes are in the area where the rubber is clamped between the spacer disks, it is assumed that the influence of these holes can be neglected.

Since no material measurements are performed for these disks the E-modulus is unknown. In the previous chapter it was already shown that the analytical model, with a linear correction factor, gives similar results as the non-linear finite element model. In this case the material behaviour of the disks is unknown and therefore no additional finite element simulations are performed. Since the E-modulus is unknown its value is estimated

Figure 4.8: A sealing disk from Rosen. Note that the dimensions of the nut holes are different from those in the disk of Baker Hughes. To use the available spacer disk additional nut holes were drilled.

Table 4.1: Properties of additionally tested sealing disks. The matched E-modulus of the Baker Hughes disk is taken as: Cor ∗ E = 1.45 * 12.25 = 17.76 MPa .

Parameter	Standard disk	65 Shore disk	13 mm disk	62% Clamping	Baker Hughes disk
Vendor	Rosen	Rosen	Rosen	Baker Hughes	Baker Hughes
Diameter	0.308 m	0.308 m	0.308 m	0.323	0.323 m
Inner diameter	0.100 m	0.100 m	0.100 m	0.117	0.117 m
Thickness	15 mm	15mm	13 mm	15	15 mm
Material	75 Shore	65 Shore	75 Shore	75 Shore	75 Shore
E_{fit}	12.5 MPa	7 MPa	12.5 MPa	17.76 MPa	17.76 MPa
Spacer disk	172 mm	172 mm	172 mm	201.2 mm	172 mm

through making a fit to the experiments. One can see that the model scales linearly with the E-modulus, and therefore the linear correction factor and E-modulus can be combined in a corrected E-modulus E_{fit}. The used disks are new so no chamfer was apparent.

The measurement data as a function of the coefficient of friction are shown in Appendix F. All measurements are performed in duplex to validate repeatability. Again only the data points during the rise (during tensioning) are selected.

4.4.2. COMPARISON BAKER HUGHES AND ROSEN SEALING DISKS

First the disk from Rosen, with the same specifications, is used to make a comparison with the disk from Baker Hughes. Note that since the same spacer disk is used the clamping rate of the Rosen disk is a bit higher. Therefore, it is expected that the Rosen disk is stiffer and thus F_{circ} is higher. The results are shown in Figure 4.9. The Baker Hughes disk is significantly stiffer than the Rosen disk. Both the Baker Hughes disk and the Rosen disk have the same thickness (15 mm) and same hardness (75 shore). The fitted E-modulus (E_{fit}) is 12.5 MPa with an assumed Poisson's ratio of 0.45. Datapoints near 2% oversize were unusable because of a measurement error.

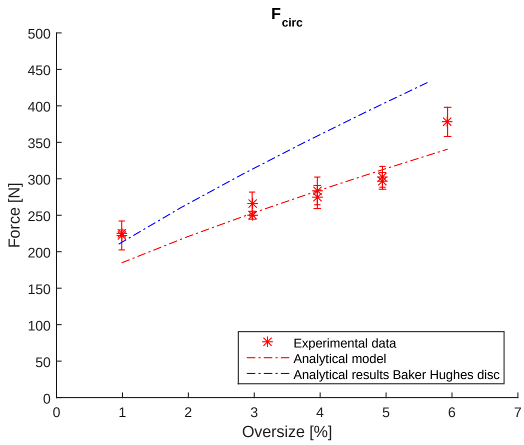

Figure 4.9: Measurement results and analytical results of the Rosen standard disk compared to the Baker Hughes disk that was shown in Figure 4.7. The fitted E-modulus (E_{fit}) was taken as 12.5 MPa with an assumed Poisson's ratio of 0.45. The results are for a coefficient of friction of μ = 0.25.

It can be concluded that the Rosen disk is much more flexible than the Baker Hughes disk. When the maximum coefficient of friction of the material was evaluated no conclusions could be drawn when compared to the Baker Hughes disk. Overall the conclusion can be drawn that the Shore hardness is a bad predictor of the quantitative material behaviour of a pig sealing disk.

4.4.3. 13 MM DISK

It is expected that the 13 mm disk behaviour can be described with the same fitted E-modulus as the 15 mm Rosen disk. The measurement results are shown in Figure 4.10.

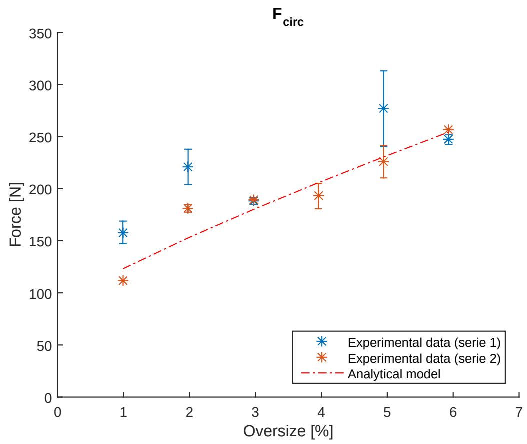

Figure 4.10: Measurement results and analytical results of the Rosen 13 mm disk. The fitted E-modulus (E_{fit}) was taken as 12.5 MPa with an assumed Poisson's ratio of 0.45. The results are for a coefficient of friction of $\mu = 0.25$.

The used values for E_{fit} and ν are equal to the ones used for the 15 mm disk. This means that for a similar material the analytical model is valid for various thicknesses.

4.4.4. 65 Shore disk

In this section a softer material is tested (65 Shore). It is interesting to see whether this influences the maximum of the measured μ. When inspecting the measurement data in Figure F.10 this seems to be the case. However, the maximum measured coefficient of friction becomes lower for larger oversizes. The measurement results as a function of the oversize are given in Figure 4.11. It can be seen that the measurements are close to each other in comparison to the previous measurements.

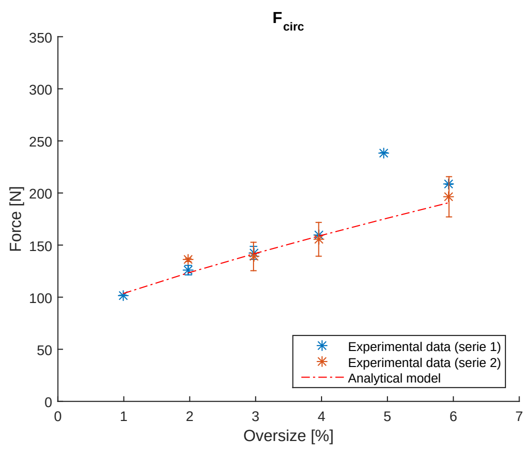

Figure 4.11: Measurement results and analytical results of the Rosen 65 Shore disk. The fitted E-modulus (E_{fit}) was taken as 7 MPa with an assumed Poisson's ratio of 0.45. The results are for a coefficient of friction of $\mu = 0.25$.

With a fitted E-modulus of 7 MPa and a Poisson's ratio of 0.45 the analytical model can accurately describe F_{circ}.

4.4.5. 62.28% Clamping rate

In this section a higher clamping rate is tested. The Baker Hughes disk with the material properties fitted to the non-linear material model are used. It is important to see if this different geometry corresponds to the same material properties. The results are shown in Figure 4.12

With a fitted E-modulus of 17.76 MPa and a Poisson's ratio of 0.45 the analytical model can accurately describe F_{circ}. Note that this implies that the analytical model is able to describe an increase in clamping rate accurately. At higher oversize the forces become too high and the measurement results became inaccurate.

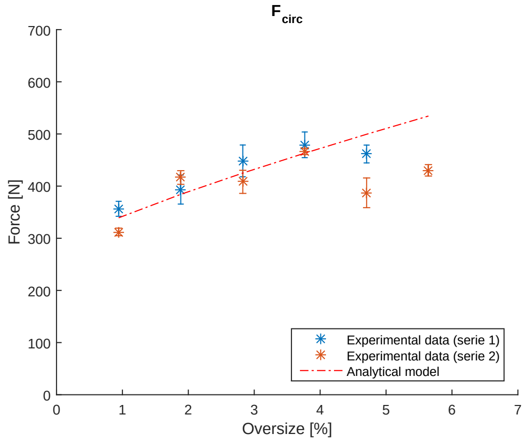

Figure 4.12: Measurement results and analytical results of the Baker Hughes 62.28% clamping rate disk. The fitted E-modulus (E_{fit}) was taken as 17.76 MPa with an assumed Poisson's ratio of 0.45. The results are for a coefficient of friction of $\mu = 0.25$.

4.5. CONCLUSION

In this chapter an overview has been given of data from literature to determine the friction of a pig sealing disk. It was identified that no measurement data were available for μ and F_{friction} in a single measurement. The current data from literature are therefore dependent on external friction tests which have a large uncertainty (20%). In this thesis an experiment has been designed to measure both F_{friction} and μ at the same time. Measurements have been performed for a commercial pig sealing disk and are shown to be in agreement with the FEM and analytic model.

Next, sealing disks from different vendors were compared. For a similar specified sealing disk both the dimensions and the materials are different. It is shown that for a conservative comparison similar specified disks can differ by as much as 45%. In this case the increase of the clamping rate (because of the smaller diameter of the Rosen disk) is neglected.

Also a different geometry was tested. It was shown that the analytical model can accurately describe the material behaviour of different geometries. Finally, a softer disk was measured. The difference in wall force was roughly 50% with the 75 Shore disk.

The next question is: can the coefficient of friction be predicted for actual pigging operations? This will be the subject of the following chapters.

5
Lubrication model

In this chapter a model is described to predict the coefficient of friction for a moving pig. This secondary model serves to predict μ and can be coupled with the model used to describe the wall force. With the use of this model an attempt is made to predict at which circumstances lubrication occurs. When lubrication occurs the coefficient of friction can drop an order of magnitude. Due to the lubrication the velocity will increase which will in turn improve the lubrication even further. However, small disturbances can suddenly destroy the lubrication effect. In this case the coefficient of friction rapidly increases creating large disturbances on the pig, pipe and fluids. First the governing equations are described in Section 5.1. To solve these non-linear equations a numerical scheme is proposed in Section 5.2. The results of this approach are discussed in Section 5.3. Finally, a conclusion is presented in Section 5.4.

5.1. Modelling equations

It will be assumed that the material near the wall can be described by a planar coordinate system. This assumption is valid because the equations for an axisymmetry configuration convergence to the equations for a planar configuration when the coordinate in the radial direction increases.

> Assumption: The contact area can be described by a planar coordinate system. ($\frac{h}{r} << 1$)

Here h is the fluid film height (which will be further defined) and r the pipe radius. The lubrication model is split up into three parts:

- Contact pressure
- Asperity pressure
- Fluid pressure

An attempt to combine these three pressures was made by O'Donoghue [6]. The used contact models, asperity model and fluid pressure are fundamental in describing elastohydrodynamic lubrication (EHL) problems [31][6][30].

First the contact pressure is discussed. It is assumed that the local deformation is small enough to treat it separately from the global deformation [25].

> Assumption: The local contact deformation is small enough to not influence the global deformation (Saint-Venant's principle).

The contact pressure is modelled with the Winkler spring theory or elastic foundation theory. The local deformation is modelled with linear springs with a certain stiffness constant K. The springs are assumed to be independent, and thus any interaction with the deformation around the spring is neglected [31].

Assumptions: The local deformation can be described with the foundation model. The foundation model assumes that linear elastic material can be described by closely spaced independent linear springs. The deformation of the foundation due to an applied load is confined to the loaded region only.

A brief remark should be made at this assumption about wear. The simplest model to describe sliding wear is the Archard equation. This equation describes how the removed debris is proportional to the work done by friction forces [45]. Therefore, at steady state, a uniform contact pressure distribution may be assumed.

The Winkler foundation theory describes the pressure at any deformation as:

$$P_{\text{contact}} = K * (\delta_o - h_o(x)) \tag{5.1}$$

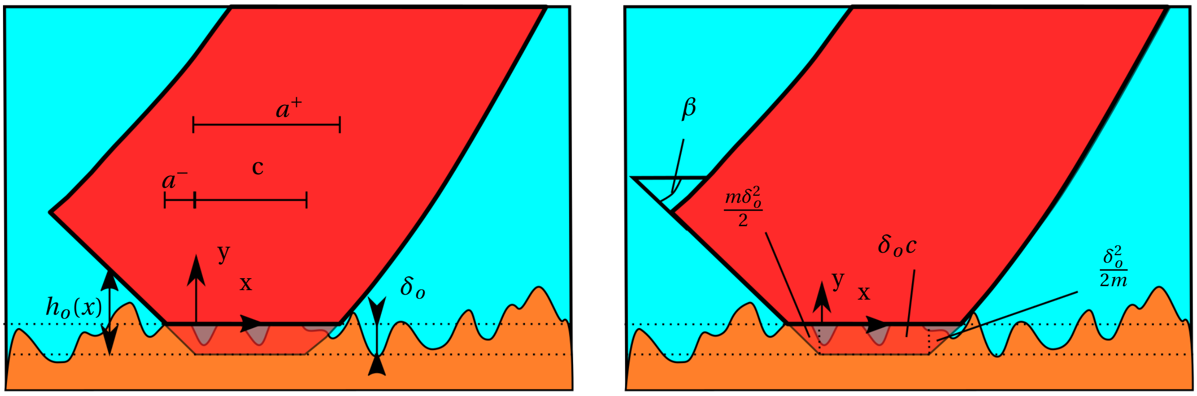

Figure 5.1: The parameter δ_o equals the initial indentation to carry the load F_{wall}. The geometry of the disk is described by a function h_o. The chamfer length equals c. The amount of deformed material can be described by three terms: $m\delta_o^2/2$, $\delta_o * c$, and $\delta_o^2/(2*m)$

Here K is a constant, δ_o is the original indentation and h_o is the original geometry as a function of x. In Figure D.1 an illustration of these parameters is given. The original geometry is the geometry before contact and equals zero at the x position where the maximum deformation occurs. An initial load F_{wall} will create a deformation along the x-axis equal to the original indentation minus the original geometry between the footprint length. With the geometry from the kinematic model described in Chapter 3 the original geometry h_o can be described by three zones. The bottom of the disk has a contact foot length a^-. The chamfer, which is the worn edge at the end of the sealing disk, runs parallel from $x = 0...c$. Finally, the positive foot print runs from $x = c...a^+$. The inclination at these three zones is denoted by m. The inclination m is found by:

$$m = \tan(\pi/2 - \beta) \tag{5.2}$$

The original height at $x = a^-...0$ is described by:

$$h_o(x) = -m * x \tag{5.3}$$

The original height at $x = 0...c$ is described by:

$$h_o(x) = 0 \tag{5.4}$$

The original height at $x = c...a^+$ equals:

$$h_o(x) = (x - c)/m \tag{5.5}$$

The challenge in the Winkler foundation theory is to find an accurate value of K. As an initial estimate K is matched to the analytical solution of Hertz for the contact problem between an elastic half space and a cylinder [31]. A full derivation of this is given in appendix D.1. When the linear coefficient is matched the following relationship is found:

$$P_{to} = \frac{1.013E}{a(1-\nu^2)}(\delta_o - h_o(x)) \tag{5.6}$$

Note that by using this K the pressure becomes a function of the footprint, the height profile and the initial indentation. To reduce the number of unknowns, the relation between the initial indentation (δ_o) and contact length (a) is used. This is shown for example by O'Donoghue [6]. From the original height profile three expressions are found.

The negative footprint equals:

$$a^- = \frac{\delta_o}{m} \tag{5.7}$$

The positive footprint equals:

$$a^+ = c + \delta_o m \tag{5.8}$$

The average footprint equals:

$$a = \frac{\delta_o m^2 + cm + \delta_o}{2m} \tag{5.9}$$

To eliminate one unknown an additional equation is found by integrating the contact pressure over the contact area. This is described as:

$$F_{\text{wall}} = \int_{a^-}^{a^+} P_t dx = \frac{1.013E}{(1-\nu^2)a}\left(\frac{m\delta_o^2}{2} + \delta_o c + \frac{\delta_o^2}{2m}\right) \tag{5.10}$$

By combining Equations 5.9 and 5.10 the initial indentation depth can be found as:

$$\begin{aligned} \delta_o &= \frac{\mathrm{C1} - 2\,c\,m + \mathrm{C1}\,m^2 - \sqrt{\mathrm{C1}^2\,m^4 + 2\,\mathrm{C1}^2\,m^2 + \mathrm{C1}^2 + 4\,c^2\,m^2}}{2\left(m^2+1\right)} \\ \mathrm{C1} &= \frac{F_{\text{wall}}(1-\nu^2)}{1.013E} \end{aligned} \tag{5.11}$$

Finally, the original geometry (h_0), the original indentation (δ_o) and the contact length (a) are found. To find these the input parameters c, β, ν, E and F_{wall} are used.

Since the geometry is static, the force (or pressure) applied by the sealing disk must be matched with an external pressure. In the lubrication model the pressure consists of two contributions: the asperity pressure (P_a) and the fluid film pressure (P_f). When a fluid film forms, or when the height of the wall asperities increases, the sealing disk will be deformed. This additional deformation is called h. The deformation of the sealing disk contact can therefore be written as:

$$P_t = \frac{1.013E}{a(1-\nu^2)}(\delta_o - h_o(x) + h(x)) \tag{5.12}$$

In this equation $h(x)$ is the additional deformation caused by the fluid film asperities. Therefore, this value denotes the fluid film height. The variable $h(x)$ is shown in Figure 5.2.

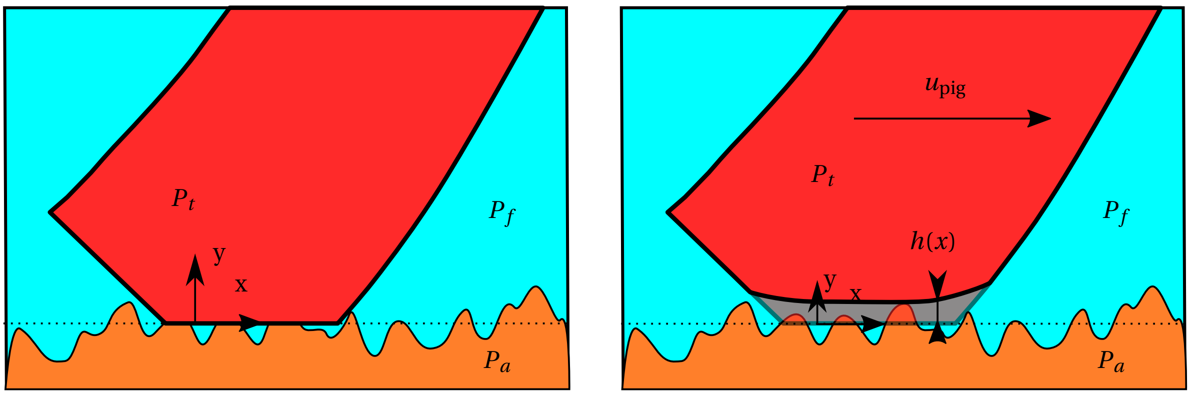

Figure 5.2: The deformation of the sealing disk placed on a reference height is determined by the average height of the wall asperities. Here a balance has to be found between the asperity pressure P_a, the fluid pressure P_f and the contact pressure P_t.

The Greenwood-Wiliamson asperity model takes the elastic deformation of the wall asperities into account [35] [33]. To do this the model assumes an exponential distribution for the height profile in which the peaks of the wall asperities are deformed. The deformation of the peaks is described with the Hertzian equation for contacting spheres. To use this equation the values for the curvature of the spheres (R_a) and for the density of the spheres (N_a) must be known. These two values, together with the wall roughness (σ_a), are captured by the following dimensionless number:

$$K_s = R_a^{1/2} N_a \sigma_a^{3/2} \tag{5.13}$$

The necessary assumptions to derive the Greenwood-Wiliamson model are:

- The asperities have a spherical shape with a constant radius of curvature.
- The deformation of the asperities can be described with the Hertzian contact equations.
- The heights of the asperities have an exponential or normal Gaussian distributions.
- The deformation of each asperity is independent of its neighbours.

Note that these assumptions are very approximate, and more accurate asperity models do exist. However, the additional value of these models is limited when little is known about the actual wall roughness.

In Appendix D.3 a brief derivation of the Greenwood-Wiliamson model is given. The final expression for the pressure carried by the asperities contact as a function of the height h is:

$$P_a = \frac{\sqrt{2} K_s E}{2(1-\nu^2)} e^{-h/\sigma_a} \tag{5.14}$$

The lubrication effect of the liquid in a thin film can be described with the lubrication equation which for a planar configuration reads:

$$\frac{d}{dx}\left(\frac{-h^3}{12\eta}\frac{dP_f}{dx}\right) = \frac{u_{\text{pig}}}{2}\frac{dh}{dx} \tag{5.15}$$

Here P_f is the fluid pressure, η is the viscosity and u_{pig} is the pig velocity [30].

For a derivation of Equation 5.15 from the Reynolds equation see appendix E. The assumptions necessary to derive the Reynolds equation are:

- Because of the thin film geometry, the velocity in the x direction is dominant compared to the other directions.
- The viscous terms in the fluid are dominant (Stokes flow).
- The geometry is quasi static (dh/dt can be neglected).
- Flow disturbances by asperities can be neglected.

The assumptions of steady state can easily be removed by adding the transient terms [30]. The assumption of flow disturbances could easily be removed by adding additional empirical terms as described by Patir and Cheng [36]. However, for its practical application the choice was made to keep the model steady state and to neglect both the flow disturbances and the instationary flow effects.

The assumption of steady state implies that the pressure balance should be zero in every point along the contact area. This results into Equation 5.16, given as:

$$P_t(h) - P_a(h) - P_f(h) = 0 \tag{5.16}$$

Finally, by combining the contact pressure (Equation 5.12), the asperity pressure (Equation 5.14) and the fluid film pressure (Equation 5.15) in the pressure balance (Equation 5.16) a new $h(x)$ can be found. The input parameters are: K_s, E,ν, σ, u_{pig}, δ_o and a. Since Equation 5.15 is a differential equation, the pressure boundary conditions also need to be specified. The pressure difference over the gap is formulates as ΔP.

With the fluid film height the required friction force can be calculated as:

$$F_{\text{friction}} = F_a - F_f \tag{5.17}$$

Where F_a is the asperity friction in N/m, and F_f is the fluid friction in N/m. It must be noted that the fluid friction is much smaller than the asperity friction. The fluid friction is in the opposite direction of the asperity friction because the fluid in the fluid film moves faster than the pig due to the pressure difference over the pig.

The fluid friction is:

$$F_f = \int \left(\frac{dP_f}{dx} \frac{h}{2} - \frac{\eta u_{\text{pig}}}{h} \right) dx \tag{5.18}$$

The asperity friction is:

$$F_a = \mu_{\text{dry}} \int P_a \, dx \tag{5.19}$$

in which μ_{dry} is the coefficient of friction for dry contact. Finally, a new coefficient of friction can be calculated by:

$$\mu = \frac{F_{\text{friction}}}{F_{\text{wall}}} \tag{5.20}$$

5.2. NUMERICAL IMPLEMENTATION

The problem that needs to be solved is: $P_f(h_{i+1}, h_i, h_{i-1}) + P_a(h_i) - P_t(h_i) = 0$. The difficulty is that P_f is dependent on the fluid film height on both sides. Therefore, it is not possible to evaluate the pressure at each point separately. When Equation 5.15 is re-written to solve for P_f (as has been done in Equation E.11) a parameter h^3 appears in the denominator. Therefore, P_f goes to ∞ for h=0. Any numerical scheme must prevent that h becomes less than or equal to 0.

In this case the height h is varied until:

$$P_f(h_{i+1}, h_i, h_{i-1}) + P_a(h_i) - P_t(h_i) < \text{convergence criterion} \tag{5.21}$$

The convergence criterion in this case stands for an unbalance in pressure. To find h, h_i is iterated by the following equation:

$$h_i^{n+1} = h_i^n + P_f^n(h_{i+1}, h_i, h_{i-1}) + P_a^n(h_i) - P_t^n(h_i) \frac{(1-\nu^2)}{1.013\text{RELAX} * E} \tag{5.22}$$

To prevent that h_i becomes less than zero the RELAX factor is increased. This is repeated until a value for h_i is found at which the unbalance in pressure is less than the convergence criterion.

For the used discretization first order convergence is expected. To validate this, results for a very fine mesh are compared to those for coarser meshes. The input values given in Table 5.1 are used. The relative error is calculated by:

$$\text{relative error} = \frac{\max(h(x)) - \max(h(x))_{\text{very fine mesh}}}{\max(h(x))_{\text{very fine mesh}}} \tag{5.23}$$

The very fine mesh solution was obtained with 510 nodes. Figure 6.3 shows that the solution indeed converges with a first order error.

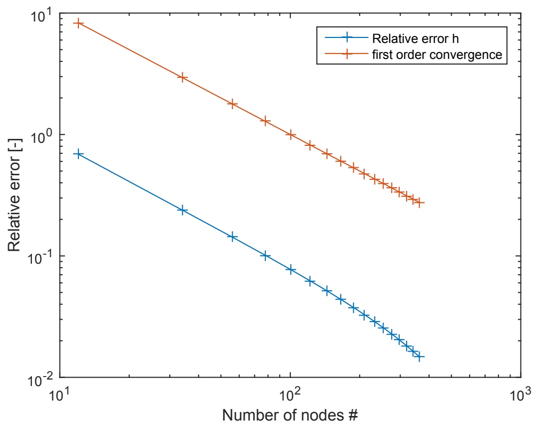

Figure 5.3: The relative error against the number of nodes. As one can see the model converges with roughly first order.

5.3. RESULTS

In this section a typical result from the previous model is shown. First the input parameters are discussed and an initial guess of the mesh is shown. In Table 5.1 the input parameters of the lubrication model are given.

Table 5.1: The input parameters of the described lubrication model.

Parameter	Value
Force on wall (F_{wall})	410 N/m
Speed (u_{pig})	1 m/s
Viscosity (η)	1e-3 Pa.s
Dry coefficiient of friction (μ_{dry})	0.9
Modulus of elasticity (E)	12.25 MPa
Poisson's ratio (ν)	0.45
beta for 1% oversize (β)	0.6929
Chamfer (c)	0.005
Dimensionless friction number (K_s)	0.0115
Std. deviation wall roughness (σ)	6.7e-6 m
Pressure drop over pig (ΔP)	0 Pa

The initial mesh is shown in Figure 5.4. The function to describe the film height equals $h_o(x) + \text{guess} = h$, where the guess is typically in the range of $0.5\sigma_a$ - $3\sigma_a$. This is the typical range for EHL lubrication. The convergence criterion is 1 Pa. This criterion is considerably more difficult to obtain at the locations near the edges of the chamfer. Therefore, the mesh size is refined at these locations. The convergence becomes increasingly difficult for small film heights. No extensive study has been performed on this. However it is likely that the instability increases when the stiffness of the lubrication equation increases. Again this is because h becomes closer to 0. For full fluid film lubrication, the convergence takes less than 5 minutes on an average laptop. In the case of bad lubrication convergence can take up to 1 hour.

The solution of the diverging edge (near a^-) is shown in Figure 5.5(a). Note that there is a small under pressure at this location. The lubrication pressure here becomes lower and the material is sucked to the pipeline wall. Here the asperity pressure also increases. The solution for the converging edge (near a^+) is shown in Figure 5.5(b). At the converging edge the material is deformed. Between the previous two zones, the fluid film pressure and the film height are nearly constant.

The pressures are shown in Figure 5.6. As one can see the diverging side has a small under pressure. However over the entire contact area the pressure is nearly constant. Note that in this simulation ΔP was chosen equal to 0.

By solving Equation 5.20 the coefficient of friction is found. The Stribeck curve predicts a straight line for the coefficient of friction against the lubrication parameter when plotted on a log-log scale [30]. The lubrication parameter is a dimensionless number consisting of the main parameters that influence the

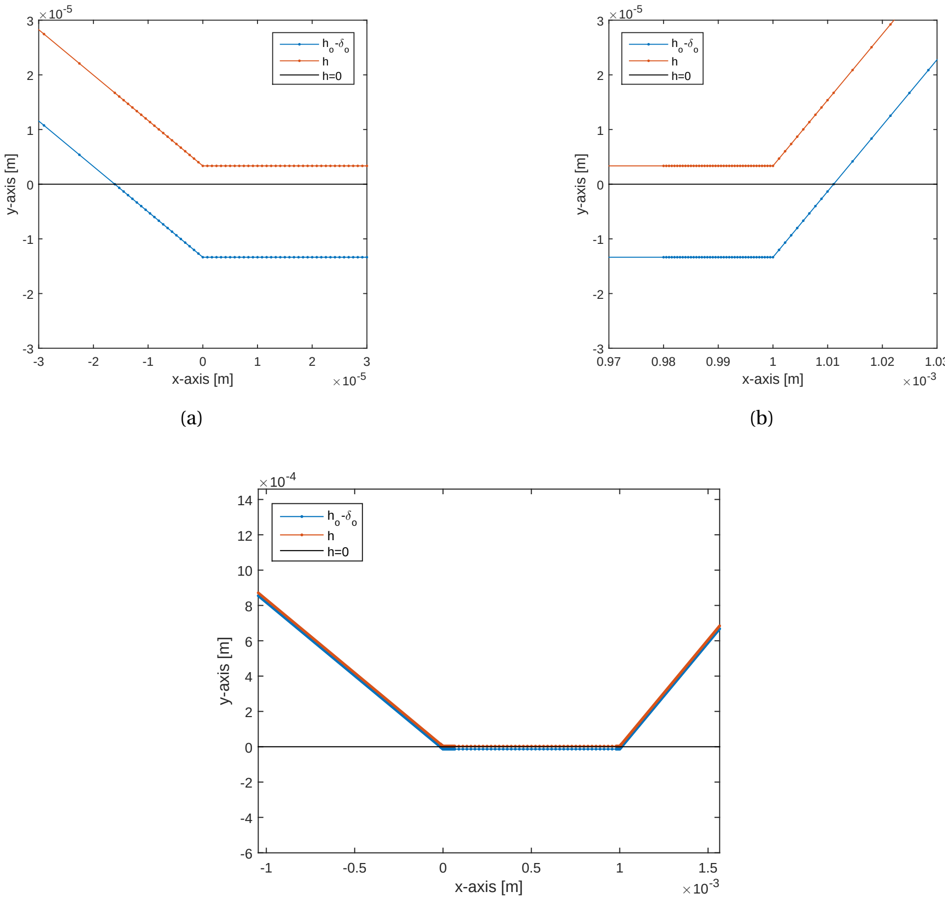

(a) (b) (c)

Figure 5.4: An initial guess of the solution is made. In this case the original solution is equal to $h_o + 1\sigma_a$.

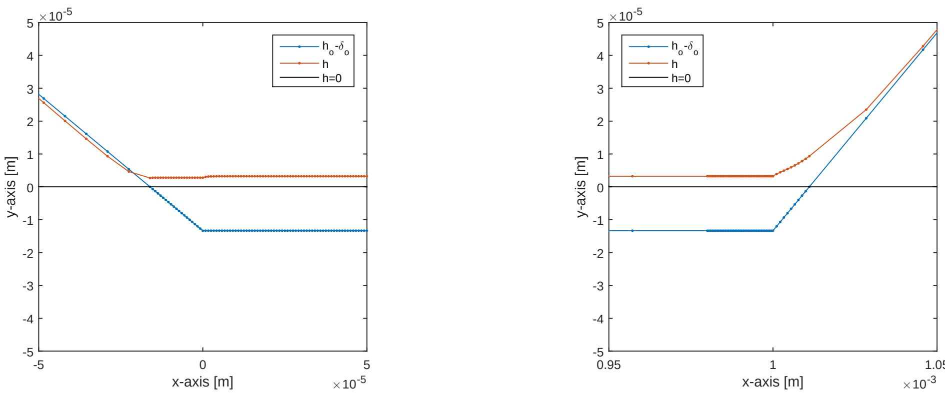

(a) (b)

Figure 5.5: The resulting film height for the input parameters given in Table 5.1. Note that at the converging edge the pressure increases and the film height becomes larger. At the back end the pressure becomes lower and the film height decreases.

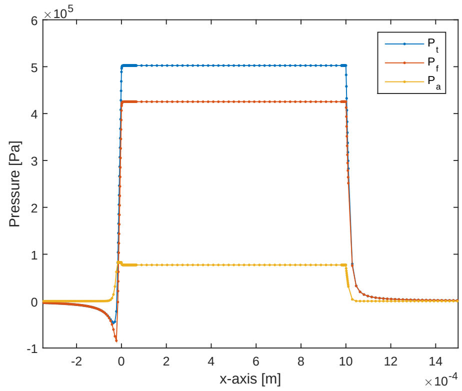

Figure 5.6: The pressure P_f, P_t and P_a as a function of x. The input parameters are given in table 5.1.

lubrication behaviour. These parameters are: viscosity (η), velocity (u_{pig}), and the load (F_{wall}). A plot of the coefficient of friction as a function of the lubrication parameter is shown in Figure 5.7.

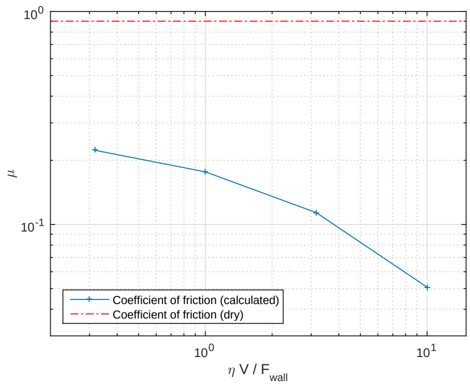

Figure 5.7: The stribeck curve which is calculated by the model described in this chapter.

The maximum film height for 0.31 m/s, 1 m/s, 3.1 m/s, and 10 m/s are 0.24 σ_a, 0.48 σ_a, 0.93 σ_a, and 1.8 σ_a. This means that the coefficient of friction initially is calculated at the left side of the Stribeck curve where lubrication is poor. The curvature near the poor lubrication is in agreement with the Stribeck curve.

For large fluid film heights it can be seen from Equation 5.12 that the contact pressure also increases. The contact pressure is delivered by the bending of the sealing disk and therefore this suggests that F_{wall} also increases. This influence can be calculated by:

$$\text{Conservation of force} = \frac{F_{\text{wall}}}{\int P_t dx} \tag{5.24}$$

The conservation of force for the velocities 0.31 m/s, 1 m/s, 3.31 m/s, and 10 m/s are 0.88, 0.7984, 0.6756, and 0.5263. A conservation of force of 0.5 means that the fluid pressure needs to overcome a force twice that of F_{wall}. The reason for this is that the Winkler springs assume local indentation. For higher deformations the foot length a should be recalculated. An attempt to combine this small length scale deformation with the overall deformation is done by using the boundary element method. This subject will be discussed in the following chapter.

5.4. CONCLUSION

In this chapter a model was discussed to describe the lubrication behaviour of a pig. For the analytical relations for the contact pressure, the asperity pressure and the fluid pressure were discussed. These three equations describe the deformation of the pig at local contact. By combining these three equations in a numerical model the pressure at contact can be calculated. It is shown that this model is in agreement with the Stribeck curve.

For higher fluid film heights the model significantly over predicts the contact pressure. This is because the large deformation is not taken into account. To couple this local lubrication effect with the large deformation effect a boundary element approach is suggested in the following chapters.

6

Boundary element model

In this chapter a brief introduction into boundary elements is given. First the boundary integral equations lying underneath the boundary element method are discussed. The boundary integral equations are discretized to enable using them in the boundary element method to solve the linear elasticity problem. By discretization a general purpose method is obtained to solve different geometries. The proposed discretization is checked for convergence and its accuracy is validated for a case with a beam.

6.1. Introduction

The boundary element method (BEM) is, just like the finite element method, a method to solve partial differential equations. The boundary element method however can only be used to solve linear partial differential equations. Therefore, the application is more limited than for example the finite element method. The finite element method divides a domain into multiple finite elements. A 3D problem is solved by building a model out of 3D elements (for example cubes or tetrahedrons). The boundary element method differs from the finite element method by dividing the problem into boundary elements which are one dimension less. In this way a 3D problem can be described by dividing it into 2D (for example square or triangular) boundary elements. Similar, a 2D problem can be described by 1D elements (lines) and a 1D problem by 0D elements (points). This reduction by one dimension is very advantageous when describing certain problems. An example of the difference between a finite element approach and a boundary element approach is shown in Figure 6.1.

First the reduction of complexity can be advantageous when the meshing of a certain problem becomes difficult. For contact problems typically a very fine mesh is needed near the contact area and in the domain near the contact area. The mesh size can thereby become so small that the computational effort to solve the problem becomes very high. When this kind of problem is solved with boundary elements it is simple to make the mesh very fine near the contact area and coarse in the rest of the domain. A second advantage of the use of boundary elements is that when the solution for the boundary is known the solution can be found for any point in the interior of the domain. This is helpful while evaluating high stress concentrations.

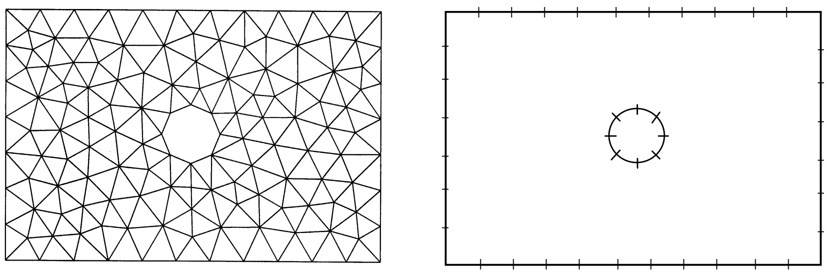

(FEM Discretization: 228 Elements) (BEM Discretization: 44 Elements)

Figure 6.1: A comparison between a finite element mesh and a boundary element mesh. Note that far less elements are required in the boundary element method [11].

A third advantage of this method is that it can easily solve infinite domains. An example of such an application can for example be found in fluid mechanics. To solve the flow field around a certain object only the shape of the object needs to be modelled. When the solution for the 1D boundary elements defining a 2D aerofoil are known the entire potential flow field can be solved.

In previous examples it was shown that the nature of the boundary elements makes them very suitable to define and solve certain problems. Because of the nature of these elements, the number of elements necessary to describe a problem can be significantly reduced. This results in a smaller set of equations and thus into smaller matrices which need to be solved. This makes the boundary element method computational more efficient. However unlike the sparse matrices obtained with the finite element method, the matrices of the boundary element method are full.

To understand the boundary element method first the boundary integral method is discussed. The boundary integral method is a method for solving partial differential equations by reducing them to boundary problems. Many textbooks on the subject of boundary integral equations and the boundary element method have been written. Therefore, the explanation in this thesis is very compact and serves to give a simple understanding of the working principles. For more information about boundary integrals or the boundary element method the reader is referred to e.g. Beer [46] and Gaul [47].

6.2. THEORY

The boundary integral method describes a way to solve partial differential equations such as those related to Stokes flow and linear elasticity.

6.2.1. GOVERNING EQUATIONS FOR STOKES FLOW

The governing equations for Stokes flow are:

$$-\nabla p + \mu \nabla^2 \mathbf{u}(\mathbf{x_0}) = 0 \tag{6.1}$$

$$\nabla \cdot \mathbf{u}(\mathbf{x_0}) = 0 \tag{6.2}$$

Here $\mathbf{u}(\mathbf{x_0})$ is the velocity in the fluid domain at location $\mathbf{x_0}$, see Figure 6.2a. Furthermore, p is the pressure and μ is the dynamic viscosity.

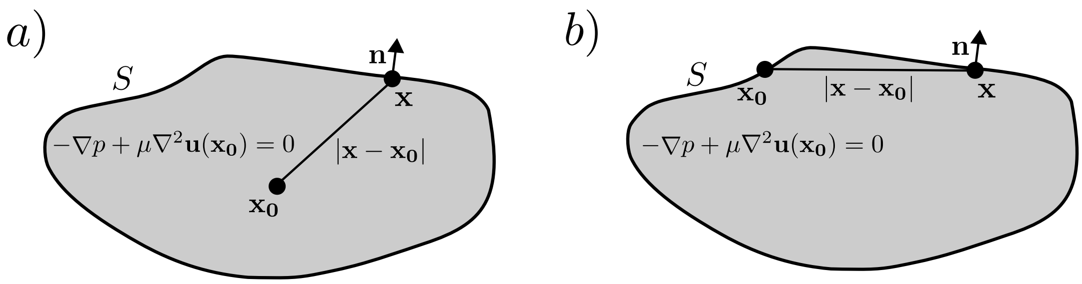

Figure 6.2: A fluid domain governed by Stokes flow, bounded by an enclosing surface S. (a) The field point $\mathbf{x_0}$ is located inside the domain. (b) The field point $\mathbf{x_0}$ is located at the boundary of the domain.

6.2.2. GOVERNING EQUATIONS FOR LINEAR ELASTICITY

The governing equations of Stokes flow are now compared to those of linear elasticity. The equation for linear elasticity are for example given by Zechner [48]. Static equilibirum is described by:

$$\nabla\sigma(\mathbf{x}) + \mathbf{F}(\mathbf{x}) = 0 \tag{6.3}$$

where σ equals the cauchy stress tensor and $\mathbf{F}$ is the body force per volume. The constitutive equation between stress and strain is given by Hooke's law:

$$\nabla\sigma(\mathbf{x}) = C(\lambda, \mu) : \epsilon(\mathbf{x}) \tag{6.4}$$

Here $\epsilon(\mathbf{x})$ is the infinitesimal strain tensor and C is the stiffness tensor. The stiffness tensor is a function of the Lame constants λ and μ, and can be replaced by the more commonly known Young's modulus (E) and the Poisson's ratio (ν).

$$\lambda = \frac{E\nu}{(1-2\nu)(1+\nu)} \tag{6.5}$$

$$\mu = \frac{E}{2(1+\nu)} \tag{6.6}$$

The third and final equation is the relation between strain and displacement:

$$\epsilon(\mathbf{x}) = 0.5[\nabla\mathbf{u} + (\nabla\mathbf{u})^{\mathbf{T}}] \tag{6.7}$$

Finally, Equation 6.8 is found, which is a partial differential equation with the force per volume $\mathbf{f(x)}$ as a function of displacement $\mathbf{u(x)}$. This derivation is discussed explicitly in Zechner [48].

$$-(\lambda+2\mu)\nabla\cdot\nabla\mathbf{u(x)} + \mu\nabla\times(\nabla\times\mathbf{u(x)}) = \mathbf{f(x)} \tag{6.8}$$

Note that Equation 6.8 looks very different from the equations for Stokes flow. By re-writing these PDEs to boundary integral equations it will be shown that the method for arbitrary domains is very similar. In fact the solutions are exactly the same as those for incompressible linear elastic material. For 2D problems one can either assume plane strain or plane stress. In the case of plain strain the displacement in the 3rd direction is not considered in the above equation. However the stress component σ_3 exists and can be calculated by:

$$\sigma_3 = \frac{E\nu(\epsilon_1+\epsilon_2)}{(1-2\nu)(1+\nu)} \tag{6.9}$$

Note that for an incompressible material σ_3 goes to infinite.

6.3. BOUNDARY INTEGRAL EQUATIONS

The boundary integral method solves the partial differential equations such as given by Equations 6.1 and 6.8 by rewriting them in the following form:

$$\beta u_j(\mathbf{x_0}) = \int_S f_i(\mathbf{x})\mathbf{U}_{ij}(\mathbf{x},\mathbf{x_0})\mathrm{d}S(\mathbf{x}) - \int_S u_i(\mathbf{x})\mathbf{T}_{ijk}(\mathbf{x},\mathbf{x_0})n_k(\mathbf{x})\mathrm{d}S(\mathbf{x}) \tag{6.10}$$

The usual Einstein summation convention is used. Here n_k is the k^{th} component of the outward-pointing unit normal vector of boundary S. $\mathbf{U}_{ij}$ and $\mathbf{T}_{ijk}$ are the fundamental solutions. The essence of the boundary element method is that any linear partial differential equation can be solved when the right fundamental solutions are known.

In the following section it will be proven that solving the equations for Stokes flow is exactly the same as solving the equations of incompressible linear elasticity by comparing their respective fundamental solutions.

6.3.1. FUNDAMENTAL SOLUTIONS FOR STOKES FLOW

For Stokes flow Equation 6.10 becomes [49]:

$$\beta u_j(\mathbf{x_0}) = 8\pi u_j(\mathbf{x_0}) = \frac{1}{\mu}\int_S f_i(\mathbf{x})\mathbf{U}_{ij}(\mathbf{x},\mathbf{x_0})\mathrm{d}S(\mathbf{x}) - \int_S u_i(\mathbf{x})\mathbf{T}_{ijk}(\mathbf{x},\mathbf{x_0})n_k(\mathbf{x})\mathrm{d}S(\mathbf{x}) \tag{6.11}$$

$\mathbf{U}_{ij}$ and $\mathbf{T}_{ijk}$ are the fundamental solutions, which for 3D Stokes flow read:

$$\mathbf{U}_{ij} = \frac{\delta_{ij}}{r} + \frac{(x_i-x_i^0)(x_j-x_j^0)}{r^3} \tag{6.12}$$

$$\mathbf{T}_{ijk} = -6\frac{(x_i-x_i^0)(x_j-x_j^0)(x_k-x_k^0)}{r^5} \tag{6.13}$$

Here x_i^0 are the components of $\mathbf{x_0}$, and $r = |\mathbf{x}-\mathbf{x_0}|$. Furthermore, as can be inferred from Equation 6.11, the constant β is taken as $\beta = 8\pi$. This is only valid if $\mathbf{x_0}$ is located inside the domain. If $\mathbf{x_0}$ is located at the boundary S, β should be taken equal to $\beta = 4\pi$.

Apart from evaluating the solution inside the domain once the solution at the boundary S is known, Equation 6.11 can be used to solve a Stokes problem by locating $\mathbf{x_0}$ on the boundary, see Figure 6.2b. In that case Equation 6.11 reads:

$$\beta u_j(\mathbf{x_0}) = 4\pi u_j(\mathbf{x_0}) = \frac{1}{\mu}\int_S f_i(\mathbf{x})\mathbf{U}_{ij}(\mathbf{x},\mathbf{x_0})\mathrm{d}S(\mathbf{x}) - \int_S u_i(\mathbf{x})\mathbf{T}_{ijk}(\mathbf{x},\mathbf{x_0})n_k(\mathbf{x})\mathrm{d}S(\mathbf{x}) \tag{6.14}$$

Equation 6.14 describes a relation between the traction $\mathbf{f}(\mathbf{x})$ and the velocity $\mathbf{u}(\mathbf{x})$. Note that if either $\mathbf{f}(\mathbf{x})$ or $\mathbf{u}(\mathbf{x})$ is known at the boundary, the remaining unknown can be solved using Equation 6.14. For an external problem with an infinite domain an additional term of $8\pi u_j(\mathbf{x_0})$ appears on the left hand side of Equation 6.14.

Note that for Stokes flow the traction $\mathbf{f}(\mathbf{x})$ is related to the stress tensor σ_{ik} as $f_i = \sigma_{ik}n_k$ with [49]:

$$\sigma_{ik} = -p\delta_{ik} + \mu\left(\frac{\partial u_i}{\partial x_k} + \frac{\partial u_k}{\partial x_i}\right) \tag{6.15}$$

The BEM for Stokes flow can also be applied in 2D. In that case, the flowfield $\mathbf{u}(\mathbf{x_0})$ inside the 2D domain can be expressed as [49]:

$$\beta u_j(\mathbf{x_0}) = 4\pi u_j(\mathbf{x_0}) = \frac{1}{\mu}\int_S f_i(\mathbf{x})\mathbf{U}_{ij}(\mathbf{x},\mathbf{x_0})\mathrm{d}S(\mathbf{x}) - \int_S u_i(\mathbf{x})\mathbf{T}_{ijk}(\mathbf{x},\mathbf{x_0})n_k(\mathbf{x})\mathrm{d}S(\mathbf{x}). \tag{6.16}$$

The appropriate fundamental solutions for 2D Stokes flow read [49]:

$$\mathbf{U}_{ij} = -\delta_{ij}\log(r) + \frac{(x_i - x_i^0)(x_j - x_j^0)}{r^2}, \tag{6.17}$$

$$\mathbf{T}_{ijk} = -4\frac{(x_i - x_i^0)(x_j - x_j^0)(x_k - x_k^0)}{r^4}. \tag{6.18}$$

When $(\mathbf{x_0})$ is located on the boundary, the integral equation will read [49]:

$$\beta u_j(\mathbf{x_0}) = 2\pi u_j(\mathbf{x_0}) = \frac{1}{\mu}\int_S f_i(\mathbf{x})\mathbf{U}_{ij}(\mathbf{x},\mathbf{x_0})\mathrm{d}S(\mathbf{x}) - \int_S u_i(\mathbf{x})\mathbf{T}_{ijk}(\mathbf{x},\mathbf{x_0})n_k(\mathbf{x})\mathrm{d}S(\mathbf{x}). \tag{6.19}$$

For an external problem with an infinite domain in 2D Stokes flow, an additional term of $4\pi u_j(\mathbf{x_0})$ appears on the left hand side of Equation 6.19.

6.3.2. FUNDAMENTAL SOLUTIONS FOR LINEAR ELASTICITY

The BEM for linear elasticity allows the calculation of the displacement field $\mathbf{u}(\mathbf{x_0})$ inside a 3D deformable solid domain as function of the solution $\mathbf{u}(\mathbf{x})$ and traction field $\mathbf{f}(\mathbf{x})$ at the boundary S. The same Equation 6.11 as for Stokes flow can now be used in which $\mathbf{u}(\mathbf{x_0})$ is the displacement field, and μ the shear modulus of the material. The corresponding fundamental solutions for 3D linear elasticity are given as follows [49]:

$$\mathbf{U}_{ij} = \frac{1}{2(1-\nu)}\left[(3-4\nu)\frac{\delta_{ij}}{r} + \frac{(x_i - x_i^0)(x_j - x_j^0)}{r^3}\right] \tag{6.20}$$

$$\mathbf{T}_{ijk} = -\frac{1}{1-\nu}\left[3\frac{(x_i - x_i^0)(x_j - x_j^0)(x_k - x_k^0)}{r^5} + \frac{1-2\nu}{r^3}\left(-\delta_{ij}(x_k - x_k^0) + \delta_{ki}(x_j - x_j^0) + \delta_{kj}(x_i - x_i^0)\right)\right] \tag{6.21}$$

Note that for an incompressible material ($\nu = 0.5$) the fundamental solutions are identical to the fundamental solutions of the Stokes problem.

In a analogous way, the BEM can be used to obtain the fundamental solutions for the 2D linear elasticity problem. The appropriate fundamental solutions in this case read [49]:

$$\mathbf{U}_{ij} = \frac{1}{2(1-\nu)}\left[-(3-4\nu)\delta_{ij}\log(r) + \frac{(x_i - x_i^0)(x_j - x_j^0)}{r^2}\right] \tag{6.22}$$

$$\mathbf{T}_{ijk} = -\frac{1}{1-\nu}\left[2\frac{(x_i - x_i^0)(x_j - x_j^0)(x_k - x_k^0)}{r^4} + \frac{1-2\nu}{r^2}\left(-\delta_{ij}(x_k - x_k^0) + \delta_{ki}(x_j - x_j^0) + \delta_{kj}(x_i - x_i^0)\right)\right] \tag{6.23}$$

The fundamental solutions for 2D and 3D Stokes flow and for linear elasticity are now shown. Note that for incompressible material $\nu = 0.5$. The reader can check that in this case the equations for Stokes flow become equal to those of linear elasticity.

By examining the fundamental solution one additional key characteristic of the boundary element method appears. The r in the denominator gives a singularity when $\mathbf{x} = \mathbf{x_0}$. This will give rise to problems in the numerical implementation.

So far no inaccuracies have been introduced in solving the underlying model. Only assumptions in the description of the partial differential equations have caused inaccuracies. Examples of such assumptions are the linearisation of the kinematics (small linear kinematics) or linear stress strain behaviour. It is clear that the boundary integrals above are not analytically solvable for arbitrary domains. Therefore, the boundary S will be subdivided into sections called boundary elements. These boundary elements can be solved numerically, and form a general method of solving the above equations for arbitrary domains.

6.4. DISCRETISATION

In this section the discretisation of the linear elasticity problem using the Boundary Element Method (BEM) will be discussed. This analysis is restricted to the 2D plain strain problems, for which Equation 6.19 applies. By seeding the enclosing surface S of a 2D domain by nodes, Equation 6.19 can be discretised. Note that for a 2D domain the enclosing surface S is essentially a line, see Figure 6.3.

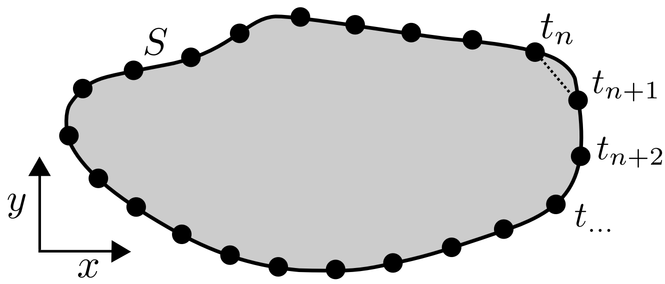

Figure 6.3: Schematic representation of the surface discretization used in the BEM for a 2D plain strain domain.

In this thesis linear first order elements are used to describe the boundary of the domain. This means that the shape of each element that builds up the surface S is described by a line. If the total number of nodes equals N, the total number of elements M is given by $M = N - 1$. The dashed line in Figure 6.3 represents one linear element. The length of this element is given by:

$$t_{n+1} - t_n = \sqrt{(y_{n+1} - y_n)^2 + (x_{n+1} - x_n)^2} \tag{6.24}$$

Here t is the curve parameter that runs along the discretized surface. The integrals appearing in Equation 6.19 can be approximated by using of the definition of t. For example, the first integral in Equation 6.19 can be expressed as:

$$\int_S f_i(\mathbf{x})\mathbf{U}_{ij}(\mathbf{x},\mathbf{x_0})\mathrm{d}S(\mathbf{x}) \approx \sum_{n=1}^{N-1} \int_{t_n}^{t_n+1} f_i(\mathbf{x}(t))\mathbf{U}_{ij}(\mathbf{x}(t),\mathbf{x_0})dt \tag{6.25}$$

Typically a system of equations is required which give the solution for an unknown $f_i(\mathbf{x}(t))$ at a node n. By linear interpolation it is possible to describe $f_i(\mathbf{x}(t))$ on the interval $[t_n, t_{n+1}]$ as follows:

$$\sum_{n=1}^{N-1} \int_{t_n}^{t_n+1} f_i(\mathbf{x}(t))\mathbf{U}_{ij}(\mathbf{x}(t),\mathbf{x_0})dt \approx \sum_{n=1}^{N-1} \int_{t_n}^{t_n+1} \left[f_i(\mathbf{x}(t_n))\frac{t_{n+1}-t}{t_{n+1}-t_n} + f_i(\mathbf{x}(t_{n+1}))\frac{t-t_n}{t_{n+1}-t_n} \right] \mathbf{U}_{ij}(\mathbf{x}(t),\mathbf{x_0})dt \tag{6.26}$$

To solve Equation 6.26 numerically it is discretized as follows. First $t = t(X)$ is parameterized such that the interval $[t_n, t_{n+1}]$ is mapped onto $[-1, 1]$ when using X as variable. This corresponds to:

$$t(X) = \frac{t_{n+1} - t_n}{2}(X+1) + t_n. \tag{6.27}$$

By substituting this relation it is possible to evaluate the integral on the right hand side of Equation 6.26 on the interval $[-1,1]$ by using Gauss-Legendre quadrature with pre-calculated weights as follows:

$$\begin{aligned}
&\sum_{n=1}^{N-1}\int_{t_n}^{t_n+1}\left[f_i(\mathbf{x}(t_n))\frac{t_{n+1}-t}{t_{n+1}-t_n}+f_i(\mathbf{x}(t_{n+1}))\frac{t-t_n}{t_{n+1}-t_n}\right]\mathbf{U}_{ij}(\mathbf{x}(t),\mathbf{x_0})\,dt\\
&\quad=\sum_{n=1}^{N-1}\frac{t_{n+1}-t_n}{2}\int_{-1}^{1}\left[f_i(\mathbf{x}(t_n))(\frac{1}{2}(1-X))+f_i(\mathbf{x}(t_{n+1}))(\frac{1}{2}(1+X))\right]\mathbf{U}_{ij}(\mathbf{x}(t(X)),\mathbf{x_0})\,dX\\
&\quad\approx\sum_{n=1}^{N-1}\frac{t_{n+1}-t_n}{2}\sum_k w_k\left[\left[f_i(\mathbf{x}(t_n))(\frac{1}{2}(1-X_k))+f_i(\mathbf{x}(t_{n+1}))(\frac{1}{2}(1+X_k))\right]\mathbf{U}_{ij}(\mathbf{x}(t(X_k)),\mathbf{x_0})\right]
\end{aligned}\tag{6.28}$$

Here X_k and w_k are the locations of the Gaussian points and of the Gaussian weights, respectively, which can be pre-calculated for any given number of Gaussian points. Equation 6.28 is valid for any $\mathbf{x_0}$ placed on the surface S. Now $\mathbf{x_0}$ is placed on the nodes such that it represents the surface $\mathbf{x}_l$, where $l=(1,2,\ldots,N-1,N)$. By using Equation 6.28 finally a system of equations is written such that the matrix vector product follows as:

$$\begin{aligned}
&\sum_{n=1}^{N-1}\frac{t_{n+1}-t_n}{2}\sum_k w_k\left[\left[f_i(\mathbf{x}(t_n))(\frac{1}{2}(1-X_k))+f_i(\mathbf{x}(t_{n+1}))(\frac{1}{2}(1+X_k))\right]\mathbf{U}_{ij}(\mathbf{x}(t(X_k)),\mathbf{x}_l)\right]\\
&\qquad=\mathbf{U}\cdot\begin{bmatrix}f_{x,1}\\ f_{y,1}\\ f_{x,2}\\ f_{y,2}\\ \vdots\\ f_{x,N}\\ f_{y,N}\end{bmatrix}=\mathbf{U}\cdot\mathbf{f}
\end{aligned}\tag{6.29}$$

The components of f_i have been written out explicitly so that one can see that in 2D they are f_x and f_y. Furthermore $f_{i,n}=f_i(\mathbf{x}(t_n))$. In the 2D case $\mathbf{U}$ has the size $2N\times 2N$. The second integral in Equation 6.19 can be discretised in the same way. The discrete version of Equation 6.19 finally becomes:

$$\beta\mathbf{u}=\frac{1}{\mu}\mathbf{U}\cdot\mathbf{f}-\mathbf{T}\cdot\mathbf{u}\tag{6.30}$$

here $u=[u_{x,1},u_{y,1},u_{x,2},u_{y,2},\ldots,u_{x,N},u_{y,N}]^T$. Since $\mathbf{U}$ and $\mathbf{T}$ contain coefficients which are dependent on the geometry, on the discretisation and on the known fundamental solution it appears that Equation 6.30 is a linear set of equations which can be solved by a software package. To do this Equation 6.30 is rearranged to:

$$[\mathbf{A}]\cdot\mathbf{x}=\mathbf{b}\tag{6.31}$$

in which $[A]$ is a full constant coefficient matrix, $\mathbf{x}$ an unknown vector and $\mathbf{b}$ a vector containing the known boundary variables. Note that at this point no steps have been made to correct for the singular behaviour of the fundamental solutions. When $\mathbf{x}_l$ approaches $\mathbf{x}$ the solution explodes and the numerical integration method used becomes inaccurate. To remove the singular behaviour of the fundamental solutions an additional solution is subtracted. This approach is provided by Klaseboer and will not be further discussed in this thesis [42].

6.5. VALIDATION

In the following section a validation of the described method is given. The results for planar 2D will be compared with the analytical solution for a Bernouilli beam. First the problem is shown and the analytical solution for it is given. Next this problem is solved with boundary elements and the convergence of the solution is checked. Finally, the BEM results are compared with the analytical results.

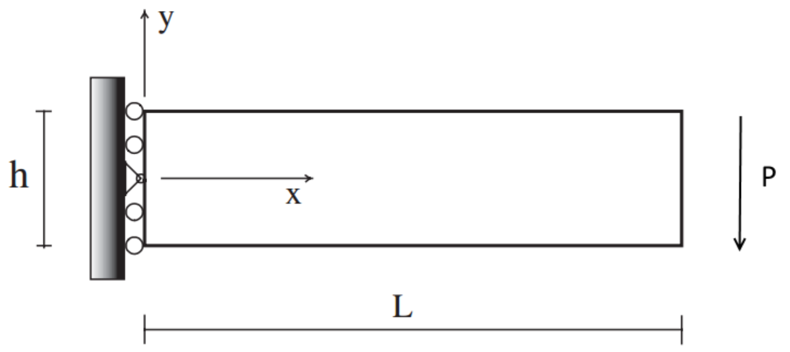

Figure 6.4: Definition sketch of a Bernoulli bending beam with height h, length L and force P. The problem is defined in plain strain. [12]

6.5.1. ANALYTICAL PROBLEM

In Figure 6.4 the definitions of a typical bending beam are shown. The deformation u in the y direction can be described by:

$$u(x) = \frac{P * x^3}{3E^* I} \tag{6.32}$$

$$I = \frac{h^3}{12} \tag{6.33}$$

$$E^* = \frac{E}{(1-\nu^2)} \tag{6.34}$$

in which P is the force per meter, L is the length, E^* is the plain strain E-modulus, h is the height and I is the moment of inertia.

Note that the plain strain E-modulus is used, to enable applying the incompressible plain strain formulation of the boundary elements. The input parameters used are given in Table 6.1.

Table 6.1: The input parameters of the described bending beam problem.

Parameter	Value
Modulus of elasticity (E)	1000 MPa
P	100 N/m
Height	1 m
Length	5 m
Poisson's ratio (ν)	0.5

6.5.2. BEM MODEL

The mesh of the BEM model is shown in Figure 6.5. Note that all normal vectors are pointing outwards. The beauty of the boundary element mesh is that only nodes are placed on the boundary of the problem. The model is built with an equidistant mesh.

The boundary conditions are as shown in Figure 6.4. One node is placed at $x = 0$ and $y = 0.5$. All other points along $x = 0$ are constrained in the x-direction. The force is applied as a distributed force at $x = L$.

Convergence is tested by comparing the maximum deviation with respect to the analytical solution.

$$\text{relative error} = \frac{u(x=l) - u(x=l)_{\text{Anal.}}}{u(x=l)_{\text{Anal.}}} \tag{6.35}$$

The convergence of the solution is shown in Figure 6.6.

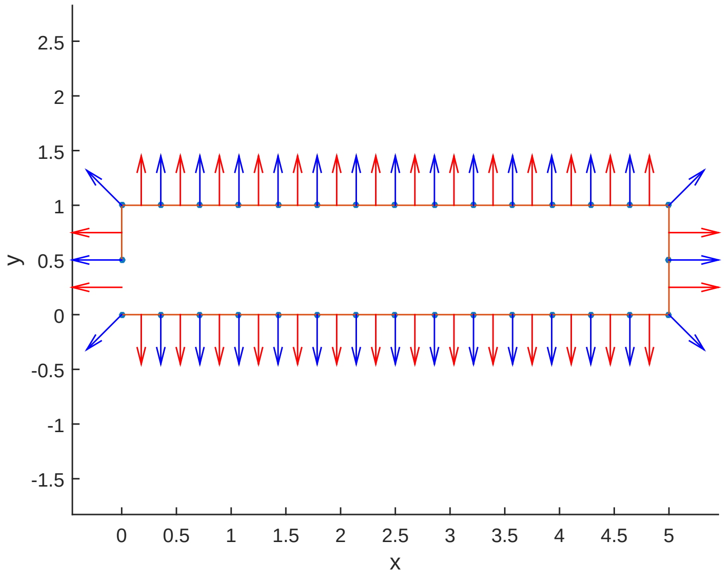

Figure 6.5: The boundary element mesh of the Bernoulli beam problem. Note that the normal vectors of the elements and nodes are pointing outwards. This mesh has 106 nodes.

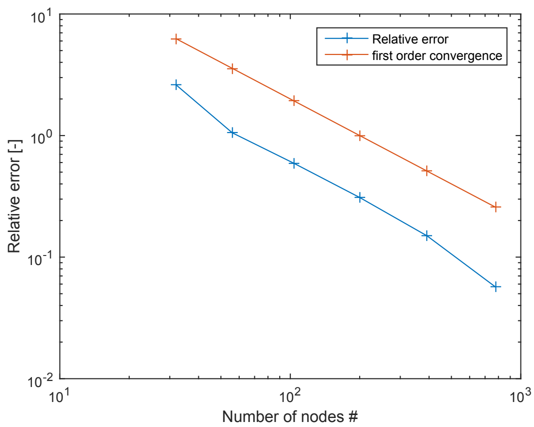

Figure 6.6: The relative error as function of the number of nodes. As one can see, the model converges with first order.

6.5.3. RESULTS

The results of the deformation and stress are shown in Figure 6.7. The interior results are not corrected for the singular behaviour. Therefore, some disturbance in the stress results can be seen in the solution near the boundary.

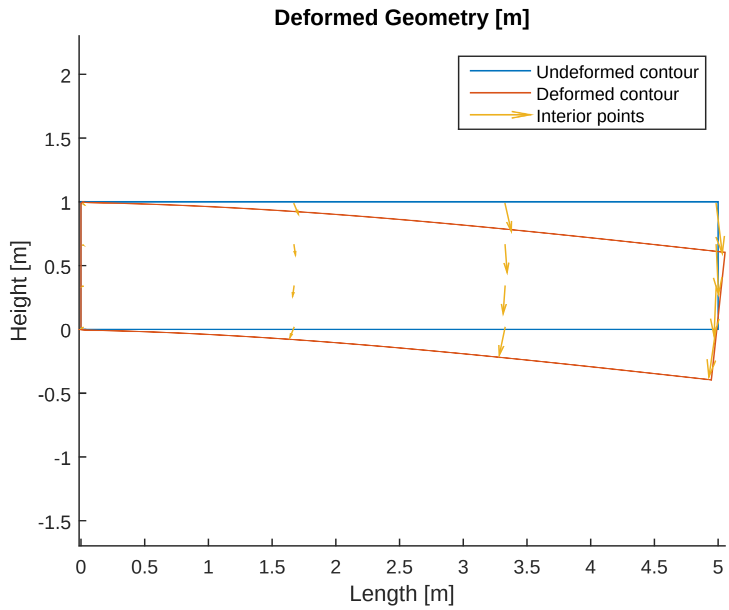

(a)

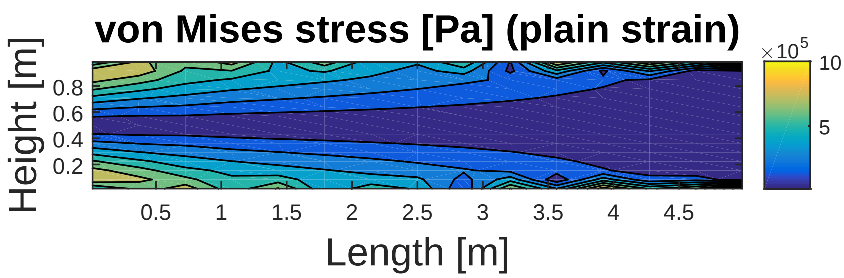

(b)

Figure 6.7: The solution of the Bernoulli beam problem. The model converges to the analytical solution with first order accuracy and with a relative error of 0.7% for the finest mesh that has been applied. The calculated stress is typical for a bending beam. Note that disturbances are seen near the boundary caused by the singular behaviour of the elements.

6.6. CONCLUSION

In this chapter a boundary element model was presented. It was shown that this model can describe both linear elasticity and Stokes flow. Since only the boundary of the mesh has to be discretised, this method can easily accommodate a large mesh refinement. This makes this method good in building models where local mesh refinement is needed. The method has been validated with the known problem of a bending Bernoulli beam.

7

BOUNDARY ELEMENT LUBRICATION MODEL

In this chapter the boundary conditions of lubricated friction are applied on the linear elasticity boundary element model. The input parameters and governing equations are discussed first. Secondly the numerical implementation is shown. Since the lubrication equation is highly non linear an iteration scheme must be used. Finally, it is shown that the model converges. A parameter study is left for future work.

7.1. MODEL

The boundary element model captures both the model to predict the sealing disk deformation and the lubrication model. By doing this it is no longer necessary to specify an angle β and force F_{wall} as input parameters. Because β is now not specified anymore we can choose to define the chamfer in the undeformed position by a chamfer length t_w and by an angle α. Note that t_w differs from c because it no longer runs parallel to the pipeline wall.

The input parameters now become: E-modulus (E), Poisson's ratio (ν), sealing disk radius (r_s), sealing disk inner radius (r_i), sealing disk thickness (t), chamfer length (t_w), pipe radius (r), friction number (K_s), wall asperity height (σ_a), dry friction coefficient (μ_{dry}), pig velocity (u_{pig}) and viscosity (η). These parameters are shown in Figure 7.1.

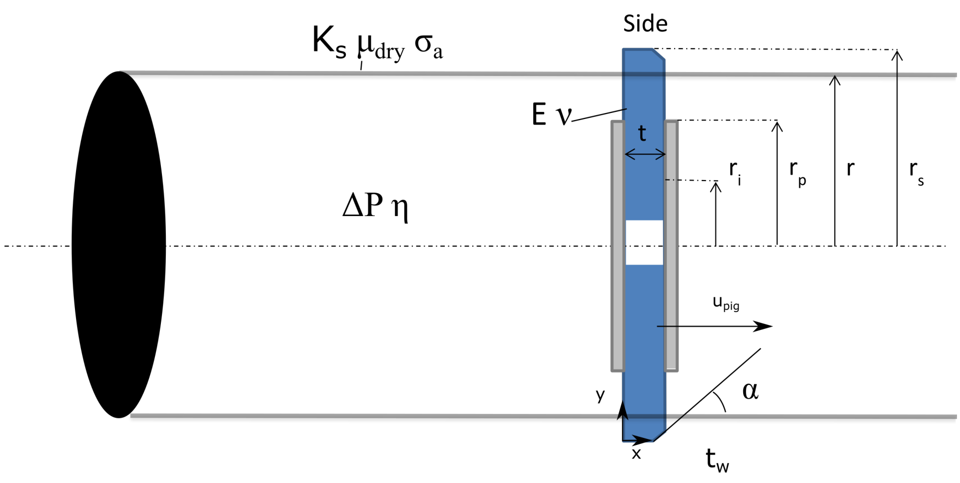

Figure 7.1: A sealing disk clamped between spacer disks with all design dimensions.

The model is described by plain strain, and all values thus are per meter circumference. The sealing disk is constrained at the location of the spacer disk. By integrating the constraint force in the y-direction along these nodes the value for F_{wall} is found. The friction force can be found in a similar way by integrating the force component in the x-direction. The coefficient of friction can be found as:

$$\mu = \frac{\int f_y}{\int f_x} \tag{7.1}$$

Here the integral is taken along the contact area.

The boundary conditions are applied with the Greenwood-Wiliamson method for planar lubrication as described in Chapter 5. Along the bottom of the model two force components are applied by the asperity pressure $P_a(h)$ and by the fluid pressure $P_f(h)$. To find the asperity pressure and the fluid film pressure a height profile is necessary. The height profile is defined as:

$$h(x) = y + u_y - (r_s - r_p) \tag{7.2}$$

in which y equals the height of the sealing disk, which is set to zero at the feet. u_y is the deformation in the y-direction, and $r_s - r$ is the distance caused by the disk oversize. With this film height the boundary conditions can be defined as:

$$f_x = P_x = -\overrightarrow{n_x}\left(\mu_{\text{dry}} 0.707 K_s e^{-\frac{h}{\sigma a}} + P_f(h)\right) \tag{7.3}$$

$$f_y = P_y = -\overrightarrow{n_y}\left(0.707 K_s e^{-\frac{h}{\sigma a}} + P_f(h)\right) \tag{7.4}$$

Here n_x and n_y are the unit normal vectors on the surface of the disk geometry.

7.2. NUMERICAL IMPLEMENTATION

By using linear elasticity the problem becomes as follows:

$$P_f(h_{i+1}, h_i, h_{i-1}) + P_a(h_i) - P_t(h_1 ... h_N) = 0 \tag{7.5}$$

The fluid film height can not be simply varied, because the film height of each node is connected to the film height of all other nodes. Another issue is that the boundary element model uses linear displacements. This means that boundary conditions are applied on a geometry and that the responding deformations and constraint forces are calculated. However the deformations and constraint forces correspond to the undeformed position. This means that the applied boundary conditions are not satisfied at the deformed position. This makes the model not suited for large oversizes. Note that this method is also in contrast to the approach of the analytical model which assumes that the model must be in equilibirium in the deformed position. Of course the current boundary element model could be expanded for applications with large deformation as has been shown by Beer [46], Shiue [50] and Chen [51]. To do this typically the interior has to be discretized, which also implies that the boundary element method loses its attractive properties. This has not been explored in this thesis and therefore only linear deformations have been considered.

Assumption: Deformations are small enough so that influence on the boundary conditions can be neglected.

By making this assumption the boundary conditions can be applied on the non-deformed disk.

As can be seen by inspecting the lubrication equation the fluid pressure behaves highly non-linearly. Therefore an iteration scheme is proposed in which a relaxation factor can be defined. This relaxation factor takes the average of an old and new deformation position.

The iteration scheme is shown in Figure 7.2. The scheme starts at the undeformed position. Note that in this case the film height is negative since u_y is zero in Equation 7.2. When h becomes zero the fluid pressure has passed a singularity and the model will crash. Therefore when h is negative the value is replaced by $h = \sigma_a/10$. With this very low film height the fluid pressure will be so large that an initial deformation is imposed. Some remarks can be made on this initial estimate. When the pig velocity (u_{pig}) is very low the deformation is only caused by the asperities. However, the asperity pressure allows a fluid film height of less than zero. This means that the material is moved past the average wall asperity height. This case is currently cut-off and care must be taken when the fluid film height approaches the cut off criterion.

With the initial deformation a new fluid film height is found. Note that this fluid film height will be far too large and therefore both the fluid pressure and the asperity pressure will be near zero. This unstable nature is damped by averaging two film heights by a relaxation factor. The new fluid film height is defined by:

$$h^{n+1} = \frac{(\text{RELAX} - 1) * h^{n-1}}{\text{RELAX}} + \frac{h^n}{\text{RELAX}} \tag{7.6}$$

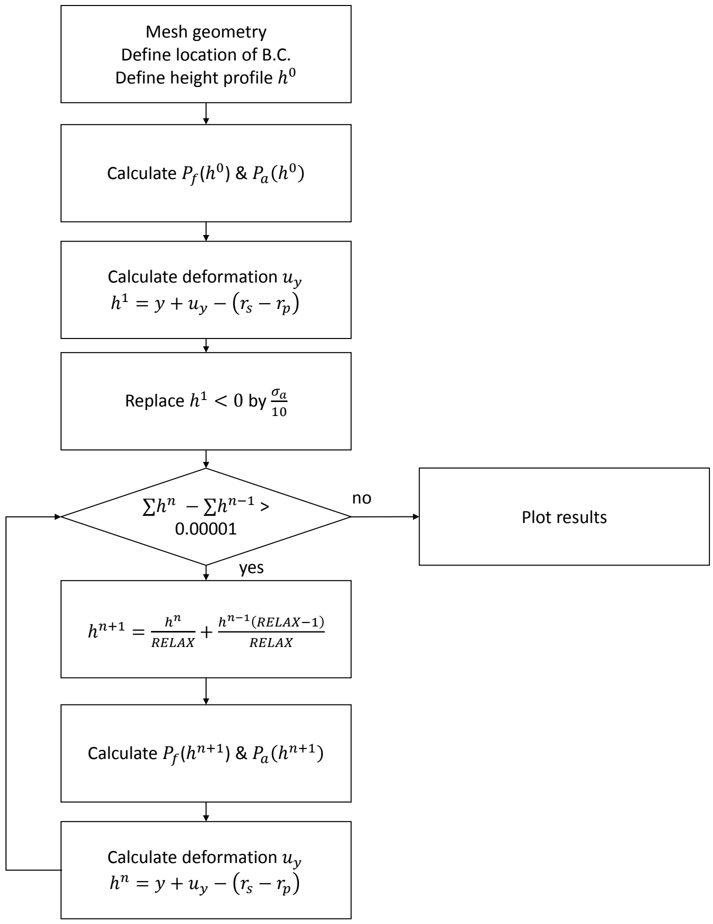

Figure 7.2: The iteration scheme used to calculate the fluid film height h.

When the iteration process shows unstable behaviour the relaxation denoted by the factor RELAX is increased.

This fluid film height is iterated until a film height is found which does not change anymore. Although it is good practice to iterate to convergence criteria with a physical meaning this has become more difficult since the earlier used criteria of pressure equilibrium can be used. This is obvious since the contact pressure is applied directly and so $P_t - P_f - P_a = 0$ holds per definition.

7.3. RESULTS

The used input parameters are given in Table 7.1, for which the geometry is shown in Figure 7.3.

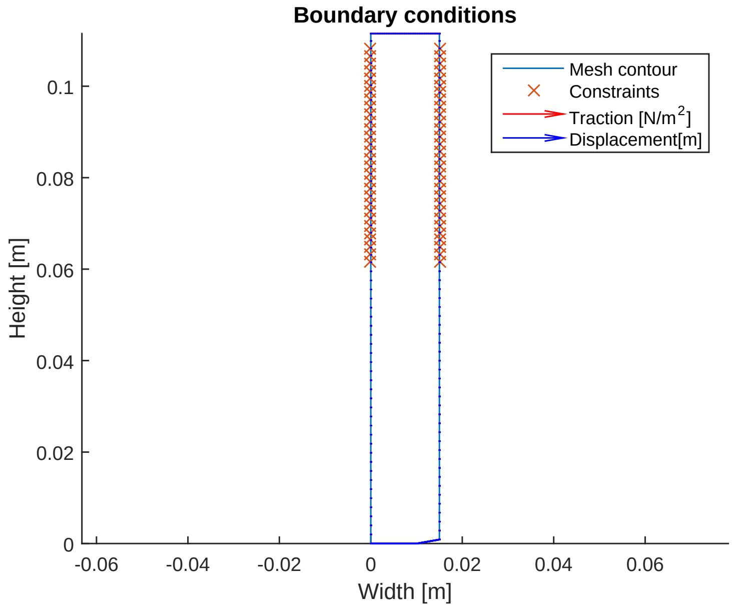

Figure 7.3: The geometry that corresponds with the input parameters given in Table 7.1. The constraints are both in the x and y direction.

Table 7.1: The input parameters of the boundary element lubrication model.

Parameter	Value
Modulus of elasticity (E)	6.5 MPa
Poisson's ratio (v)	0.5
Sealing disk radius (r_s)	0.1615 m
Sealing disk inner radius (r_i)	0.05 m
Spacer disk radius (r_i)	0.1 m
Sealing disk thickness (t)	0.015 m
Chamfer length (t_w)	0.005 m
Chamfer angle (α)	0.10
Pipe radius (r)	0.161 m
Friction number (K_s)	0.0115
Wall asperity height (σ_a)	6.7*10e-6 m
Dry friction coefficient (μ_{dry})	0.91 m
Pig velocity (u_{pig})	1 m
Viscosity (η)	0.001 Pa.s m

The calculated fluid film height for respectively 29, 65, 137 and 281 nodes is shown in Figure 7.4 .

The fluid film height calculated in this simulation is very high and therefore far in the lubrication regime. The calculated dispacement and traction as vectors for the geometry are given in Figure 7.5. The length of the vectors is scaled for clarity.

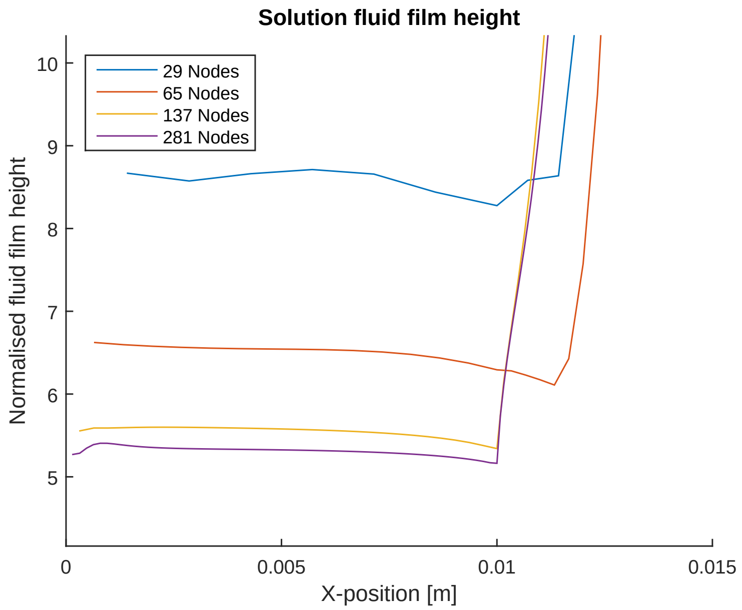

Figure 7.4: The normalised fluid film height for the input parameters given in Table 7.1. Note that the solution appears to converge. The fluid film height in this case is equal to 5.2 σ_a, which is very high. In this case lubrication would be very good.

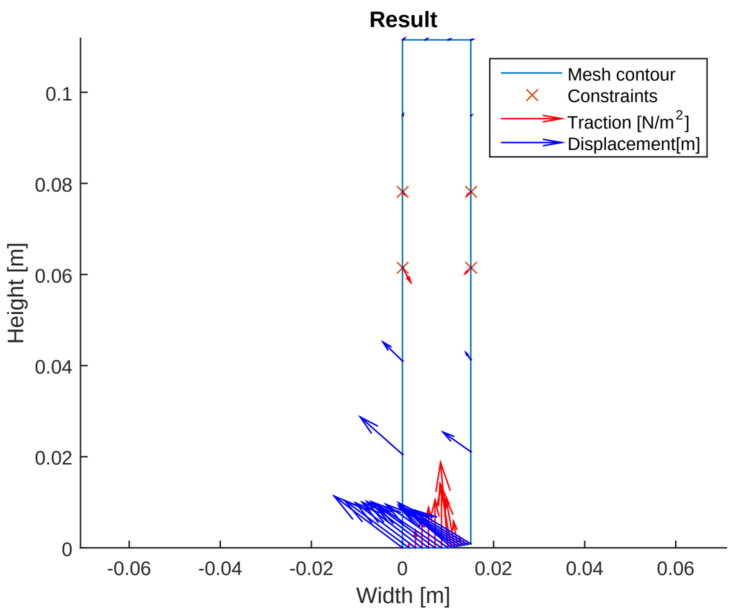

Figure 7.5: The displacement and traction vectors for the model with 29 nodes. Note that the mesh is very fine near the lubrication layer and very coarse along the remaining geometry. This shows that it is easy to refine the mesh locally.

7.4. CONCLUSION

The lubrication boundary conditions were coupled to a boundary element linear elasticity model. This makes it possible to describe the lubrication behaviour of a sealing disk. An iteration scheme was developed and it is shown that the solution converges when the mesh is refined. The validation of the cases and the parameter study is left for future work.

8

Flow loop measurements

An experiment has been performed to measure the pressure drop over a bypass pig. The measured pressure drop results are compared with an analytical solution. Finally, a conclusion is drawn on the validity of the analytical correlation in comparison to the measured results.

8.1. Introduction

As has been seen in Chapter 2, the motion of a pig is determined by a balance between the driving pressure force and the resisting friction force. Bypass pigs allow part of the fluid to move through the pig. Note that this fluid can be a liquid, a gas or a mixture of both. The pressure drop due to the friction of the bypassing fluid has been investigated with CFD studies by Azpiroz [38] and Liang [39]. This section describes pressure drop measurements carried out as part of this study for a model of a bypass pig. With these pressure drop measurements a drag coefficient can be deduced and this will be compared with values found in the literature.

8.2. Measurements

First a distinction must be made between the standard bypass pig and the disk bypass pig. A standard bypass pig has a constant bypass area in which fluid is allowed to pass the pig. A disk bypass pig has an additional disk placed in front of its bypass. The disk placed in front of the bypass creates an additional resistance for the bypassing fluid. A definition sketch of a disk bypass pig is given in Figure 8.1 with its dimensions in Table 8.1. This bypass pig has been manufactured. The roughness of the manufactured bypass pig is specified as 1e-6 m.

Table 8.1: Design dimensions of a bypass pig.

Parameter	Value
Diameter (D)	0.095 m
Bypass diameter (d)	0.032 m
Length (L)	0.1752 m
Disk size (d_{plate})	0.0356 m
Distance plate (w_{plate})	0.0112 m

Two series of measurements have been done. The used working fluid was water. Firstly, measurements were done for the bypass pig. Secondly, measurements were done for the disk bypass pig. The bypass pig without a deflector disk is shown in Figure 8.2. A glass case which can be filled with water has been manufactured around the glass tube. This is meant to reduce the refraction of light during visual inspection. The pressure drop over the bypass pig is measured with a differential pressure sensor. The connection of this pressure sensor can be seen at the bottom of the flow tube. The used pressure drop sensor is a PI-100 from which the results are stored with an Eurotherm recorder.

The mass flow through the flow tube is regulated with an FIC-100 which also stops the pump when the pressure becomes as low as 0.5 bar. In practice this means that the mass flow can be regulated and the pressure drop is measured in steps of 2.5 m^3/hr. With this mass flow the velocity and Reynolds number are calculated.

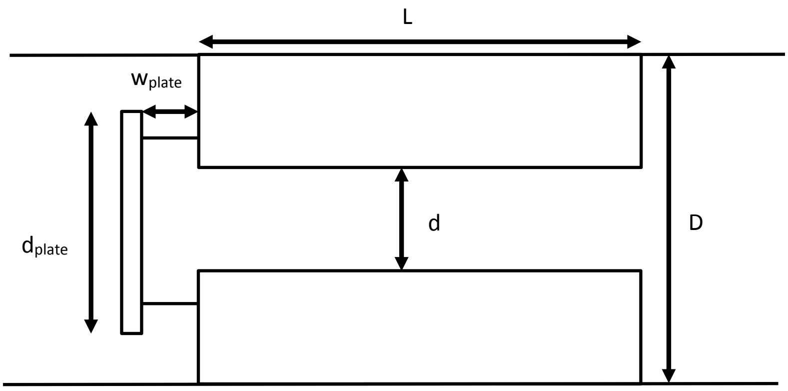

Figure 8.1: Definition sketch of a disk bypass pig.

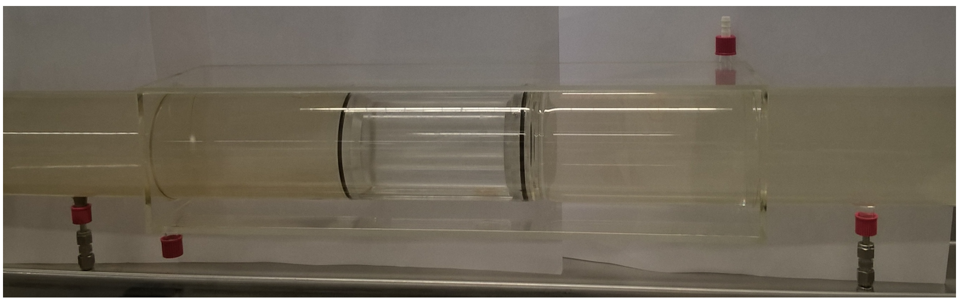

Figure 8.2: A picture of the experimental setup in which the pressure drop over the pig is measured. Note how the connections of the differential pressure sensor are placed.

The pressure drop is noted by hand and the average value of these five readings is taken. The standard deviation equals the standard deviation of these five readings.

The output of the flow tube is lower than the output of the bypass pig. This means that for low mass flows the tube is not totally filled. Readings in this regime are unreliable and therefore are excluded from this analysis.

8.3. RESULTS

The measurements are compared to the analytical results described by Idellchick [52]. Firstly the friction factor f is defined, secondly the pressure drop coefficient C_d and finally the pressure drop ΔP.

The friction factor for single phase, fully developed pipe flow is approximated by Churchill as:

$$f = 2\left(\left(\frac{8}{Re_{\text{bp}}}\right)^{12} + (A+B)^{-1.5}\right)^{\frac{1}{12}} \tag{8.1}$$

$$A = \left(2.457\ln\left(\left(\frac{7}{Re_{\text{bp}}}\right)^{0.9} + 0.27\frac{\epsilon}{D}\right)^{-1}\right)^{16} \tag{8.2}$$

$$B = \left(\frac{37530}{Re_{\text{bp}}}\right)^{16} \tag{8.3}$$

Here Re_{bp} is the Reynolds number based on the bypass diameter and the bypass bulk velocity. The parameters ϵ stands for the standardized wall roughness.

The pressure drop coefficient for a bypass pig without disk equals:

$$C_d = 0.5\left(1-\frac{A_1}{A_0}\right)^{0.75} + \frac{4fL}{D} + \left(1-\frac{A_1}{A_0}\right)^2 \tag{8.4}$$

in which A_1 denotes the area of the bypass and A_0 denotes the area of the flow tube.

The pressure drop coefficient for the disk bypass pig is approximated as [52]:

$$C_d = 0.5 * \left(1-\frac{A_1}{A_0}\right)^{0.75} + \frac{4fL}{d} + \left(\frac{2d_{plate}}{d}\right) + \left(\frac{0.155d^2}{w_{plate}^2} - 1.85\right) \tag{8.5}$$

Finally, the pressure drop is calculated as follows:

$$\Delta P = 0.5\rho C_d u^2 \tag{8.6}$$

To calculate the Reynolds number and the fluid velocity from the mass flow a density of 998 kg/m^3 and a viscosity of 1e-3 Pa.s are used.

In Figure 8.3(a) the differential pressure is shown for the standard bypass pig against the Reynolds number. Both the differential pressure predicted by Idelchick and the measurement results are shown. As can be seen, Idelchick over predicts the pressure drop and the pressure drop coefficient. The error bar shown is equal to one standard deviation.

In Figure 8.4 the pressure drop results are shown for the disk bypass pig model. Note that the correlation follows the measurement results very well.

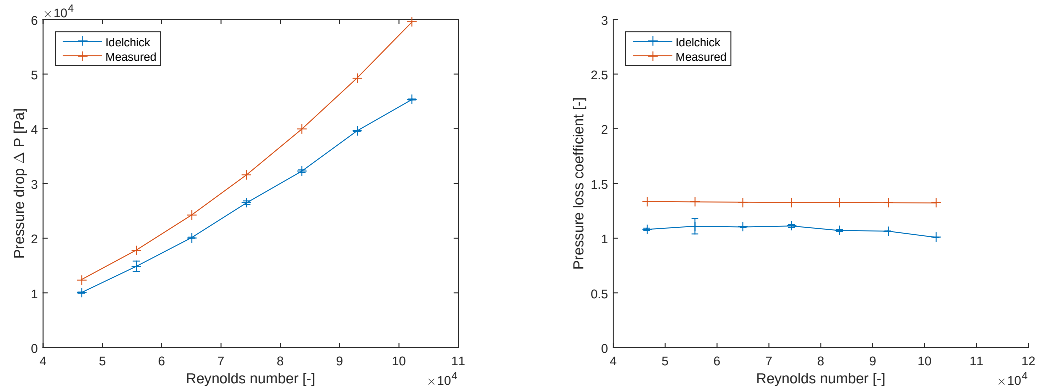

(a) Pressure drop results measured compared with the analytical solution.

(b) Pressure loss coeficient as calculated by 8.4.

Figure 8.3: Measurement results for a bypass pig without a disk. The error bar is defined by one standard deviation.

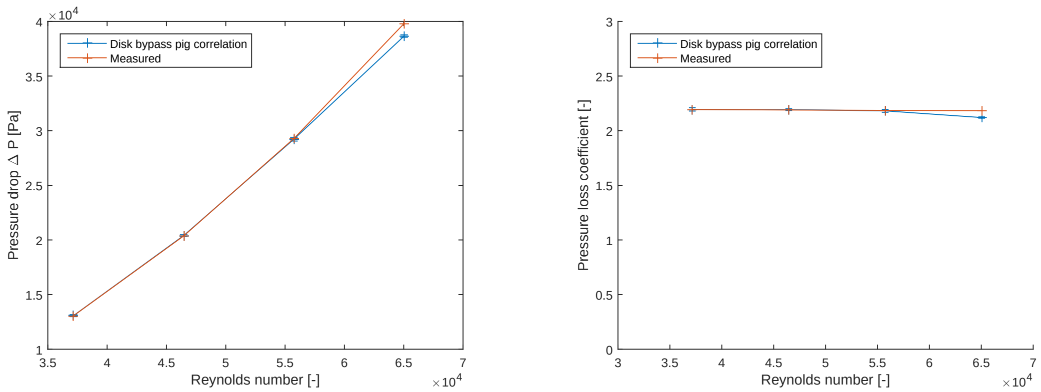

(a) Pressure drop results measured compared with the analytical solution.

(b) Pressure loss coeficient as calculated by 8.5.

Figure 8.4: Measurement results for a disk bypass pig. The error bar is defined by one standard deviation.

8.4. CONCLUSION

In this chapter pressure drop measurements were presented that were used to validate the correlations for a standard bypass pig and for a disk bypass pig. It was shown that the correlation given by Idelchick for a sudden expansion deviates from the measurements. This is somewhat surprising as it is the simplest geometry. Measurements were also performed for the disk bypass pig and the results are in good agreement with the correlation.

9
Conclusions and recommendations for future work

9.1. Conclusions

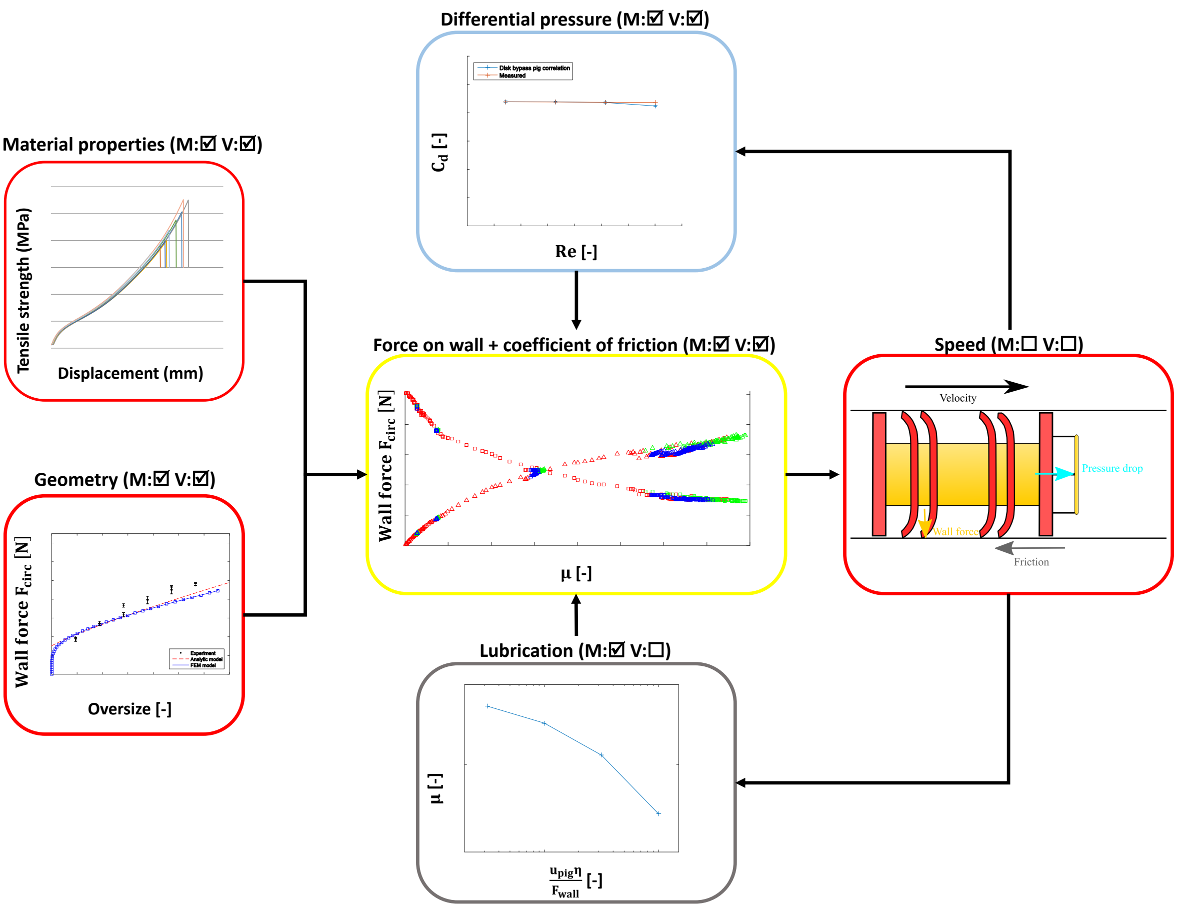

Figure 9.1: Most important pigging items placed in the framework. (M) model (V) validation.

At the beginning of this thesis the model of Cordell was introduced as a best practice to describe the pressure over a pig. This model gives the necessary pressure to drive a pig by using a factor, which depends on the pig type, divided by the pipe diameter. The results of the various aspects of the pig friction studied in the present thesis are summarized in the framework shown in Figure 9.1. The results for each specific item are described in the following subsections.

9.1.1. MATERIAL PROPERTIES

The material stiffness of the pig sealing disks is typically specified in by the Shore hardness. Firstly it was shown that the material of sealing disks can be described by a linear E-modulus. This was done by comparing the results from a non-linear finite element model to the results from a linear finite element model.

From this comparison it was concluded that the E-modulus given by the Gents equation is not valid for the relatively small strains typical for sealing disks. For small deformations the E-modulus of the used polyurethane will typically be higher.

The Shore hardness appeared to be an unreliable predictor of the E-modulus. In the wall force experiments, disks with the same specified Shore hardness appeared to have different E-moduli. However, it was also shown that the model was able to describe the wall force for different geometries when the material properties are known.

9.1.2. GEOMETRY

The geometry of a sealing disk can be described by four parameters: the clamping rate, the oversize, the thickness ratio and the chamfer ratio. The wall force model and the experiment described in this thesis were tested for a range of geometries. In this thesis the validity of these models for different thicknesses, clamping rates and material properties were validated for a range of oversizes.

It is difficult to specify which parameters have the main influence, since it is difficult to compare an increase in thickness with an increase in clamping rate. However, it can be concluded that in for typical oversizes the wall force can increase by a factor of 3.

9.1.3. WALL FORCE MODEL

The wall force model predicts the wall force for a certain geometry, for certain material properties and for a certain pressure drop as a function of the coefficient of friction. The experiment did not show the typical friction behaviour that is described by Coulomb's law. No μ_{static} and/or μ_{dynamic} were found. Other existing experiments were also unsuccessful in finding these values. However it was hoped that by obtaining more control on the sealing disk this value would be found. Although the experiment did not succeed in finding these two values, the wall force was measured for the entire range of values for the coefficient of friction, leading to the next two conclusions.

Firstly, for non lubricated cases (such as for pipelines filled with pressurized gas) the coefficient of friction is typically high. For high coefficients of friction the wall force becomes stable. The coefficient of friction in those cases can simply be determined by doing a small test. Typically, the value of μ will be between 0.2 and 0.4 . Note that this inaccuracy is roughly 33%.

Secondly, for highly lubricated cases the coefficient of friction will drop by orders of magnitude ($\mu < 0.1$). In those cases the wall force will converge to a finite value. The measured wall force for very low values of μ can be used to calculate if there is a chance that lubrication will occur by performing a simple analytical calculation. By solving the Reynolds equation for this load, in combination with the pig speed and the fluid viscosity for an approximate geometry the order of magnitude of the fluid film height can be calculated in seconds on a laptop. A typical approximate geometry is an inclined linear slider which is derived in Appendix E.2.

Overall the validated model can be easily solved in a spreadsheet program such as Excel and is useful in a quick first calculation of the necessary force to drive a pig. The accuracy of the prediction of the necessary driving pressure is reduced an order of magnitude difference to say a few tens percent difference.

9.1.4. LUBRICATION MODEL

When lubrication occurs it has a large effect on the friction of the pig. Lubrication is typically described by empirical models due to the unpredictable behaviour of: the wall roughness, the geometry of the contact area, and the availability of lubricant at the contact area. A first conclusion therefore is the importance of the Stribeck curve in the description of the friction of a pig. However in this thesis not an empirical approach but a modelling approach was taken.

In this thesis two lubrication models were developed. Firstly a relatively simple lubrication model which was able to describe the Stribeck curve quantitatively. This model could easily be coupled to the wall force model to give a general description of pigging. To couple the lubrication model to the wall force model a boundary element method approach was taken.

It was shown that the boundary element method is a useful method in solving this coupled problem since it allows for very fine meshes locally while it also describes the global behaviour accurately. It was shown that the boundary element method can be used to solve problems of linear elasticity. It was also shown that the boundary element method can easily be coupled to the phenomena related to lubrication such as wall asperities and fluid film lubrication. So far no validation cases of the lubrication effect were available, therefore the analysis was merely indicative.

9.1.5. PRESSURE DROP

To calculate the pressure drop over a bypass pig, analytical models and CFD models were already developed in previous thesis projects. A start has been made in validating these experiments. It was shown that for the simplest geometry the deviation between the measured pressure drop and the calculated pressure drop was roughly 35% . This was surprisingly large since it was the simplest geometry.

For the disk bypass pig the analytical expression was in good agreement with the measurements.

9.2. RECOMMMENDATIONS FOR FUTURE WORK

In this section the main recommendations for future work are given. Firstly suggestions for additional measurements which can be obtained by running the sealing disk experiment are given. Secondly recommendations are given on the subject of modelling the deformation of the sealing disk and its lubrication behaviour. Thirdly, the flow loop experiments performed were done very briefly. In this thesis it was not possible to validate the work done in various CFD studies.

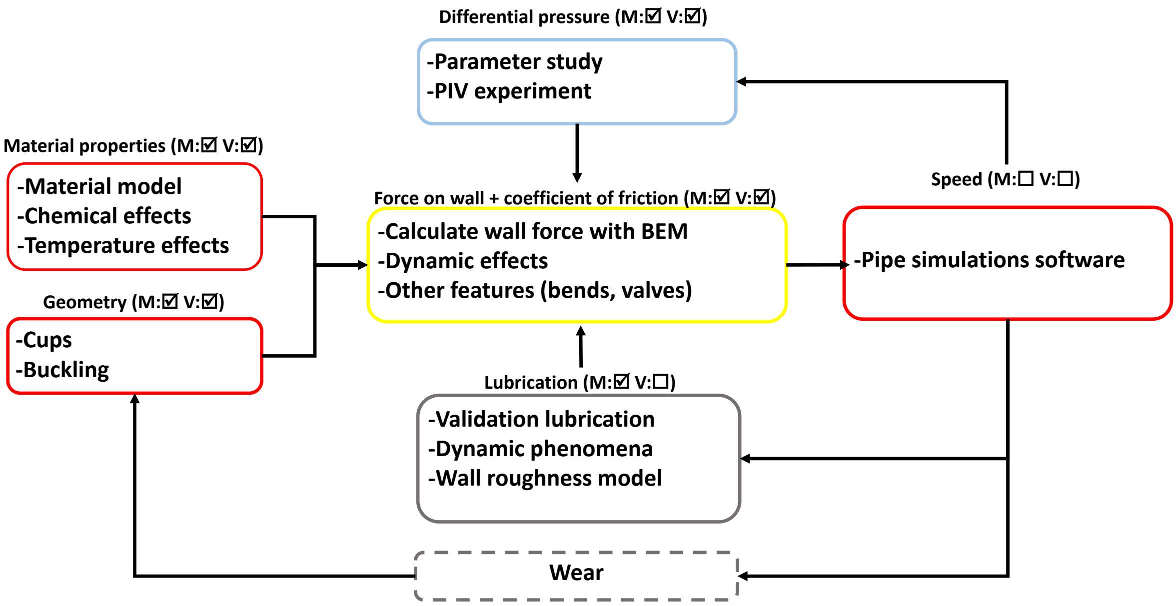

Figure 9.2: Recommendations for future work placed in the framework. (M) model (V) validation.

9.2.1. SEALING DISK EXPERIMENTS

In this thesis an experiment has been designed to measure the necessary force to deform a sealing disk into the relevant position. The working principle has been demonstrated, and now it is easy to follow up with new series of experiments.

Two factors are known to change the behaviour of polyurethane (being the pig sealing disk material) significantly: temperature and chemical reactivity. In the literature it is shown that the temperature can significantly influence the modulus of elasticity. The experiments obtained in this project were all done at room temperature. Pigs may be exposed to a range of temperatures, i.e from sub-zero Siberian conditions to desert conditions, which thus will have a strong effect on the pig material properties. However, there are no reasons to why these experiments cannot be done over this range of temperatures. For high temperatures the polyurethane material has the tendency to creep. Therefore, it can be interesting to also do experiments over longer periods of time.

A similar reasoning can be given on the influence of the chemical reactivity. No studies were found on the influence of the working fluid on the sealing disk. However, oil and condensate consist out of a large range of components. It is very likely that some of these components change the material behaviour. Therefore, the disks can be tested after exposing them over a certain period to such liquids.

It is also known that there are multiple diameter pigs. The sealing disks of these pigs buckle to fit in smaller diameter pipelines. The experiment designed in this thesis can be used for such pigs.

Finally, we make some remarks on expanding the current static experiment to a dynamic one. In the literature study done during the design of this experiment it was shown that it was very hard to control all parameters during a dynamic pig pull experiment. However by modelling, it was shown that the coefficient of friction can drop by an order of magnitud because of dynamic effects. An initial attempt has been made to model the lubrication behaviour of a pig, but no experimental validation has been done.

9.2.2. Modelling of pig sealing disks

It has been shown that when the material properties of a sealing disk are known it is possible to predict the pressure drop necessary to drive the pig with a finite element simulation. In this thesis a boundary element model has been presented to couple the local lubrication with the global deformation model.

The lubrication behaviour of a pig can cause unstable stick-slip motion. This model to describe the lubrication can serve two purposes. Firstly it is essential for the accurate description of the motion of pigs.

Secondly the model can be used to investigate the influence of the geometry on lubrication. During full fluid film lubrication wear can be neglected, while with dry friction wear will be significant. To describe the pig and its wearing mechanism during long pig runs the lubrication mechanism is essential. A choice can be made to try to destroy the lubrication mechanism to create a high friction pig which seals and moves with a constant velocity. However, another strategy could be to focus on the enhancement of lubrication. Forward leakage will be no problem for bypass pigs and wear will be insignificant during lubrication. A validation with experimental pig runs and a parameter study for the influence of the geometry on the lubrication can therefore be beneficial.

The current boundary element model still requires additional work to be able to describe the large deformation phenomena related to the sealing disk deformation. Next to this the current lubrication boundary condition could easily be extended to Stokes flow to predict the fluid flow behaviour beyond the small thin lubrication fluid film. Essential while doing this is an accurate description of the forward leakage.

9.2.3. Flow loop experiments

In this thesis a first experiment has been performed to measure the pressure drop over a pig. However, the analysis in this thesis was very briefly and many bypass pig geometries can still be tested. Firstly the currently used geometry can be varied for multiple bypass areas defined by the distance between the disk and the pig.

The setup was designed to do measurements for multiphase flows in which both water and air can pass through the bypass. Problems with the mass flow meter made these measurements impossible. However, further analysis of this is useful to validate the available results from CFD studies.

Finally, currently only the pressure drop has been measured. The glass configuration has been built to make it easy to do a visual inspection of the flow field. Initially this can be done by visual observation of the length of the recirculation zone (by adding particles). However, also more advanced techniques such as particle image velocimetry could be used.

9.3. Closure

In this thesis the framework from Chapter 2 was revisited. The material properties were validated. This appeared to be crucial in obtaining accurate values from the made models. The analytical and the finite element model were validated by experiments for various geometries. Also a lubrication model was made to predict the coefficient of friction. To couple lubrication to the wall force model a boundary element method code was written and validated with the analytical solution of a Bernoulli beam. Next, experiments were performed to measure the coefficient of drag over a bypass pig. Overall a lot of information and many models were made to contribute into the prediction of the motion of bypass pigs. These models are now left to other people to incorporate in other models that describe the behaviour of the pipeline systems.

A

Derivation wall force equations

A.1. Newton Raphson

The Newton Raphson method is used to find the roots of a function iteratively:

$$x_{n+1} = x_n - \frac{f(x_n)}{f'(x_n)} \tag{A.1}$$

By combining the given equations the following two functions are found:

$$f(\beta) : \beta(r - r_p) - \frac{\beta t \sin(\beta)}{2} + c\beta \sin(\beta)\cos(\beta) - (r_s - r_p)\sin(\beta) = 0 \tag{A.2}$$

$$f'(\beta) : (r - r_p) - (r_s - r_p)\cos(\beta) + c(\beta\cos(2\beta) + \sin(\beta)\cos(\beta)) - \frac{t}{2}(\sin(\beta) + \beta\cos(\beta)) \tag{A.3}$$

Because the model is typically valid for $\beta = 0...\pi/2$ an initial guess of $x_0 = \pi/4$ is taken.

A.2. External forces

The momentum in any point is found by multiplying the force with the arm tangential to the force.

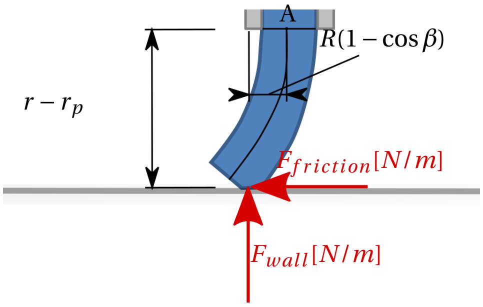

Figure A.1: The moment caused by external forces.

By using a simple geometry it can be shown that:

$$M_w = F_{\text{wall}}\left(R(1-\cos(\beta)) - \frac{t\cos\beta}{2}\right) r d\theta \tag{A.4}$$

$$M_f = F_{\text{friction}}(r - r_p) r d\theta \tag{A.5}$$

The pressure difference over the pig sealing disk follows the same approach. First the pressure difference is divided into a part parallel to the wall force which will be called the x-direction, and one component parallel to the friction force which will be called the y-direction. At each point of the sealing disk surface, the x-component of the pressure force will be $\Delta P, x = \Delta P \sin(\beta)$ and the y-component is $\Delta P, y = \Delta P \cos(\beta)$.

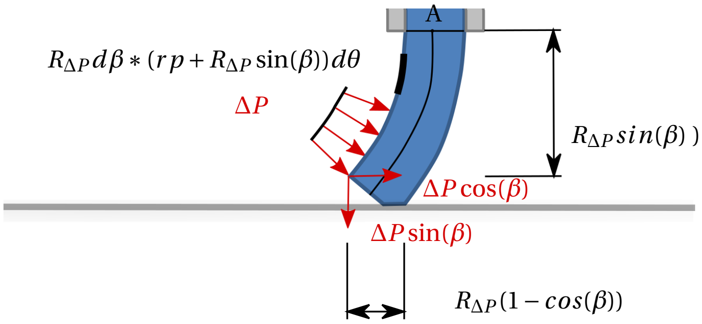

Figure A.2: Momentum $M_{\Delta P}$ with the definitions for: force, arm and area.

An infinitesimal small area of the sealing disk surface can be described by : $dA = R_{\Delta P} d\beta * (r_p + (R - t/2)\sin(\beta))d\theta$. For simplicity $(R - t/2)$ will be written as $R_{\Delta P}$.

The arm for the x component equals $R_{\Delta P} * (1 - \cos(\beta))$, and the arm for the y component is $R_{\Delta P}\sin(\beta)$. The moment contribution is found by multiplying the area with the sum of the x contribution and y contribution.

$$dM_{\Delta P} = (R_{\Delta P} d\beta * (r_p + R_{\Delta P}\sin(\beta))d\theta)\left[\Delta P\sin(\beta) * R_{\Delta P}(1 - \cos(\beta)) + \Delta P\cos(\beta) * R_{\Delta P}\sin(\beta))\right] \tag{A.6}$$

$$dM_{\Delta P} = \Delta P R_{\Delta P}^2 d\theta \sin(\beta)(r_p + R_{\Delta P}\sin(\beta))d\beta \tag{A.7}$$

To obtain the total moment, $dM_{\Delta p}$ is integrated over β to obtain

$$M_{\Delta P} = \Delta P R_{\Delta P}^2 d\theta \int_0^{\beta} r_p \sin(\beta) + R_{\Delta P}\sin(\beta)^2 d\beta \tag{A.8}$$

$$M_{\Delta P} = \Delta P R_{\Delta P}^2 d\theta \left(R_{\Delta P}\frac{\beta - \sin(\beta)\cos(\beta)}{2} + r_p * (1 - \cos(\beta)) \right) \tag{A.9}$$

This can be further simplified to:

$$M_{\Delta P} = \Delta P * R_{\Delta P}^2 d\theta * \left(\frac{R_{\Delta P}\beta}{2} - \frac{R_{\Delta P} * \sin(2\beta)}{4} + r_p * (1 - \cos(\beta)) \right) \tag{A.10}$$

A.3. PURE BENDING

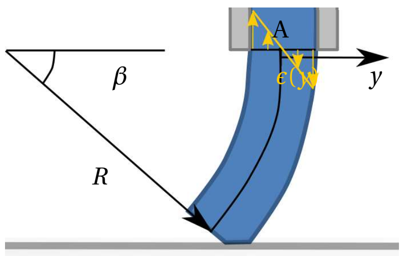

Figure A.3: Momentum $M_{c/t}$ with the definitions for: stress, arm and area.

It is assumed that the neutral axis is constant and in the center of the sealing disk. The strain along the thickness can so be related to:

$$\epsilon_{\text{compresive}} = \frac{\text{change in length}}{\text{origonal length}} = \frac{(R - y) * \beta - R * \beta}{R\beta} = \frac{-y}{R} \tag{A.11}$$

By using Hooke's law $\sigma = E\epsilon$ (in which E stand for the E-modulus and ϵ for the strain) the compressive stress can be found.

$$\sigma_{\text{compressive}}(y) = E\frac{-y}{R} \tag{A.12}$$

The stress can be expressed as a moment in point A by:

$$dM = ydF = y\sigma_{\text{compressive}}dA = E\frac{-y^2}{R}dA \tag{A.13}$$

in which M is the moment, E is the elasticity modulus, I is the moment of inertia and R is the radius related to the curvature.

Note that we recognize the moment of inertia as:

$$I = \int y^2 dA \tag{A.14}$$

Finally we recognize the curvature moment relationship as:

$$M = \frac{EI}{R} \tag{A.15}$$

A.4. INTERNAL FORCES

In the case of a sealing disk the moment of inertia around point A can be calculated as:

$$I = \int_0^{t/2} y^2 dy r_p d\theta = \left[\frac{y^3}{3}\right]_0^{-t/2} r_p d\theta = \frac{t^3 r_p d\theta}{24} \tag{A.16}$$

Therefore the momentum in point A becomes:

$$M_{\text{compressive}} = \frac{Et^3 r_p d\theta}{24R} \tag{A.17}$$

The derivation for the tensile momentum is analogous to the above

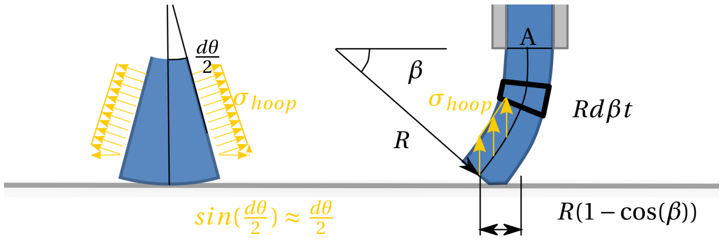

Figure A.4: Moment M_θ with definitions for: stress, arm and area.

Next to the bending, the disk is compressed in the θ direction. This stress is called the hoop stress. Hooke's law in circular coordinates for an axisymmetric geometry can be found in numerous locations (such as [44]). When just the θ and r components are taken the following stress strain relation is obtained:

$$\sigma_\theta = \frac{E}{1-\nu^2}(\epsilon_\theta + \nu\epsilon_r) \tag{A.18}$$

The circumferential strain is

$$\epsilon_\theta = \frac{\text{change in circumference}}{\text{original circumference}} = \frac{2\pi(\beta R + r_p) - 2\pi(R\sin(\beta) + r_p)}{2\pi(\beta R + r_i)} = \frac{\beta - \sin(\beta)}{\beta + r_p/R} \tag{A.19}$$

The opposing forces cancel each other. However the forces in the same direction create a moment around point A. Using $\sin\theta \approx d\theta$ the force becomes:

$$dFd\theta = \frac{E}{1-\nu^2}\frac{\beta - \sin(\beta)}{\beta + r_p/R}dA \tag{A.20}$$

$$dFd\theta = \frac{E}{1-\nu^2}\frac{\beta - \sin(\beta)}{\beta + r_p/R}Rtd\beta d\theta \tag{A.21}$$

$$dM = \frac{Ed\theta}{1-\nu^2}\frac{\beta - \sin(\beta)}{\beta + r_p/R}Rt(1-\cos(\beta))d\beta d\theta \tag{A.22}$$

$$M_\theta = \frac{E d\theta R t}{1-\nu^2} \int_0^{\beta} \frac{\beta - \sin(\beta)}{\beta + r_p/R} (1-\cos(\beta))\, d\beta\, d\theta \tag{A.23}$$

B

Material tests

In this chapter the results of the material tests of a pig sealing disk are given. Firstly a short introduction is given on the hardness tests in Section B.1. Secondly hardness tests are performed to verify whether the hardness is as specified by the manufacturer in Section B.2. The E-modulus is derived from stress-strain tests in Section B.3. With the derived E-modulus conclusions are given on the assumptions made for non-linear materials in Section B.5.

B.1. Material properties

The hardness of a pig sealing disk is typically between 65 and 85 shore type A (S_A). Empirical correlations exist between the shore hardness and E-modulus. The Gent equation reads [43]:

$$E = \frac{0.0981 * (561 + 7.62336 S_A)}{0.137505 * (254 - 2.54 S_A)} \tag{B.1}$$

The British standard reports another empirical relation, namely [53]:

$$S_A = 100\mathrm{erf}(3.186 * 10^{-4} E^{1/2}) \rightarrow E = \left(\frac{\sqrt{\Gamma(S_A/100, 0.5, 1)}}{3.186 * 10^{-4}} \right)^2 \tag{B.2}$$

in which erf() stands for the error function and $\Gamma()$ for the gamma function.

Shore values have a resolution of 5 meaning that a material classified as Shore 75 also could be Shore 72.5 or 77.5. In Table B.1 some typical values for the E-modulus of pigging disks are given.

Table B.1: E-moduli for multiple typical pig shore hardnesses.

Shore hardness A	Gents Equation[MPa] B.1	Giacomin [MPa] B.2
65	4,43	4,30
70	5,52	5,29
75	7,05	6,52
80	9,35	8,09
85	13,18	10,21

The Poisson's ratio of polyurethane is taken as 0.45 as a typical value specified for rubber. Note that it is important to have accurate values for the E-modulus of rubber because the specified correlations can vary +/- 30%.

Rubber is known to behave highly non-linear. Because of the proprietary chemical composition of the polyurethane used by the pig sealing disk manufacturers the material behaviour is unknown. Often the material of a pig sealing disk is classified in shore hardness. The analytical relation between shore hardness and E-modulus assumes a linear behaviour which might be incorrect. Corrections exist, but it is unclear if these are valid for the commercial pig sealing disk used in this experiment. To relate the hardness to the stress-strain results firstly a shore hardness measurement is done and secondly a stress strain test is performed.

B.2. HARDNESS MEASUREMENTS

According to ASTM D2240 hardness measurements are done. The results are shown in Table B.2.

Table B.2: Hardness results for a polyurethane pig.

Sample #	Specified 75 S_a	Specified 85 S_a
1	76	82.8
2	75.7	82.8
3	76.5	83
4	78.3	84.5
5	76.5	83.4
Avg.	76.6	83.3
Std. Deviation	1.01	0.714

The hardness results are within the specification of the manufacturer. Although the measured hardness is a bit higher for the 75 S_a and a bit lower for the 85 S_a. Because the comparison with the stress strain results are general the hardness of each disk will be assumed as specified, meaning that for the 75 S_a disk an E-modulus of 7.05 MPa is expected.

B.3. STRESS STRAIN RESULTS

The stress strain measurements are performed according to ASTM D412. Firstly it was tried to cut small slices from the pig sealing disk with a bench cutter. However because the deformation during cutting was too large this resulted in non-uniform slices. Secondly slices were cut with the help of a water jet and 'dog bones' as specified in ASTM D412 where punched out. In Figure B.1(a) a dog bone is shown before extension. The material is clamped with pneumatic grippers on both sides. In Figure B.1(b) the dog bone is shown under extension.

During testing the extension is recorded against the force on the grippers. The results of nine tests are plotted in Figure B.2.

The ultimate tensile strength before breaking and the elongation the moment of breaking are given in Table B.3.

Table B.3: The tensile strength before breaking and the elongation at breaking for 9 samples of the 75 S_a sealing disk.

Transverse direction	Tensile strength [MPa]	Elongation,at break [%]
nr. 1	25.29	350
nr. 2	19.21	293
nr. 3	27.51	368
nr. 4	19.96	309
nr. 5	19.87	305
nr. 6	23.79	335
nr. 7	21.88	317
nr. 8	27.58	355
nr. 9	17.51	267
AVERAGE	22.5	322
STDEV (n=9)	3.71	32.57

The E-modulus is the derivative of the tensile strength against the strain. The E-modulus as a function of the strain is shown in Figure B.3. It is important to note that the E-modulus as given by the Gent Equation (described in Section B.1) is valid for high strains of +100%. However, from the preliminary calculations it is known that most of a pig sealing disk deforms within roughly 20% strain. The parts which show a higher strain are in the contact areas such as near the edge of the clamping disk or at the contact area with the pipeline wall.

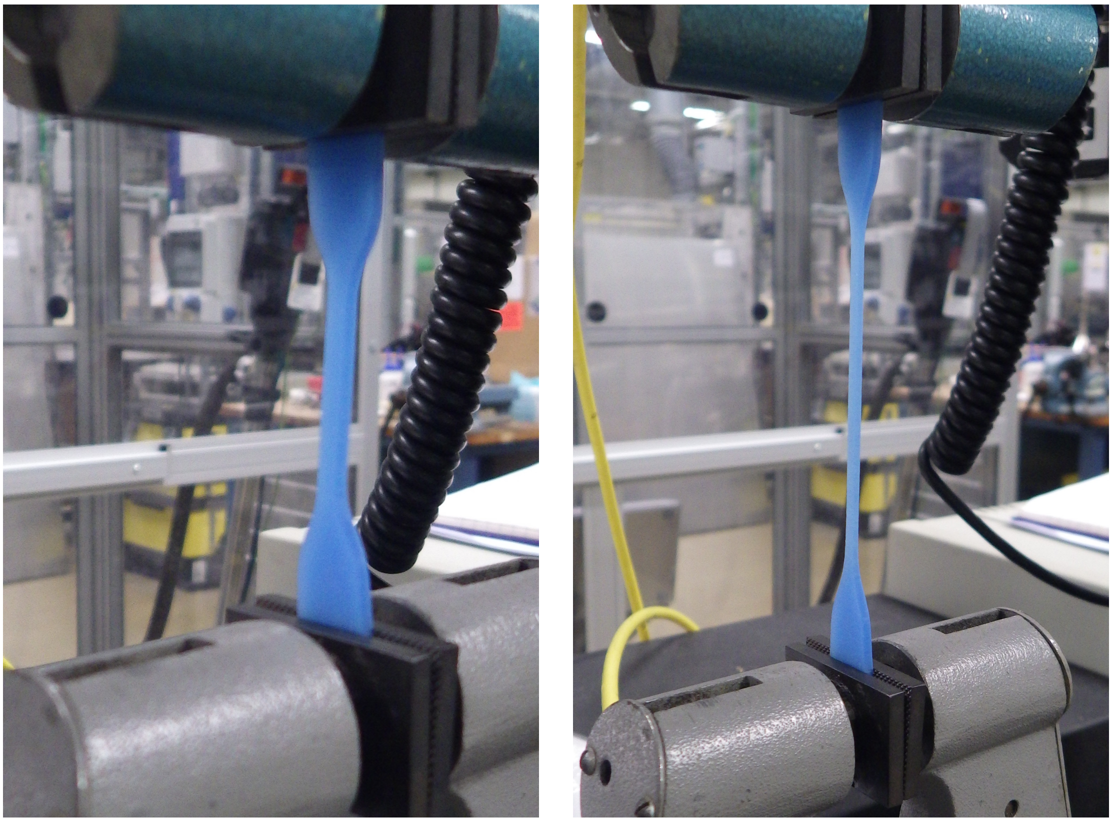

(a) (b)

Figure B.1: (a) A dog bone before tensioning. (b) A dog bone during an extension of roughly 200%. Note that the final extension can become much larger.

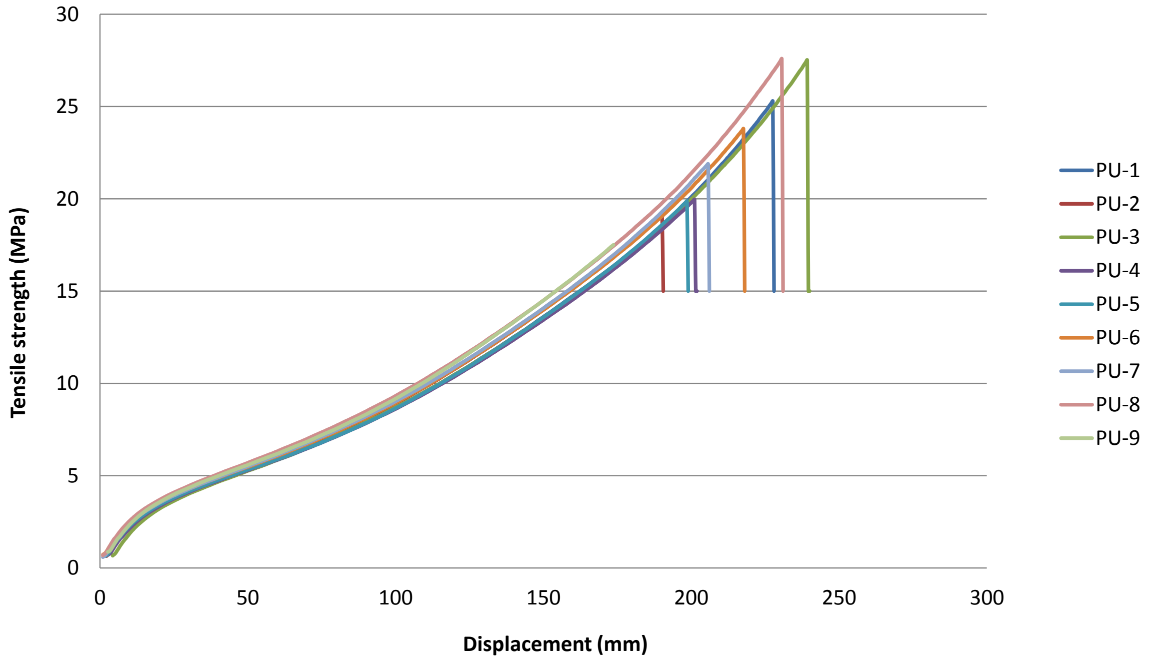

Figure B.2: Stress-strain results of 9 dog bones cutted parallel from a commercial pig sealing disk.

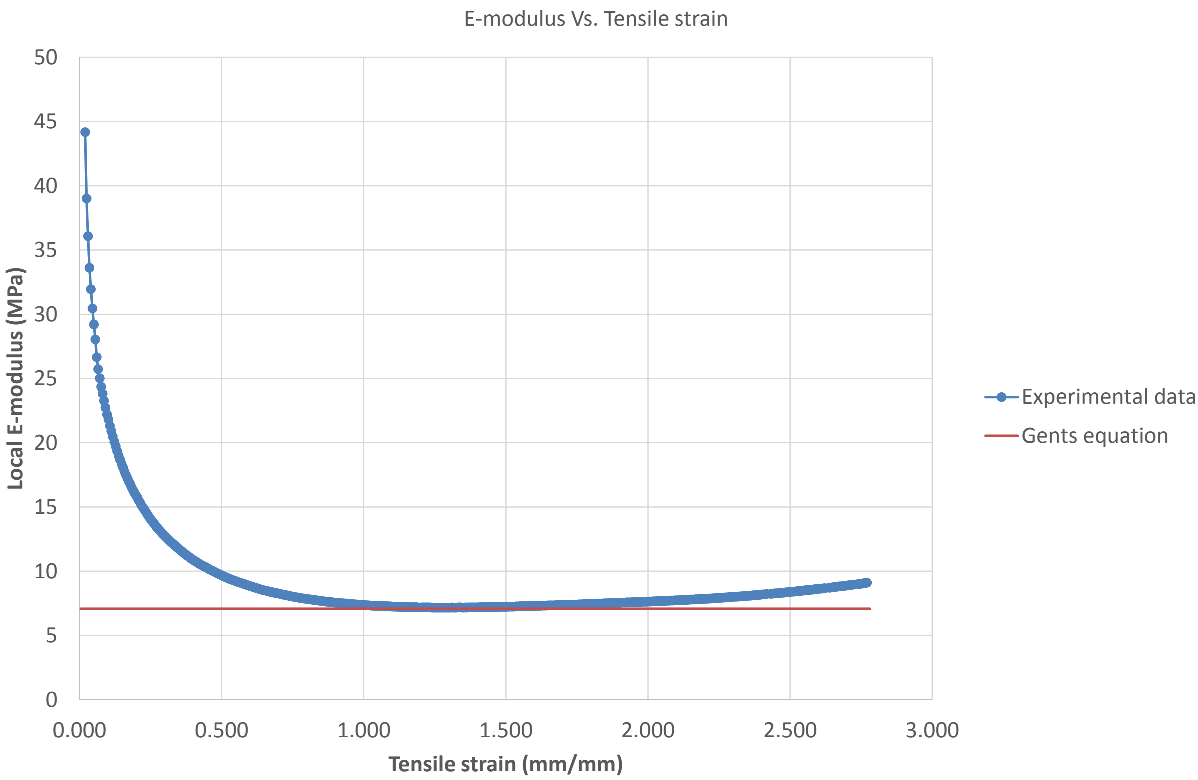

Figure B.3: The E-modulus as a function of the tensile strain. Note that the E-modulus for small strains is much larger than for large strains.

B.4. MATERIAL MODEL

The stress-strain relation for an axisymmetric configuration defined in the (x,θ,z) plane equals:

$$\begin{bmatrix} \sigma_{rr} \\ \sigma_{zz} \\ \sigma_{\theta\theta} \\ \sigma_{rz} \end{bmatrix} = \frac{E}{(1+\nu)(1-2\nu)} \begin{bmatrix} 1-\nu & \nu & \nu & 0 \\ \nu & 1-\nu & \nu & 0 \\ \nu & \nu & 1-\nu & 0 \\ 0 & 0 & 0 & \frac{1-2\nu}{2} \end{bmatrix} \begin{bmatrix} \epsilon_{rr} \\ \epsilon_{zz} \\ \epsilon_{\theta\theta} \\ \gamma_{rz} \end{bmatrix} \tag{B.3}$$

in which ϵ represents the strain, $\gamma = 2\epsilon_{rz}$, ν the Poisson's ratio and sigma stress. When $\nu = 0.5$, E is divided by zero and the solution is singular. To solve this another element formulation can be used (u/p or displacement pressure formulation). Another approach is to use a value for ν close to 0.5 such as 0.499.

B.5. CONCLUSION

Hardness tests were performed to demonstrate that the pig sealing disks perform according to the specifications of the manufacturer. After the stress strain tests it has become clear that the rubber behaves much stiffer than expected for low strains. This implies that the currently used relations largely under predict the E-modulus. With the non-linear material properties new simulations can be carried out and a new more accurate E-modulus that can be used in pig sealing disk applications can be found.

C

MATLAB CODE

C.1. WALL FORCE MODEL

```
rs = 0.1615;
Clamping = 0.5325;
Oversize = 3;
Thickness = 0.015;
c = 0;
mu = 0.3
E = 12.25E+06;
v = 0.45;


rp = Clamping * rs;
r  = rs/(1+Oversize/100);
t = Thickness;
dP = 0;

syms X;
l = rs-rp;                              %[m]

beta = double(vpasolve( (r-rp)-(t*sin(X)/2)+c*sin(X)*cos(X)== l*sin(X)/X,X,pi/2)); %[Radians]
R = l/beta; %[m]

Mc = E*(t^3)*rp/(24*R);      %[N.m]
Mt = E*(t^3)*rp/(24*R);      %[N.m]
Mp = dP*R^2 * (R*beta/2 - R*sin(2*beta)/4 +rp - rp*cos(beta));          %[N.m]

fun = @(alpha) (alpha-sin(alpha)).*(1-cos(alpha))./(alpha + rp/R);
e_theta = integral(fun,0,beta,'arrayValued',true);                      %Strain[-]
Mh = (E*R^2*t)/(1-v^2) * e_theta;                                       %[N.m]

Mext = Mc + Mt + Mp + Mh ;                                              %[N.m]
Fwall = Mext/(mu *r*(r-rp) + r*(R*(1-cos(beta))-t*cos(beta)/2));        %[N/m]
Ffric = mu* Fwall;                                                      %[N/m]

Mf = mu * Fwall *r*(r-rp);                        %[N.m]
Mw = Fwall*r*(R*(1-cos(beta))-t*cos(beta)/2);     %[N.m]
```

C.2. EHL MODEL BY ITERATION

C.2.1. MAIN

```
clc
close all
clear all



%% Define input
rs = 0.1615 ;    Clamping = 0.5325;   Oversize = 1;    Thickness = 0.015; c = 0.001;
mu = 0.9;   E = 12.25E+06;   v = 0.45; NDiscs = 4;    MU_DRY = 0.9
rp = Clamping * rs; r   = rs/(1+Oversize/100);    t = Thickness;   dP = 0;
KS = 0.0115;     SIGS_ = 6.7*10^-6;   P1=dP;   PN = 0; VP = -1    ;    ETA = 0.001;
RELAX = 100; crit = 1; guess = 0.5*SIGS_;
%alsodo qrt 10 and sqrt 0.1

number = 80
Tel = (1:2:number)
T=1
for T = 1:number

    refin = Tel(T)

X1n = (1*refin)+1;
X2n = 2*refin;
X3n = 2*refin;
X4n = 1*refin;
X5n = 2*refin;
X6n = 2*refin;
X7n = 1*refin;
NNodes = X1n+X2n+X3n+X4n+X5n+X6n+X7n;

WallForce
Mesh2


Solve


Convergence(T).X = x;
Convergence(T).H = H_;
Convergence(T).HO = HO_;
Convergence(T).hmax = max(H_ - HO_)/SIGS_;
Convergence(T).NNodes = NNodes;
end


figure;
hold on
for i=1:4:T-1
    a(i) = plot(Convergence(i).X,Convergence(i).H-Convergence(i).HO,'.-')
end
xlabel('x-position␣[m]')
ylabel('deformation␣h-h_o-\delta_o␣[m]')
```

```
set(gcf,'paperpositionmode','auto')
print(gcf,'-depsc2','-loose','Solution_for_H_HO.eps');

figure
a= loglog((cell2mat({Convergence(1:end-1).NNodes})),((cell2mat({Convergence(1:end-1).hmax}))-2.6005)./
hold on
b= loglog((cell2mat({Convergence(1:end-1).NNodes})),100*(cell2mat({Convergence(1:end-1).NNodes})).^-1,
legend([a, b], {'Relative error h', 'first order convergence'})
xlabel('Amount of Nodes #')
ylabel('Relative error [-]')

set(gcf,'paperpositionmode','auto')
print(gcf,'-depsc2','-loose','Relative_error.eps');

% %Postproc
```

C.2.2. Solve

```
j=1;
conv1(1)=crit+1;
conv2(1)=crit+1;
%% solve EHL

while abs(max(conv1))>crit;
    j=j+1;

    if mod(j,1000) == 0
        sum(conv1)
        plot(x,conv1,'+')
        drawnow
    end


     H2_(i)= H_(i) + (PF1(i)+PA(i)-PT(i))*(1-v^2)*A_./(1.013*E*RELAX);

     %H2_(find(H2_<0.4*SIGS_)) = 0.4*SIGS_;
%       disp('Negative height values are being cut off')

    while sum((H2_(i) <= 0)) > 1
        Mesh2
        RELAX = RELAX * 2
        H2_(i)= H_(i) + (PF1(i)+PA(i)-PT(i))*(1-v^2)*A_./(1.013*E*RELAX);
    end

     H_(i) =H2_(i);

     PT(i)= 1.013 * E * ((H_(i)-HO_(i)))/((1-v^2)*A_);
     PA(i)= 0.707 * E * KS*exp(-(H_(i)/SIGS_))/(1-v^2);
     conv2(i) = abs(PF1(i)+PA(i)-PT(i));

    PF1=FDSCHEME_diffmesh_ND(x,H_,ETA,VP,P1,PN);
    %PF1=FDSCHEME(x,H_,ETA,VP,P1,PN);

    conv1(i) = abs(PF1(i)+PA(i)-PT(i));
    conv2 = conv1;
end
```

C.2.3. FDSCHEME

```
function [ PF1 ] = FDSCHEME_diffmesh_ND( x,h,ETA,U,P1,PN )
%UNTITLED Summary of this function goes here
%   Detailed explanation goes here

X = max(x) - min(x);
C = (max(h) - min(h))/2;

xb = x/X;
hb = h/C;

for i=1:length(xb)-2;
    for j=1:length(xb)-2;
        if i==j
            M(i,j)= (xb(i+1)-xb(i))*hb(i+1).^3 + (xb(i+2)-xb(i+1))*hb(i).^3;
        elseif i==j+1
            M(i,j)=  -(xb(i+2)-xb(i+1))*hb(i)^3;
        elseif i==j-1
            M(i,j)=  -(xb(i+1)-xb(i))*hb(i+1)^3;
        end
    end
end

for i=1:length(xb)-2
    RHS(i)=-(hb(i+2)-hb(i+1))*(xb(i+1)-xb(i)).^2;
end

Pb1 = P1* C^2 / (6 * ETA * U);
Pbn = PN* C^2 / (6 * ETA * U);


RHS(1) = RHS(1) + Pb1*(x(3)-x(2))*hb(1)^3;
RHS(length(RHS)) = RHS(length(RHS))+ Pbn*(xb(end)-xb(end-1))*hb(i+1)^3;
Pb = M\RHS';

PF1 =[P1 Pb' * 6 * ETA * U / C^2 PN];
end
```

D

DERIVATION CONTACT MECHANICS EQUATIONS

In this appendix the derivations of the equations related to the contact mechanics equations are given. First a brief analytical derivation is done to derive an expression for the contact problem. This formula is validated with finite element calculations afterwards. After this is done a brief derivation is given of the Greenwood-Williamson model. This serves the purpose of giving the enthusiastic reader a general insight in the working principles of this model.

D.1. ANALYTICAL DERIVATION OF CONTACT MODEL BASED ON WINKLER SPRINGS

The difficulty of contact mechanics (or linear elasticity in general) is that the deformation in any point depends upon the load on all points. This gives rise to complex equations which typically can only be solved by numerical techniques. Johnson [31] states that this can be avoided if the contact can be modelled by Winkler elastic foundation theory. In the case described here we make use of the linear relationship as described by Hertz between indentation depth and force. First the kinematics of the cylinders will be discussed. Secondly the constitutive equations as given by Winkler and how they relate to Hertz.

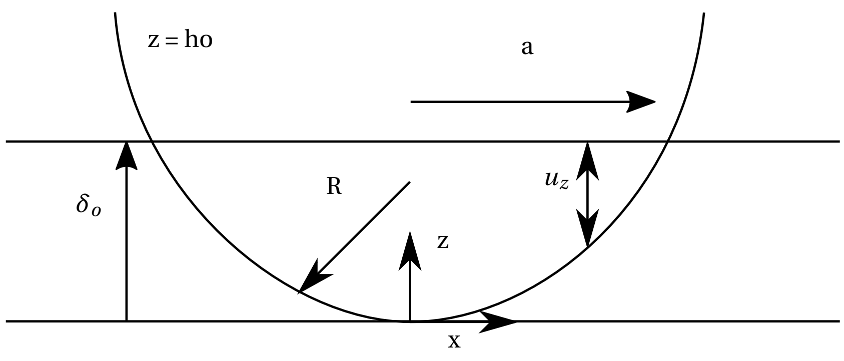

Figure D.1: The parameter δ_o equals the initial indentation to carry the load F_{wall}. The geometry of the disk is described by a function h_o. The chamfer length equals c. The amount of deformed material can be described by three terms: $m\delta_o^2/2$, $\delta_o * c$, and $\delta_o^2/(2*m)$.

The curved surfaces are approached by a polynomial of the shape

$$z_1 = A_1 x^2 + B_1 y^2 + C_1 xy + ... \tag{D.1}$$

Since the curvature is equal to the second derivative it can be shown that for a cylinder with radius R the value of A_1 equals $A_1 = (1/2R_1)$. In the case of two parallel surfaces the distance between both is given by:

$$z(x) = z_1 + z_2 \tag{D.2}$$

Therefore, the radii of both cylinders can be rewritten to one by $R = 1/R_1 + 1/R_2$. Note that for a cylinder on a flat surface this reduces to $R = R_1$. To describe the original height profile (h_o) between both cylinders we write:

$$h_o(x) = z(x) = \frac{x^2}{2R} \tag{D.3}$$

When the two cylinders are pressed onto each other they will deform. The elastic displacements (u_z) as a function of the penetration at the origin (δ_o) can be written as:

$$u_z(x) = \begin{cases} \delta_o - z(x), & \delta > z \\ 0, & \delta_o \le z \end{cases} \tag{D.4}$$

Since the deformation becomes zero near the edges, z should be equal to δ_o at those points. Now a direct relation between the penetration at origin and the contact length (a) can be found:

$$\delta_o = h_o(a) = \frac{a^2}{2R_1} \rightarrow a = \sqrt{\delta_o 2R_1} \tag{D.5}$$

To conclude a kinematic model has been made with radius R and original indentation δ_o as input parameters and the contact length (a) and displacement (u_z) as output. To do this equation D.5 and D.4 are used. Now Winkler spring model is used to relate this displacement to an applied force.

Winkler elastic foundation theory basically writes that the local pressure as a function of the displacement can be written as:

$$P(x) = K * u_z \tag{D.6}$$

In which K is a value for the stiffness of the two surfaces.

To simplify the derivation of the contact pressure equation a new constant is defined as:$K = \frac{K_2}{a}$. With the constant K_2 the Winkler foundation equation is re-written as:

$$P(x)_{\text{contact}} = \frac{K_2}{a}\left(\delta_o - \frac{x^2}{2R}\right) \tag{D.7}$$

The maximum pressure at the centre is:

$$P_{\text{max, pressure}} = \frac{K_2}{a}(\delta_o) \tag{D.8}$$

To compare the maximum pressure and the contact length the equations have to be expressed as a function of the load per meter or F_{wall}. To obtain the load the contact pressure is integrated over the contact length:

$$\begin{aligned} F_{\text{wall}} = \int_{a^-}^{a^+} P(x)dx = \quad & \frac{K_2}{a} 2 \int_0^a \left(\delta_o - \frac{x^2}{2R}\right) dx \\ & \frac{2K_2}{a}\left[\delta_o a - \frac{a^3}{6R}\right] \\ & \frac{2K_2}{a}\left[\frac{a^3}{2R} - \frac{a^3}{6R}\right] \\ F_{\text{wall}} = \frac{2K_2 a^2}{3R} = \quad & \frac{4K_2\delta_o}{3} \end{aligned} \tag{D.9}$$

Now the contact length is rewritten as:

$$a = \sqrt{\frac{3RF_{\text{wall}}}{2K_2}} \tag{D.10}$$

and if Equation D.9 is substituted into Equation D.8 the maximum pressure is found as:

$$P_{\text{max, pressure}} = \frac{3F_{\text{wall}}}{4K_2}\sqrt{\frac{2K_2}{3RF_{\text{wall}}}} = \sqrt{\frac{3F_{\text{wall}}K_2}{8R}} \tag{D.11}$$

Now the maximum pressure and foot length are known, but K_2 must still be determined. To do this the solution is compared with the solutions of Hertz. First the Hertzian assumptions are restated:

The following assumptions are done in determining the solutions of the Hertzian contact problems:

1. The strains are small and within the elastic limit.
2. The surfaces are continuous and non-conforming (implying that the area of contact is much smaller than the characteristic dimensions of the contacting bodies).
3. Each body can be considered an elastic half-space.
4. The surfaces experience no friction.

The Hertzian contact length for an cylindrical contact is given by Johnson [31] by EquationD.12. Johnson uses here the plane stress E-modulus is used, which is defined as $E^* = E/(1-\nu^2)$.

$$a_{\text{Hertz cylinder}} = \sqrt{\frac{4F_{\text{wall}}R}{\pi E*}} \tag{D.12}$$

The Hertzian maximum pressure for a cylindrical contact is given by:

$$P_{\text{max,Hertz cylinder}} = \sqrt{\frac{F_{\text{wall}}E^*}{\pi R}} \tag{D.13}$$

When comparing the contact length with the solution of Hertz K_2 is found to be:

$$K_2 = \frac{3\pi}{8} = 1.178E^* \tag{D.14}$$

When comparing the maximum pressure with the solution of Hertz K_2 is found to be:

$$K_2 = \frac{8}{3\pi} = 0.848E^* \tag{D.15}$$

To obtain an average between the two values of K_2 an average is used. Therefore, we write

$$K_2 = 1.013E^* \tag{D.16}$$

Concluding, a model is made with the local pressure $P(x)$ as the output value. The local deformation (u_z) and the plain strain E-modulus (E^*) are the input parameters. Note that this model can be extended to any geometry for which the local deformation is known. The actual local pressure will of course deviate more and more as the geometry will differ from a cylinder.

D.2. VALIDATION OF CONTACT MODEL

In this section the analytically derived equations are validated with a finite element calculation. First the Hertzian contact equation for two cylinders is calculated with Femap. The results from the analytical equations are compared with the results from Femap. Secondly the results from the equations obtained by the Winkler foundation theory are compared to FEM.

The foot length and maximum pressure are given by Equation D.12 and Equation D.13. In these equations E^* and R are the effective E-modulus and radius, respectively defined as:

$$\frac{1}{E^*} = \frac{1-\nu_1^2}{E_1} + \frac{1-\nu_2^2}{E_2} \tag{D.17}$$

$$\frac{1}{R} = \frac{1}{R_1} + \frac{1}{R_2} \tag{D.18}$$

In Figure D.2 the mesh is shown with the deformation and with the plate id Von Mises stress in MPa. The two (half) cylinders have a radius of 2 m and a length of 1 m. Linear plane strain elements are used to make the mesh and the contact is modelled with slide line elements which make use of the penalty method. The

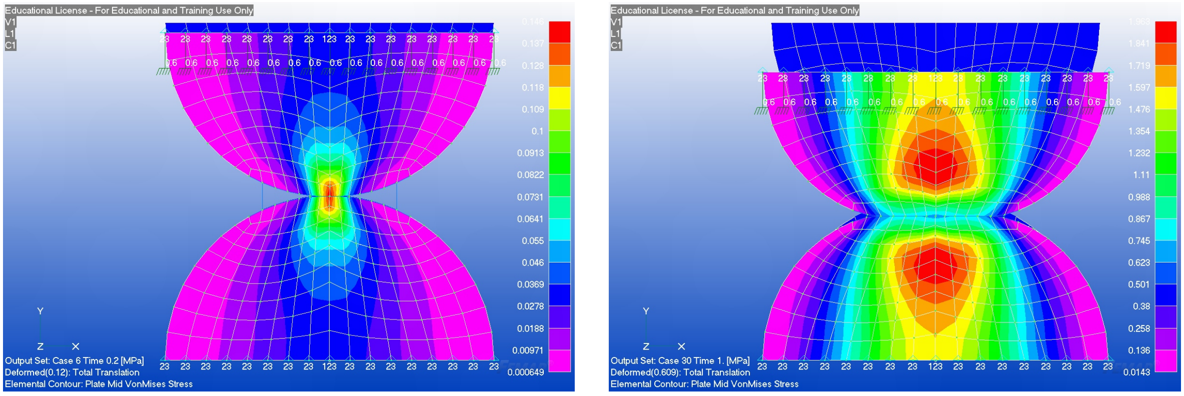

(a) (b)

Figure D.2: The Hertzian contact problem with two cylinders with an E-modulus of 12.25 MPa and a Poisson's ratio of $\nu = 0.45$. The cylinders have a radius of 2 m and a indentation of 0.02 m (a) to 0.5 m (b). The plate mid Von Mises stress is plotted in the contour in MPa.

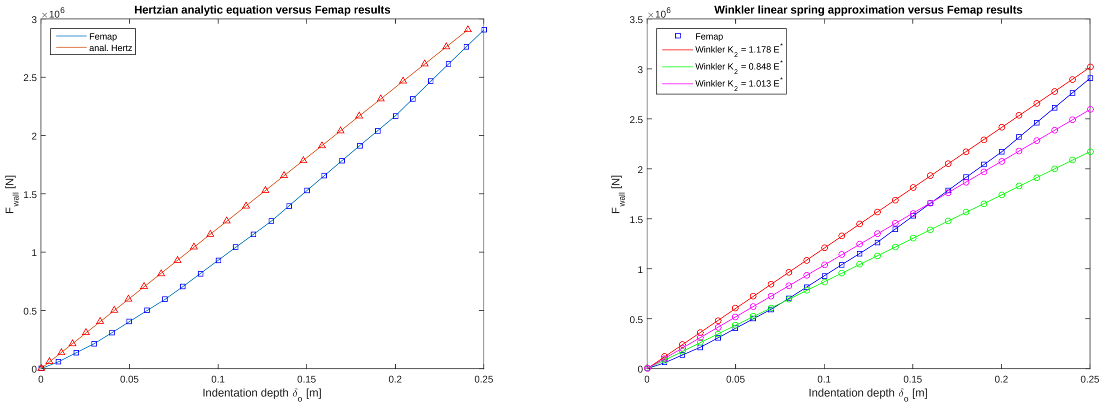

(a) (b)

Figure D.3: (a) The force F_{wall} necessary to create a certain indentation. As can be seen the analytical solution is in agreement with the results from the finite element model. (b) The Winkler spring approximation compared with the finite element results. Using an approach which is partially matched to the maximum pressure and partially matched to the foothlength provides a result in agreement with the finite element calculations.

elements are defined by a linear material model with an E-modulus of 12.25 and a Poisson's ratio of 0.45 for both cylinders. The load of the upper cylinder is defined by a forced displacement of the upper nodes in the vertical direction. Thereby allowing widening of the mesh. One node in the center of the base of each cylinder is fixated in the horizontal direction. The problem is solved by the non-linear static solver (106).

The indentation is applied by the displacement. By adding the constraint forces for all the constraint nodes F_{wall} is calculated. The results from Femap are compared with the analytical results in Figure D.3.

Overall it can be stated that the balance between an accurate footprint and an accurate maximum pressure is valid when compared to the finite element model.

D.3. DERIVATION GREENWOOD-WILIAMSON MODEL

In the following section a short derivation of the Greenwood-Wiliamson asperity model is given [35].

If two surfaces come together until their reference planes are separated by a distance d there will be contact at any asperity which height is larger than d. The asperity height can be described by z, which will be a stochastic function described by function ϕ. It can be shown that the probability of making contact at any given asperity of height z now is:

$$prob(z > d) = \int_{d}^{\infty} \phi(z)dz \tag{D.19}$$

In the Greenwood-Wiliamson model asperities are modelled as spheres (at least near the contact surface). A sketch of the Greenwood-Wiliamson model compared to the actual situation is given in Figure D.4.

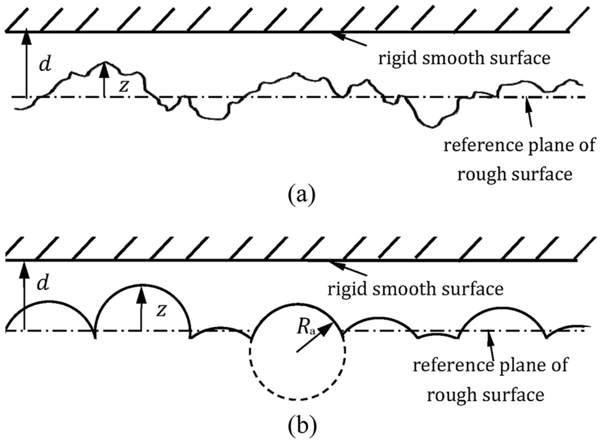

Figure D.4: A definition sketch of the working principle of the Greenwood-Wiliamson model [13].

All asperities are assumed to be spheres with the same curvature R_a. If an asperity exceeds the separation height $h(x)$ it will be compressed a distance $\omega = z - h$, in which ω is called the compliance. Because of the compression of the sphere a small flat circular disk appears from which the radius and area can be derived.

The required force to compress the asperities may be written as $F = g(\omega)$ where the function $g(\omega)$ depends on the material properties. If the deformation is entirely within the elastic limit the Hertz equations for an axisymmetric point contact can be used to find

$$g(\omega) = F = \frac{4}{3}E^* \sqrt{R_a \omega^3} \tag{D.20}$$

for single compliant interaction, such as soft-hard rubber-steel contact. Here E^* is the plane strain E-modulus of the soft material, defined as $E^* = E/(1 - \nu^2)$.

Similar it is found that the expected load is

$$P = N_a \int_{h}^{\infty} g(\omega)\phi(z)dz = N_a \int_{h}^{\infty} \frac{4}{3}E^* \sqrt{R_a (z-h)^3}\phi(z)dz \tag{D.21}$$

in which N_a is the asperity density defined as the number of asperities divided by the area.

An often used stochastic function to describe the wall height of a surface is the negative exponential distribution, which is given by Equation D.22.

$$\phi(z) = \frac{1}{\sigma_a \sqrt{2\pi}} e^{-\frac{z}{\sigma_a}} \tag{D.22}$$

The pressure then becomes:

$$P = N_a \frac{4}{3} E^* R_a^{1/2} \frac{1}{\sigma_a \sqrt{2\pi}} \int_{h}^{\infty} (z-h)^{3/2} e^{-\frac{z}{\sigma_a}} dz \tag{D.23}$$

This integral is evaluated :

$$
\begin{aligned}
I =& \int_h^{\infty} (z-h)^{3/2} e^{-\frac{z}{\sigma_a}} dz \\
=& \int_h^{\infty} (z-h)^{n-1} e^{-\frac{z}{\sigma_a}} dz && n = 2.5 \\
=& \int_h^{\infty} (u)^{n-1} e^{-\frac{u+h}{\sigma_a}} du && \text{substitution u = z-h} \\
=& \sigma_a^n e^{-h/\sigma_a} \int_h^{\infty} \left(\frac{u}{\sigma_a}\right)^{n-1} e^{-\frac{u}{\sigma_a}} d\left(\frac{u}{\sigma_a}\right) && \text{substitution } du = \sigma_a d(u/\sigma_a) \\
=& \sigma_a^n e^{-h/\sigma_a} \Gamma(n) && \text{substitution with gamma function}
\end{aligned}
\tag{D.24}
$$

The incomplete gamma function is recognized as:

$$
\Gamma(n,x) = \int_x^{\infty} t^{n-1} e^{-t} dt \tag{D.25}
$$

The pressure then becomes:

$$
F = N_a \frac{4}{3} E^* R_a^{1/2} \frac{\sigma_a^{2.5}}{\sigma_a \sqrt{2\pi}} e^{-h/\sigma_a} \Gamma(n) \tag{D.26}
$$

The incomplete gamma function for $x << 1$ gives $\Gamma(2.5, 0) = 3/4\sqrt{\pi} = 1.33$. Collecting all other constants gives $\frac{4}{3}\frac{1}{\sqrt{2\pi}} * 3/4\sqrt{\pi} = \frac{1}{\sqrt{2}} = 0.707$. The values N_a, R_a and $\sigma_a^{3/2}$ form a dimensionless number which will be called K_s. In the references [6] [31] the value of K_s is varied to match experimental results.

E

Derivation lubrication equation

E.1. Discretization and coupling

To obtain the lubrication equation for a planar slider we start with Reynolds equation for an incompressible lubricant:

$$\frac{\partial}{\partial x}\left(\frac{h^3}{12\eta}\frac{\partial P}{\partial x}\right)+\frac{\partial}{\partial z}\left(\frac{h^3}{12\eta}\frac{\partial P}{\partial z}\right)=\frac{1}{2}\frac{\partial}{\partial x}(u_2-u_1)+(V_h-V_0)+\frac{\partial}{\partial z}(W_2-W_1)h \tag{E.1}$$

We assume: no squeeze (velocity in the h direction), planar so that there are no velocities in any other direction than x, the pipeline wall velocity equals 0 and the fluid velocity at the pig equals u_{pig}:

$$\frac{\partial}{\partial x}\left(h^3\frac{\partial P_f}{\partial x}\right)=6\eta u_{\text{pig}}\frac{\partial h}{\partial x} \tag{E.2}$$

Note that in the above equation h is the fluid film height, x is the length direction, u_{pig} is the velocity of the pig and η is the fluid viscosity.

Equation E.2 is valid under the following assumptions:

- Inertial terms are neglible
- Pressure gradient over h is neglible
- The liquid behaves as a Newtonian fluid
- No slip at both boundary conditions
- Incompressible flow
- Both the fluid velocity and the pig velocity are in the same direction
- The film height velocity (($V_h - V_0 = \partial h/\partial t$) can be neglected

To enable calculating the film pressure for any film height the above equation is normalized, discretized and solved numerically. First we write:

$$\frac{\partial}{\partial \bar{x}}\left(\bar{h}^3\frac{\partial \bar{p}}{\partial \bar{x}}\right)=\frac{\partial \bar{h}}{\partial \bar{x}} \tag{E.3}$$

in which $\bar{x}=x/X$, $\bar{h}=h/C$ and $\bar{p}=P*C^2/6\eta u_{\text{pig}}$. Here X is the length of the problem and C is the average film height. This equations is discretized as:

$$\frac{\bar{h}_i^3\frac{\bar{p}_{i+1}-\bar{p}_i}{\bar{x}_{i+1}-\bar{x}_i}-\bar{h}_{i-1}^3\frac{\bar{p}_i-\bar{p}_{i-1}}{\bar{x}_i-\bar{x}_{i-1}}}{x_i-x_{i-1}}=\frac{h_{i+1}-h_i}{x_{i+1}-x_i} \tag{E.4}$$

which can be solved by simple iteration as :

$$\bar{p}_i = \frac{A + B\bar{p}_{i+1} + C\bar{p}_{i-1}}{D} \tag{E.5}$$

with:

$$\begin{aligned} A &= (\bar{h}_{i+1} - \bar{h}_i) * \Delta x_1^2 && \text{(E.6)} \\ B &= \bar{h}_i^3 \Delta x_1 && \text{(E.7)} \\ C &= \bar{h}_{i-1}^3 \Delta x_2 && \text{(E.8)} \\ D &= \Delta x_1 \bar{h}_1^3 + \bar{h}_{i-1}^3 \Delta x_2 && \text{(E.9)} \\ & && \text{(E.10)} \end{aligned}$$

in which $\Delta x_1 = \bar{x}_i - \bar{x}_{i-1}$ and $\Delta x_2 = \bar{x}_{i+1} - \bar{x}_i$. Note that to solve the above equations, the pressure at the start and end of the problem are used as boundary conditions.

E.2. VALIDATION OF THE LINEAR INCLINATION

In this section the numerical solution is compared with an analytical solution for a linear inclination.

By integrating Equation E.2 the following expression is found:

$$\frac{dP_f(x)}{dx} = 6u_{\text{pig}}\eta \frac{h - C_1}{h^3} + C_2 \tag{E.11}$$

It is assumed that the boundary condition on both sides are:

$$P_f(x = 0) = 0 \tag{E.12}$$
$$P_f(x = L) = 0 \tag{E.13}$$

$$0 = \int_L^0 \frac{h - h_c}{h^3} dx \tag{E.14}$$
$$h_c = \frac{\int_0^L \frac{1}{h^2} dx}{\int_0^L \frac{1}{h^3} dx} \tag{E.15}$$

The height profile is given by:

$$h(x) = h1 - \frac{h1 - h0}{L} x \tag{E.16}$$

This is evaluated to obtain:

$$\frac{h_c}{h_0} = \frac{2n}{n-1} \tag{E.17}$$
$$n = \frac{h_1}{h0} \tag{E.18}$$

The length x is non-dimensionalized with $\bar{x} = x/L$

$$\frac{\eta * u_{\text{pig}} * L}{h0^2} * \frac{6 * (n-1) * (1-\bar{x}). * \bar{x}}{(n+1) * (n - \bar{x} * n + \bar{x})^2} \tag{E.19}$$

The comparison between the numerical solution and the analytical solution is shown in Figure E.1. The values used are: L = 1, h0 = 1e-3, h1 = 2e-3,U = 5, η = 1e-3 and 100 nodes are used. The numerical solution is in very good agreement with the analytical solution.

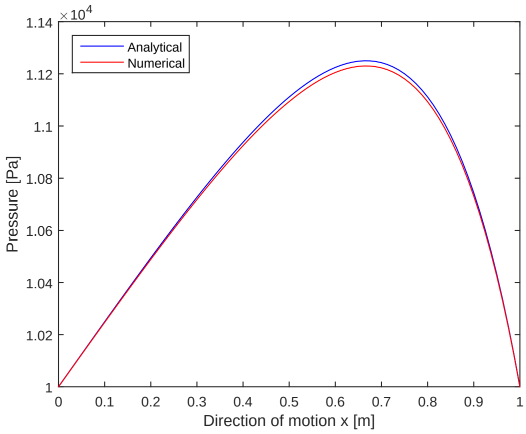

Figure E.1: Solution for the pressure for a converging wedge.

F

Measurement results

F.1. BAKER HUGHES 15 MM

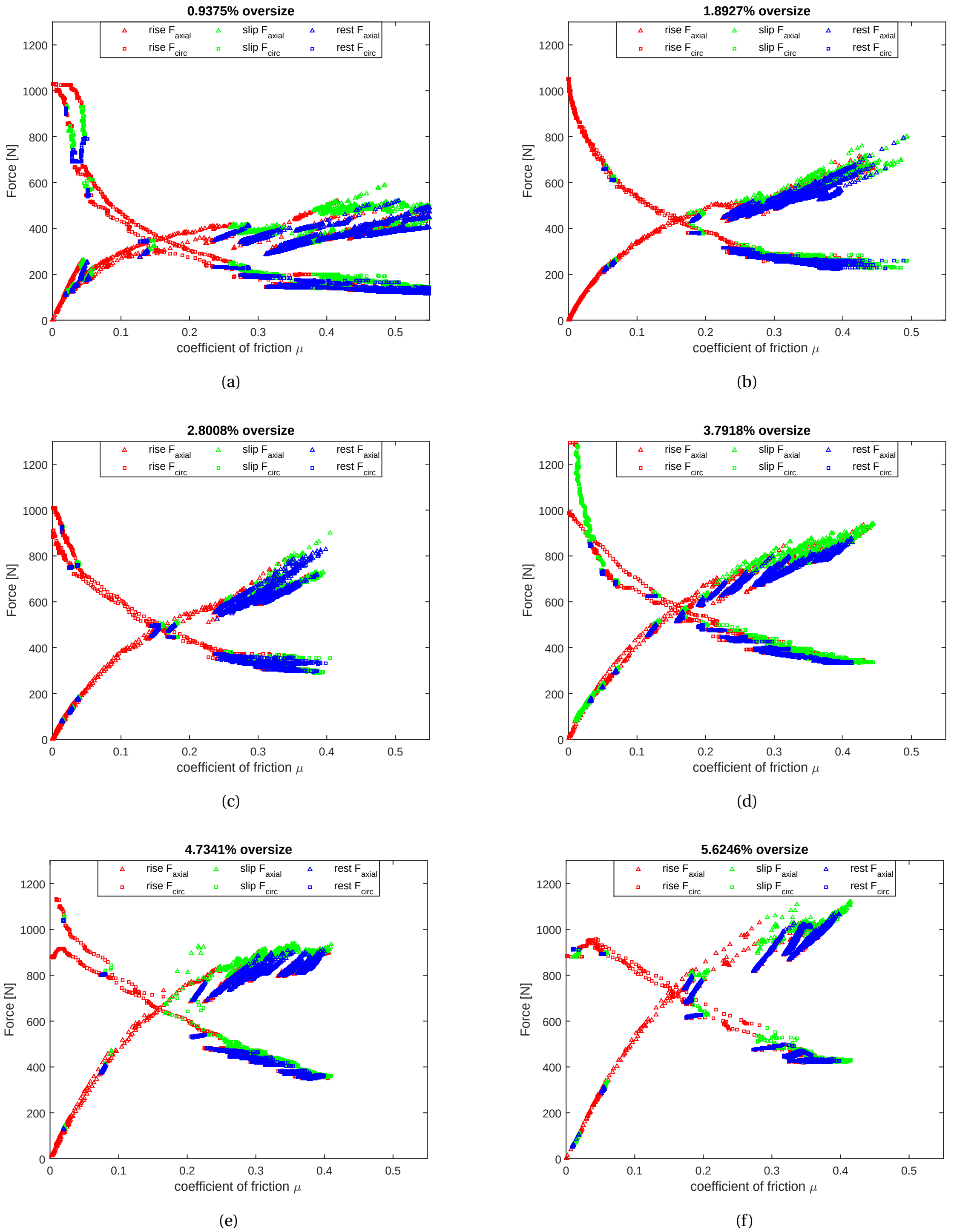

Figure F.1: Forces F_{axial} (△) and F_{circ} (□) are shown as a function of the coefficient of friction. Each figure shows two independent measurements, thereby confirming repeatability. In this figure all data points are shown and the rise, slip and rest data points are distinguished by using different colours. During rise the coefficient of friction increases and the disk is in static equilibrium. During slip the disk slips and a green noisy signal is shown. While resting the disk slowly relaxes and the coefficient of friction decreases. During creep F_{axial} decreases and F_{circ} increases.

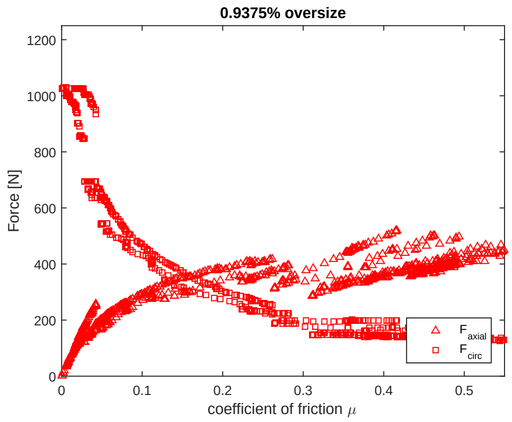

(a)

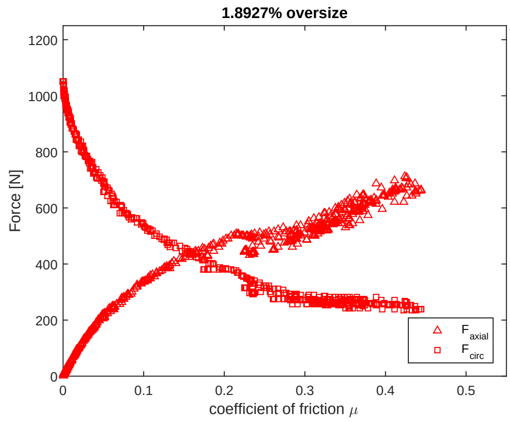

(b)

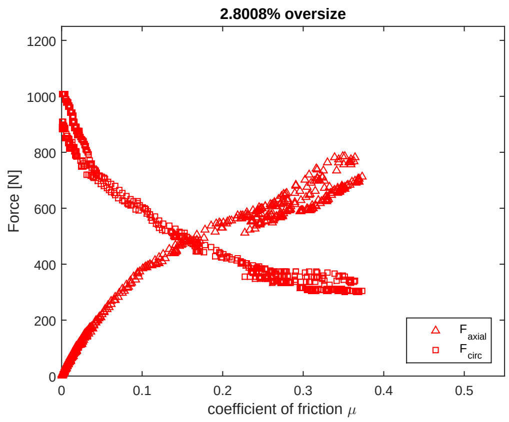

(c)

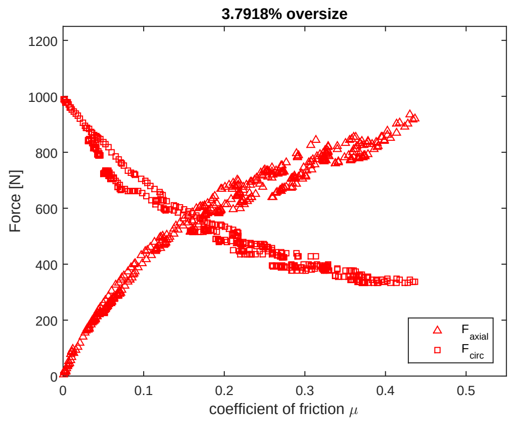

(d)

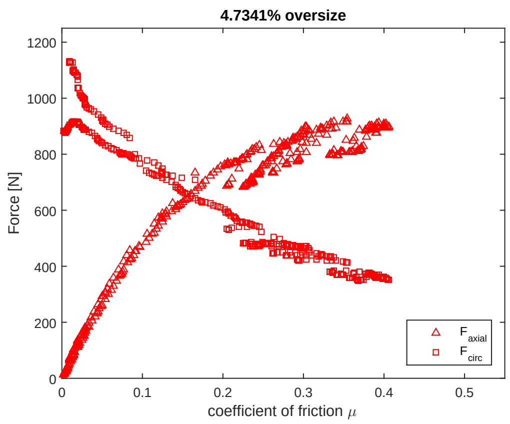

(e)

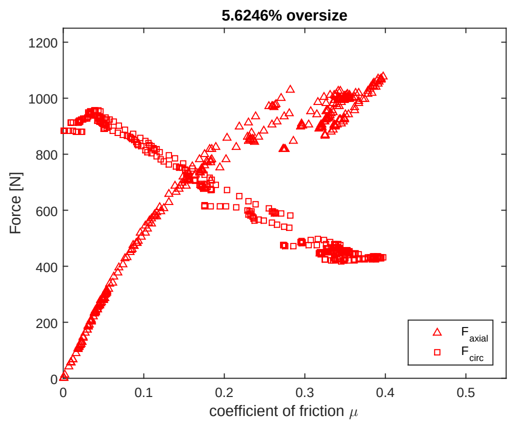

(f)

Figure F.2: Forces F_{axial} ($\triangle$) and F_{circ} ($\square$) are shown as a function of the coefficient of friction. In each figure two separate measurements are shown. In this figure only the slip data points are shown.

F.2. ROSEN 75 SHORE 15 MM

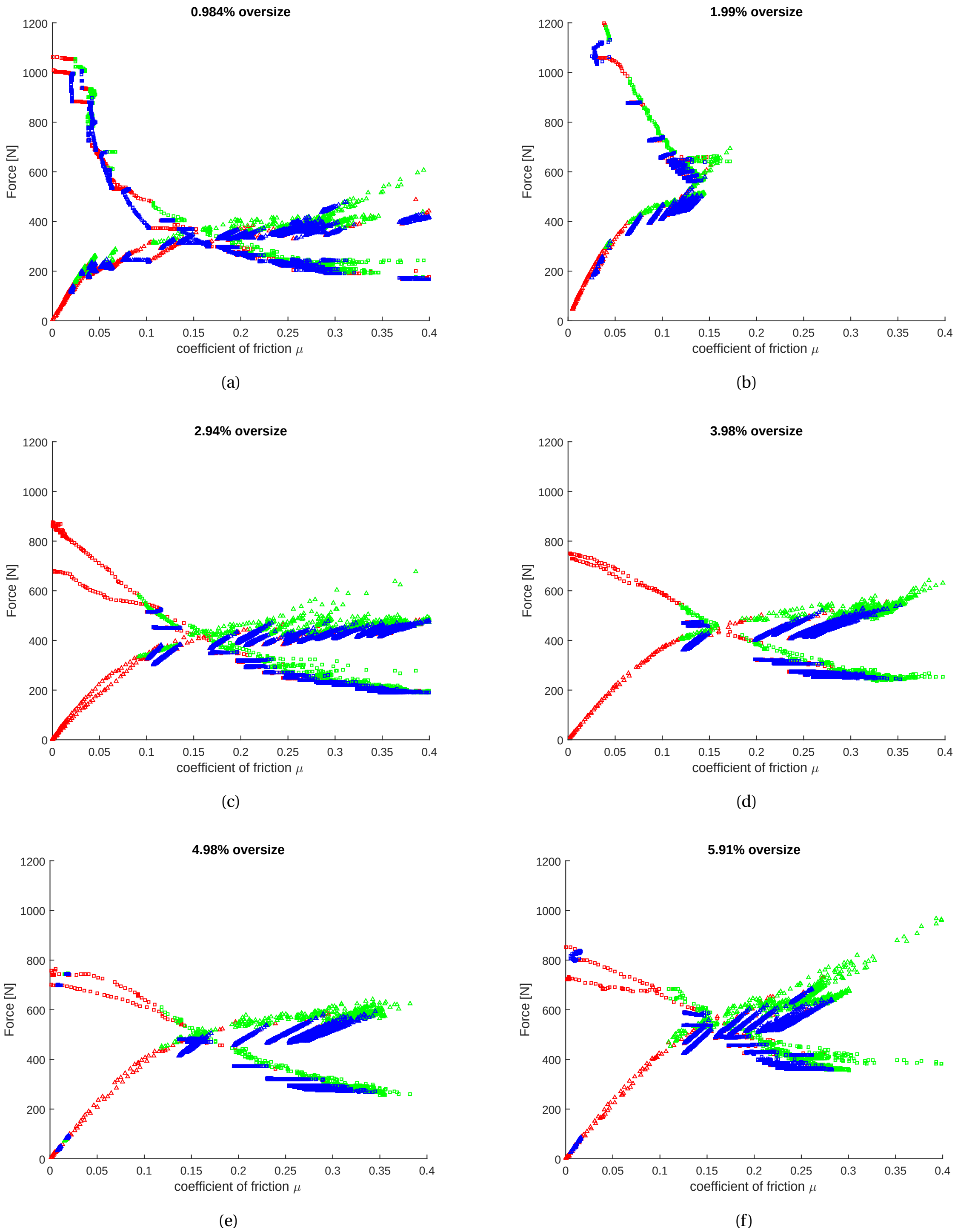

Figure F.3: Forces F_{axial} (△) and F_{circ} (□) are shown as a function of the coefficient of friction for the 15 mm Rosen disk. Each figure shows two independent measurements, thereby confirming repeatability. In this figure all data points are shown and the rise, slip and rest data points are distinguished by using different colours. During rise (red) the coefficient of friction increases and the disk is in static equilibrium. During slip (green) the disk slips and a noisy signal is shown. While resting (blue) the disk slowly relaxes and the coefficient of friction decreases. While resting F_{axial} decreases and F_{circ} increases.

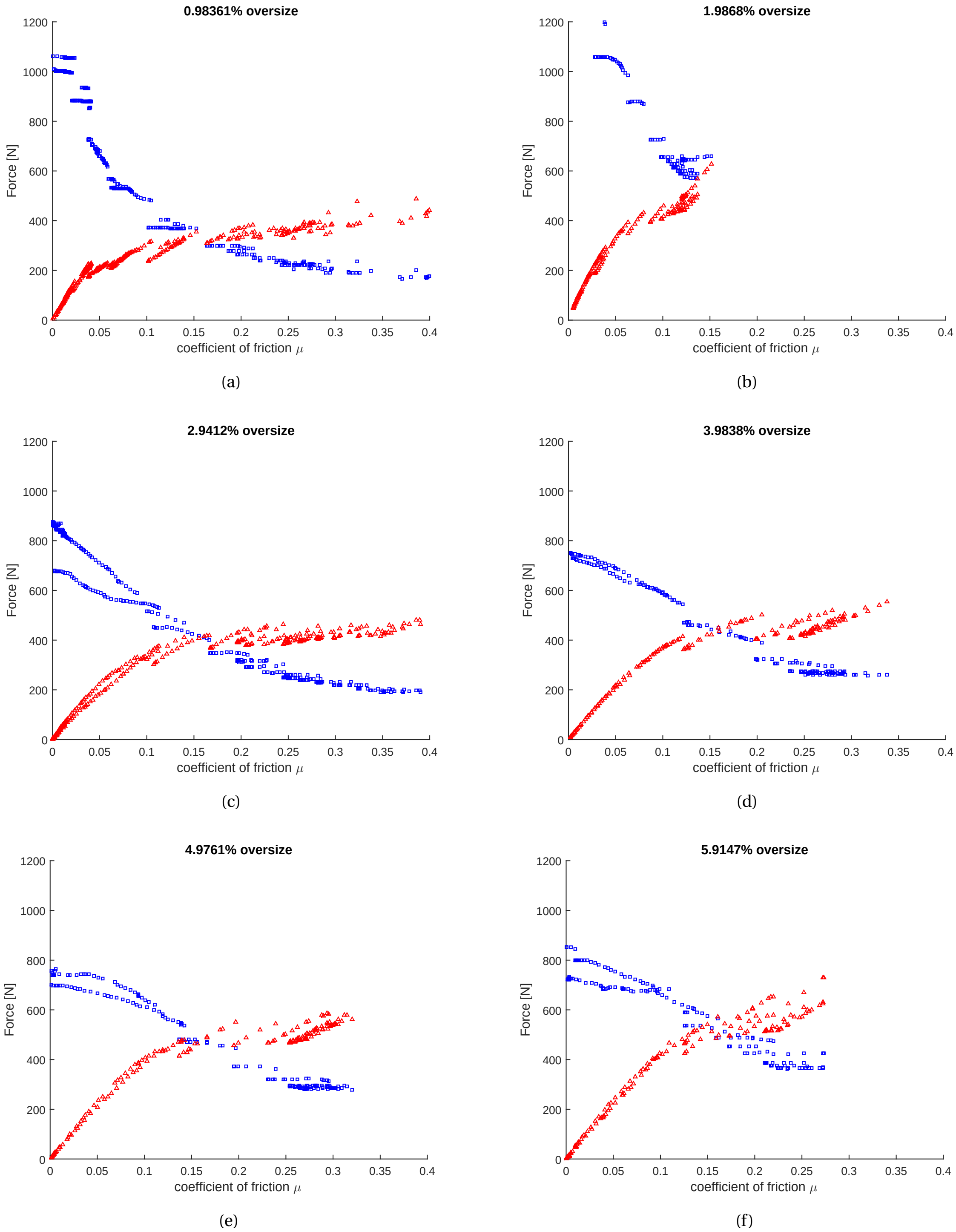

Figure F.4: Forces F_{axial} (△) and F_{circ} (□) are shown as a function of the coefficient of friction for the 15 mm Rosen disk. In each figure two separate measurements are shown. In this figure only the slip data points are shown.

F.3. ROSEN 75 SHORE 13 MM

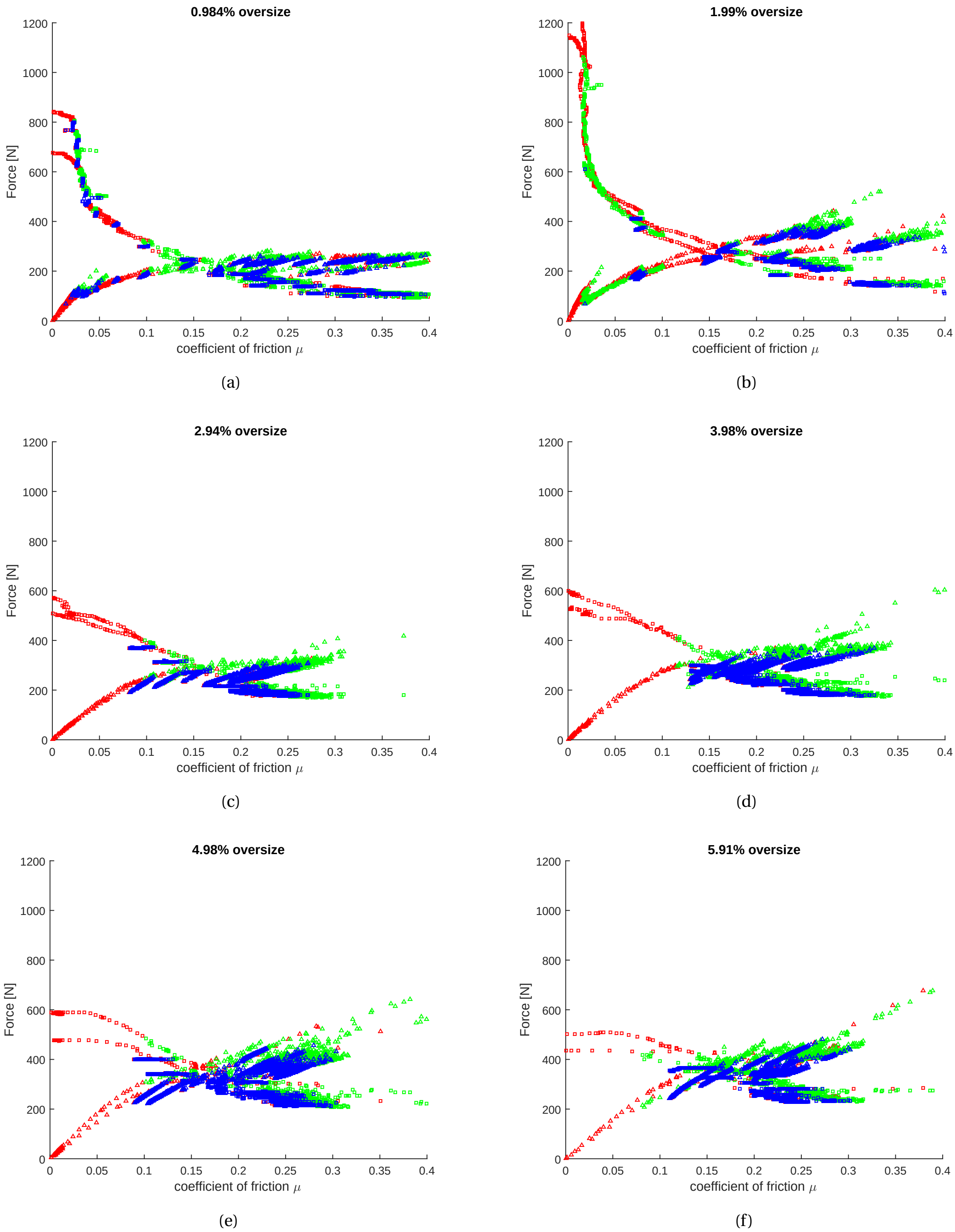

Figure F.5: Forces F_{axial} ($\triangle$) and F_{circ} ($\square$) are shown as a function of the coefficient of friction for the 13 mm Rosen disk. Each figure shows two independent measurements, thereby confirming repeatability. In this figure all data points are shown and the rise, slip and rest data points are distinguished by using different colours. During rise the coefficient of friction increases and the disk is in static equilibrium. During slip the disk slips and a green noisy signal is shown. While resting the disk slowly relaxes and the coefficient of friction decreases. During creep F_{axial} decreases and F_{circ} increases.

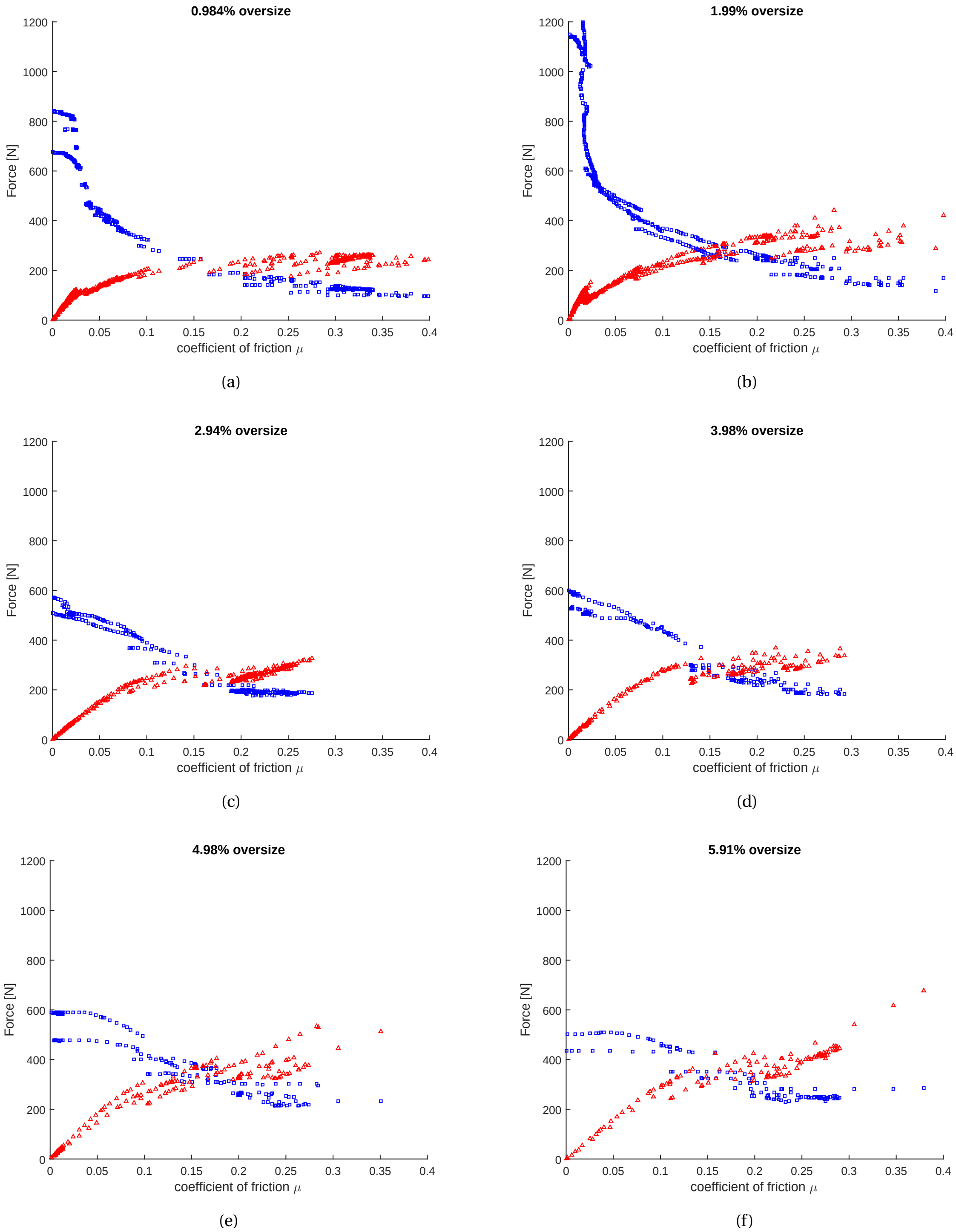

(a) (b) (c) (d) (e) (f)

Figure F.6: Forces F_{axial} (△) and F_{circ} (□) are shown as a function of the coefficient of friction for the 13 mm Rosen disk. In each figure two separate measurements are shown. In this figure only the slip data points are shown.

F.4. ROSEN 65 SHORE 15 MM

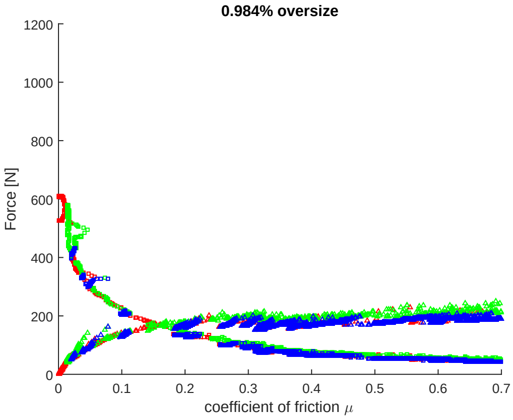

(a)

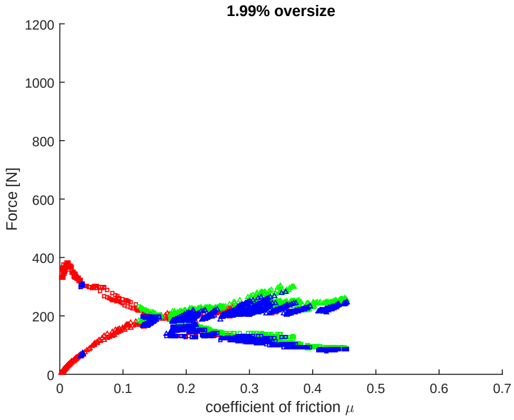

(b)

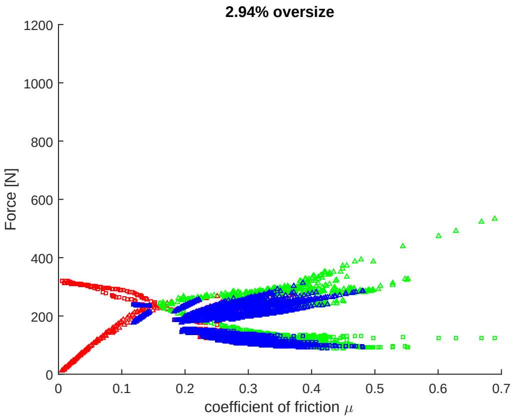

(c)

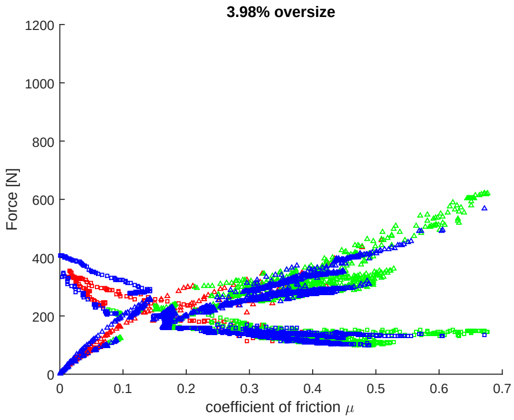

(d)

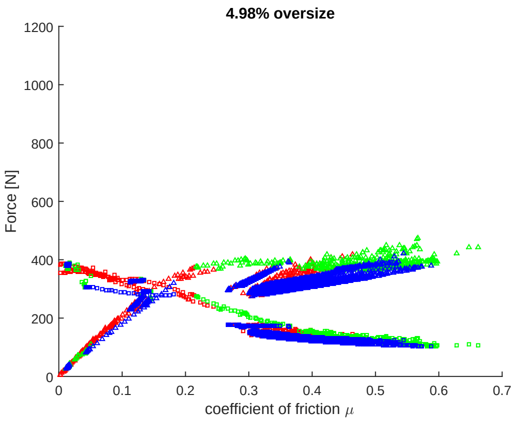

(e)

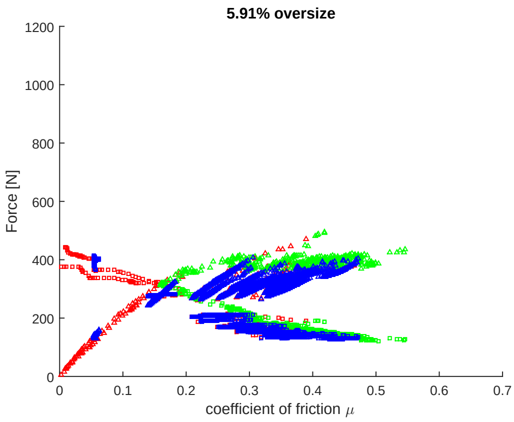

(f)

Figure F.7: Forces F_{axial} ($\triangle$) and F_{circ} ($\square$) are shown as a function of the coefficient of friction for the 65 Shore Rosen disk. Each figure shows two independent measurements, thereby confirming repeatability. In this figure all data points are shown and the rise, slip and rest data points are distinguished by using different colours. During rise the coefficient of friction increases and the disk is in static equilibrium. During slip the disk slips and a green noisy signal is shown. While resting the disk slowly relaxes and the coefficient of friction decreases. During creep F_{axial} decreases and F_{circ} increases.

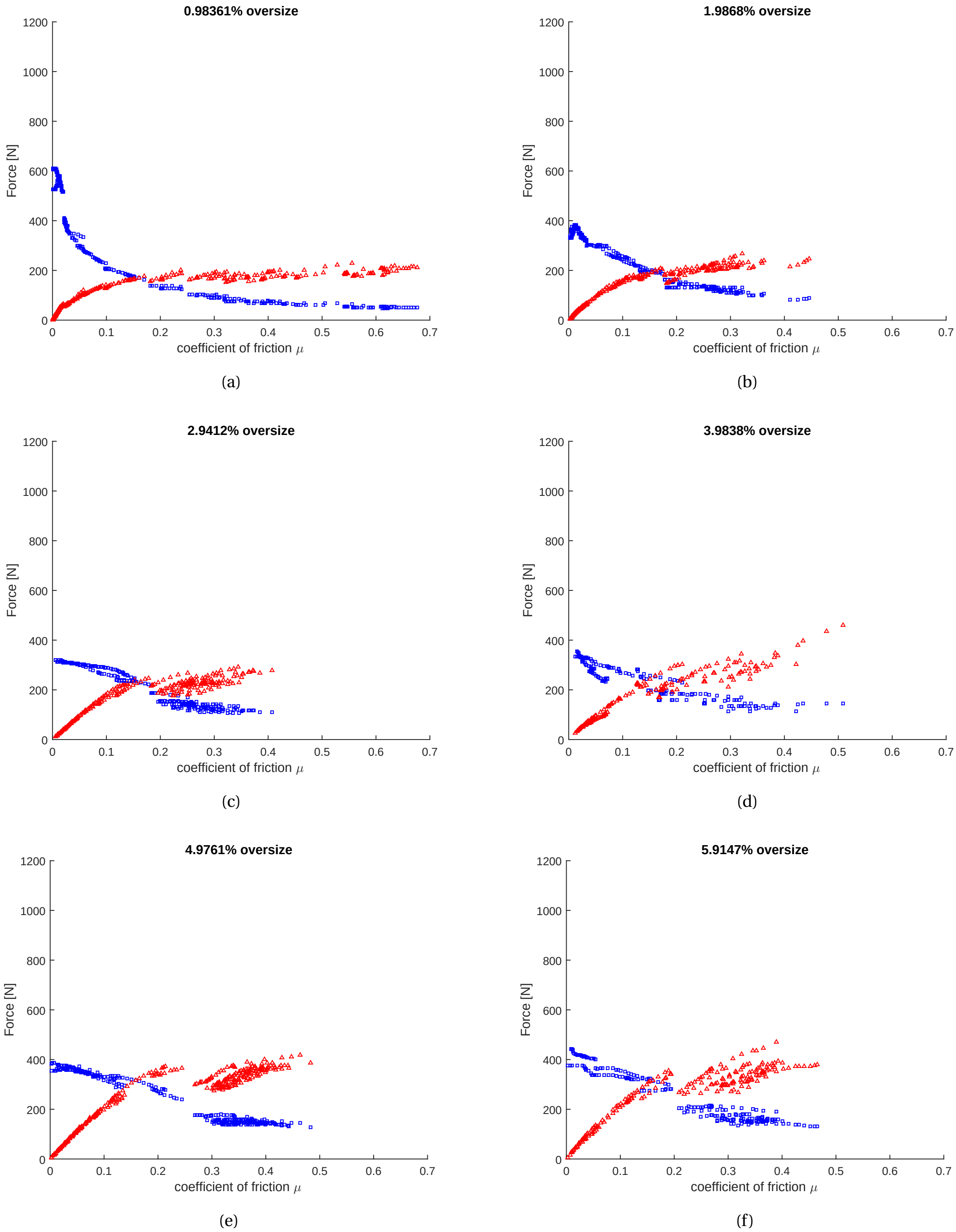

Figure F.8: Forces F_{axial} ($\triangle$) and F_{circ} ($\square$) are shown as a function of the coefficient of friction for the 65 Shore Rosen disk. In each figure two separate measurements are shown. In this figure only the slip data points are shown.

F.5. BAKER HUGHES 62% CLAMPING RATE

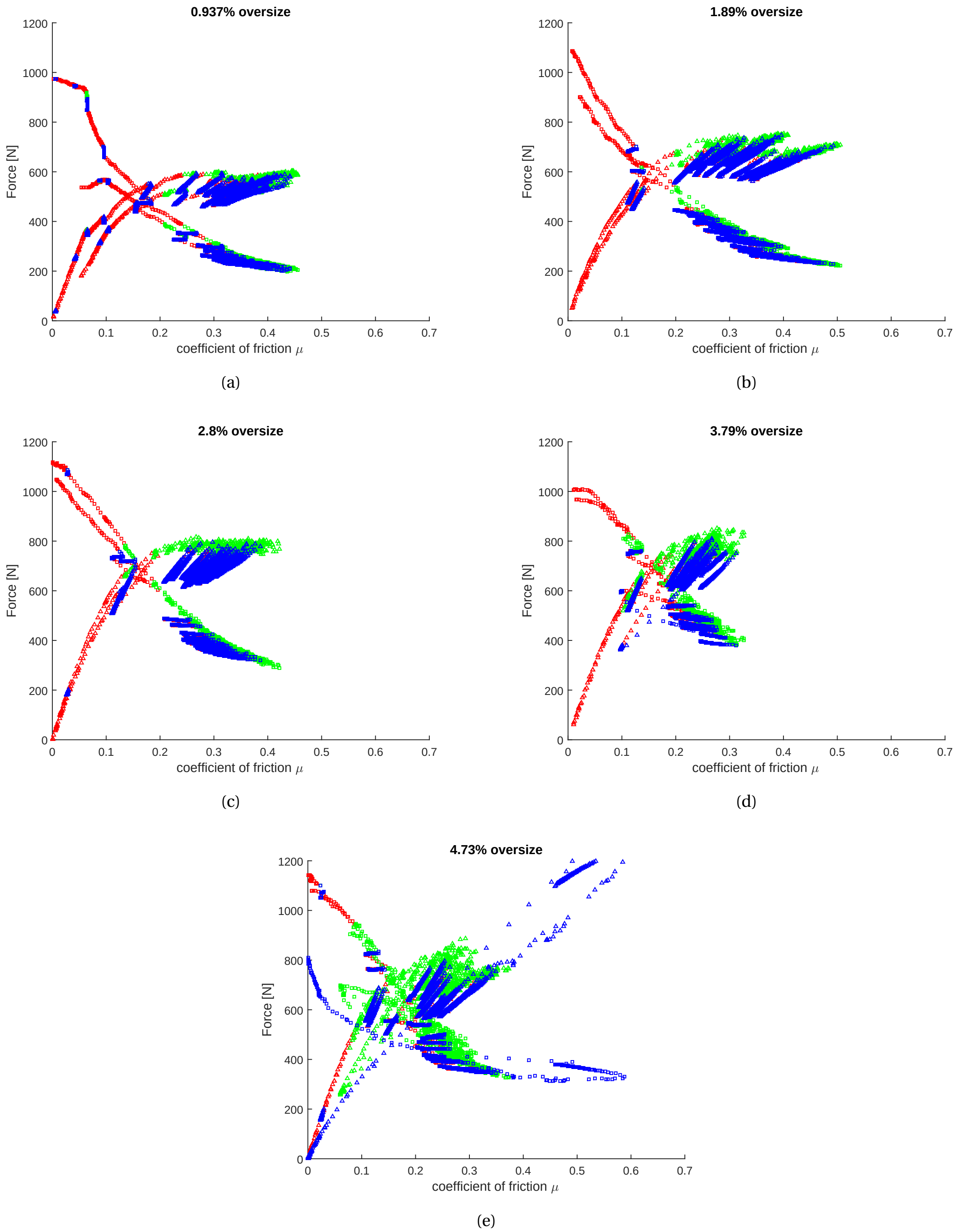

Figure F.9: Forces F_{axial} (△) and F_{circ} (□) are shown as a function of the coefficient of friction for the 62.28% clamping rate disk. Each figure shows two independent measurements, thereby confirming repeatability. In this figure all data points are shown and the rise, slip and rest data points are distinguished by using different colours. During rise the coefficient of friction increases and the disk is in static equilibrium. During slip the disk slips and a green noisy signal is shown. While resting the disk slowly relaxes and the coefficient of friction decreases. During creep F_{axial} decreases and F_{circ} increases.

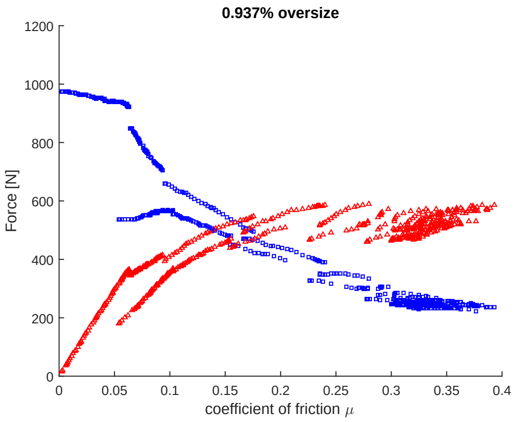

(a)

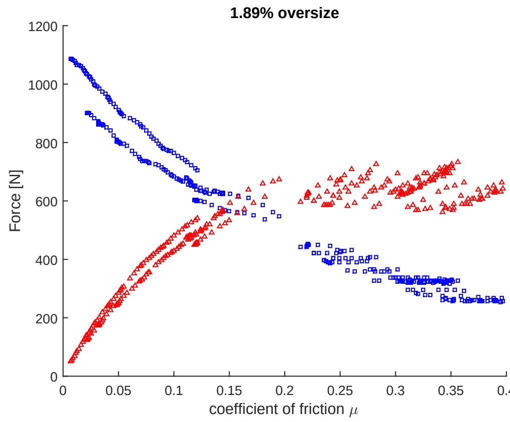

(b)

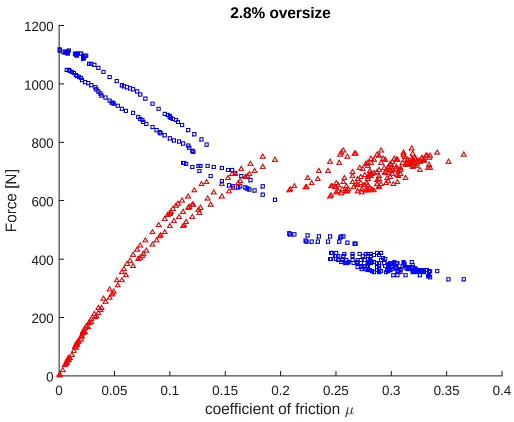

(c)

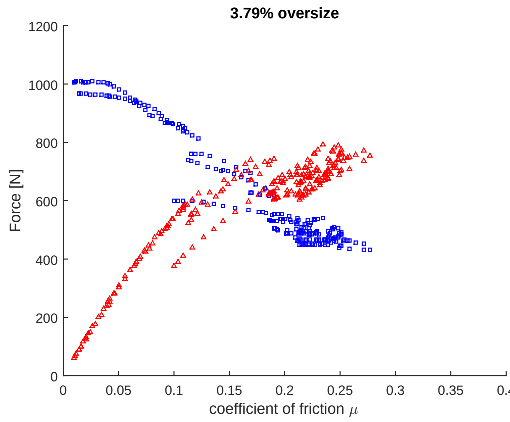

(d)

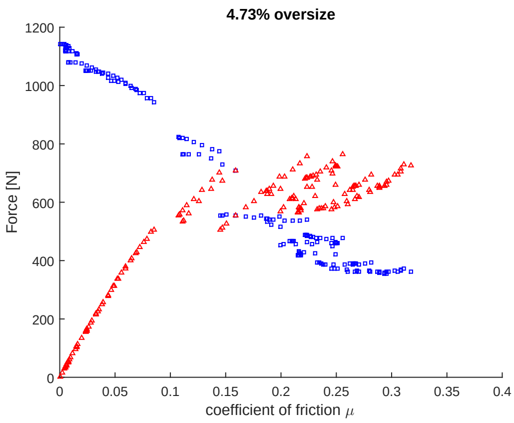

(e)

Figure F.10: Forces F_{axial} (△) and F_{circ} (□) are shown as a function of the coefficient of friction for 62.28 % clamping rate disk. In each figure two separate measurements are shown. In this figure only the slip data points are shown.

Bibliography

[1] *Tdw pipeline pigging catalog*, http://www.tdwimages.com/TDW-Pipeline-Pigging-Products-Catalog/files/assets/common/downloads/TDWPipelinePiggingCatalog.pdf (2015), accessed: 2015-09-01.

[2] A. O'Donoghue, *Pigging as a flow assurance solution: estimating pigging frequency for dewaxing*, Pipeline World **49**, 13 (2004).

[3] P. J. Moeleker, *The shell big picture of technology:bypass pigging*, Slidepack (2015).

[4] G. Groote, P. van de Camp, P. Veenstra, G. Broze, R. Henkes, *et al.*, *By-pass pigging without or with speed control for gas-condensate pipelines*, in *Abu Dhabi International Petroleum Exhibition and Conference* (Society of Petroleum Engineers, 2015).

[5] *Pigteks largest cleaning pig to date*, http://www.pigtek.com/news/2015-02-12-pigteks-largest-cleaning-pig-to-date (2015), accessed: 2015-06-04.

[6] A. F. O'Donoghue, *On the steady state motion of conventional pipeline pigs using incompressible drive media*, Ph.D. thesis, Durham University (1996).

[7] J. L. Cordell, *Conventional pigs - what to use and why*, in *Pipeline pigging and inspection technology* (Pipes and pipelines international, 1992).

[8] A. Nieckele, A. Braga, and L. Azevedo, *Transient pig motion through gas and liquid pipelines*, Journal of Energy Resources Technology **123**, 260 (2001).

[9] X. Zhu, S. Zhang, X. Li, D. Wang, and D. Yu, *Numerical simulation of contact force on bi-directional pig in gas pipeline: At the early stage of pigging*, Journal of Natural Gas Science and Engineering **23**, 127 (2015).

[10] G.-B. Tan, S.-H. Liu, D.-G. Wang, and S.-W. Zhang, *Spatio-temporal structure in wax–oil gel scraping at a soft tribological contact*, Tribology International **88**, 236 (2015).

[11] *Boundary element method for elasticity problems*, http://personal.egr.uri.edu/sadd/mce561/BoundaryElement2.pdf (2016), accessed: 2016-02-01.

[12] B. Boroomand and B. Khalilian, *On using linear elements in incompressible plane strain problems: a simple edge based approach for triangles*, International journal for numerical methods in engineering **61**, 1710 (2004).

[13] A. Beheshti and M. Khonsari, *On the contact of curved rough surfaces: Contact behavior and predictive formulas*, Journal of Applied Mechanics **81**, 111004 (2014).

[14] J. Tiratsoo, *Pipeline pigging technology* (Gulf Professional Publishing, 1992).

[15] J. L. Kennedy, *Oil and gas pipeline fundamentals* (Pennwell books, 1993).

[16] M. Apted, P. Brosnan, S. Marceau, R. Carlyle, D. Richards, R. Coltrane, and J. Dench, *The world is not enough* (MGM Home Entertainment, 2000).

[17] E. Musk, *Hyperloop alpha*, SpaceX.(Online Article). http://www. spacex. com/sites/spacex/files/hyperloop_alpha. pdf (2013).

[18] T. Galta, *Bypass Pigging of Subsea Pipelines Suffering Wax Deposition*, Master's thesis, Norges teknisk-naturvitenskapelige universitet (2014).

[19] J. Southgate, *Wax removal using pipeline pigs*, Ph.D. thesis, Durham University (2004).

[20] T. S. Golczynski and E. C. Kempton, *Understanding wax problems leads to deepwater flow assurance solutions,* World Oil **227** (2006).

[21] G. Fung, W. Backhaus, S. McDaniel, M. Erdogmus, *et al.*, *To pig or not to pig: the marlin experience with stuck pig,* in *Offshore Technology Conference* (Offshore Technology Conference, 2006).

[22] W. Wang, Q. Huang, S. Li, C. Wang, and X. Wang, *Identifying optimal pigging frequency for oil pipelines subject to non-uniform wax deposition distribution,* in *2014 10th International Pipeline Conference* (American Society of Mechanical Engineers, 2014) pp. V004T08A004–V004T08A004.

[23] G. Van Spronsen, A. Entaban, K. Mohamad Amin, S. Sarkar, R. Henkes, *et al.*, *Field experience with by-pass pigging to mitigate liquid surge,* in *16th International Conference on Multiphase Production Technology* (BHR Group, 2013).

[24] A. Muhr, *Modeling the stress-strain behavior of rubber,* Rubber chemistry and technology **78**, 391 (2005).

[25] F. Beer *et al.*, *Mechanics of materials 5th ed,* New York: McGraw-Hills (2009).

[26] A. F. Bower, *Applied mechanics of solids* (CRC press, 2009).

[27] R. Romagnoli, R. Varvelli, *et al.*, *Fem approach to the deformation study of pig cups,* in *The First International Offshore and Polar Engineering Conference* (International Society of Offshore and Polar Engineers, 1991).

[28] M. H. Chow and J. Nimmons, *Pig Pull Tests*, Tech. Rep. (Shell International Exploration and Production Inc., Houston, Houston, 2010).

[29] J. Quarini and S. Shire, *A Review of Fluid-Driven Pipeline Pigs and their Applications,* Proceedings of the Institution of Mechanical Engineers, Part E: Journal of Process Mechanical Engineering **221**, 1 (2007).

[30] B. J. Hamrock, S. R. Schmid, and B. O. Jacobson, *Fundamentals of fluid film lubrication* (CRC press, 2004).

[31] K. L. Johnson, *Contact mechanics* (Cambridge university press, 1987).

[32] P. Wriggers and T. A. Laursen, *Computational contact mechanics*, Vol. 30167 (Springer, 2006).

[33] R. L. Jackson and I. Green, *On the modeling of elastic contact between rough surfaces,* Tribology Transactions **54**, 300 (2011).

[34] G. Liu, Q. Wang, and C. Lin, *A survey of current models for simulating the contact between rough surfaces,* Tribology Transactions **42**, 581 (1999).

[35] J. Greenwood and J. Williamson, *Contact of nominally flat surfaces,* in *Proceedings of the Royal Society of London A: Mathematical, Physical and Engineering Sciences*, Vol. 295 (The Royal Society, 1966) pp. 300–319.

[36] N. Patir and H. Cheng, *An average flow model for determining effects of three-dimensional roughness on partial hydrodynamic lubrication,* Journal of Tribology **100**, 12 (1978).

[37] H. Zhang, S. Zhang, L. Lin, B. Tang, *et al.*, *Mechanical characteristics analysis of pig's sealing disc in offshore pipeline,* in *The Twenty-fifth International Offshore and Polar Engineering Conference* (International Society of Offshore and Polar Engineers, 2015).

[38] J. E. A. Korban, *CFD Modelling of Bypass Pigs*, Master's thesis, Delft University of Technology, the Netherlands (2014).

[39] X. Liang, *Numerical Study of Flow around Bypass Pigs*, Master's thesis, Delft University of Technology, the Netherlands (2015-11-17).

[40] G. Tan, D. Wang, S. Liu, H. Wang, and S. Zhang, *Frictional behaviors of rough soft contact on wet and dry pipeline surfaces: With application to deepwater pipelaying,* Science China Technological Sciences **56**, 3024 (2013).

[41] A. Becker, *The Boundary Element Method in Engineering: A Complete Course* (McGraw-Hill, 1992).

[42] E. Klaseboer, Q. Sun, and D. Y. C. Chan, *Non-singular boundary integral methods for fluid mechanics applications,* Journal of Fluid Mechanics **696**, 468 (2012).

[43] A. Gent, *On the relation between indentation hardness and young's modulus,* Rubber Chemistry and Technology **31**, 896 (1958).

[44] *Basic nonlinear analysis user's guide,* Software documentation (2015).

[45] J. F. Archard, *Contact and rubbing of flat surfaces,* Journal of Applied Physics **24**, 981 (1953).

[46] G. Beer, I. Smith, and C. Duenser, *The boundary element method with programming: for engineers and scientists* (Springer Science & Business Media, 2008).

[47] L. Gaul, M. Kögl, and M. Wagner, *Boundary element methods for engineers and scientists: an introductory course with advanced topics* (Springer Science & Business Media, 2013).

[48] J. Zechner and G. Beer, *A fast elasto-plastic formulation with hierarchical matrices and the boundary element method,* Comput. Mech. (2013).

[49] Y. Liu, *Fast multipole boundary element method: theory and applications in engineering* (Cambridge university press, 2009).

[50] F.-C. Shiue, *Geometrically nonlinear analysis for an elastic body by the boundary element method*, Ph.D. thesis, Iowa State University (1989).

[51] G. Chen and J. Zhou, *Boundary element methods with applications to nonlinear problems*, Vol. 7 (Springer Science & Business Media, 2010).

[52] I. E. Idelchik and E. Fried, *Handbook of hydraulic resistance* (Hemisphere Publishing, New York, NY, 1986).

[53] I. M. Meththananda, S. Parker, M. P. Patel, and M. Braden, *The relationship between shore hardness of elastomeric dental materials and young's modulus,* dental materials **25**, 956 (2009).